INTEGRALLY CORED CERAMIC INVESTMENT CASTING MOLD FABRICATED BY CERAMIC STEREOLITHOGRAPHY

by

Chang-Jun Bae

A dissertation submitted in partial fulfillment
of the requirements for the degree of
Doctor of Philosophy
(Materials Science and Engineering)
in The University of Michigan
2008

Doctoral Committee:

Professor John W. Halloran, Chair
Professor Brian Love
Professor Tresa Pollock
Associate Professor Suman Das, Georgia Institute of Technology

To Eun-Jeong and my family for their love and support.

ACKNOWLEDGEMENTS

First and foremost I must thank my advisor, Prof. John Halloran, for the wonderful research advice and support. I would also like to thank my committee members, Prof. Brian Love, Prof. Tresa Pollock, and Prof. Suman Das, for their participation and useful discussions.

Special thanks to Alisha Diggs and Dr. Angela Knapp, who helped make this work possible. I must also acknowledge many people in the Halloran's research group and Korean students in the MSE, Macro, Chemical engineering for their friendship and constant support throughout my study here.

Lastly, I could not have reached this point without the support of Eun-Jeong and my family. I must thank all the friends and colleagues at The University of Michigan for providing a wonderful academic and social atmosphere during my grad school.

TABLE OF CONTENTS

LIST OF FIGURES

LIST OF TABLES

CHAPTER 1

INTRODUCTION

Investment casting (IC) is a widely used technique for modern metal casting, and provides an economical means of mass producing shaped metal parts containing complex features. Hollow cored super alloy airfoils in a gas turbine engine are an example of complex IC parts. The complex internal hollow cavities of the airfoil are designed to conduct cooling air through one or more passageways. These complex internal passageways have been fabricated by a lost wax process requiring several process steps. These steps include tooling to make the metal injection die, injection molding for the core, mold wax pattern used to define metal, pattern assembly in clusters around a common sprue and feeder system, and dipping the core encased in wax into the wet slurry to make shell mold.

Several steps in the lost wax process generate problems such as high cost and decreased accuracy of the ceramic mold. For example, costly tooling and production delay are necessary to produce mold dies for complex cores and wax patterns used in injection molding, resulting in a big obstacle for prototypes and smaller production runs. Besides, if movement or shifting of the core in the mold occurs during injection molding, it will induce unacceptable variations in the wall thickness of the hollow structure and decrease the consistency and accuracy of the ceramic core and the shell mold.

Rather than using separate cores, patterns, and shell molds, it would be

advantageous to directly produce a mold that has the casting cavity and the ceramic core by one process. Ceramic stereolithography (CerSLA) can be used to directly fabricate the integrally cored ceramic casting mold (ICCM). CerSLA builds ceramic green objects from CAD files using many thin liquid layers of powder in monomer, which are solidified by polymerization with a UV laser, thereby "writing" the design for each slice. In this work we demonstrate the fabrication of an integrally cored ceramic mold (ICCM), the ceramic core with a ceramic mold shell in a single patternless construction, fabricated by CerSLA. CerSLA is considered as an alternative method to replace lost wax processes, for small production runs or designs too complex for conventional cores and patterns.

This dissertation addresses the integrally cored casting ceramic mold (ICCM) fabricated by ceramic stereolithography (CerSLA). The main topic is development of methods to successfully fabricate an ICCM by CerSLA from refractory silica, as well as related issues. The related issues were the segregation of coarse fused silica powders in a layer, the degree of segregation parameter to prevent segregation, and sintering and cristobalite transformation in fused silica compacts.

The silica core must be stable when the hot metal is cast. The core must be porous, but it cannot densify at casting temperature since this would cause shrinkage. It cannot creep at these high temperatures. The classical solution is to use coarse refractory powders of larger than 50 μm. However, coarse refractory grade powders in suspension quickly sediment, leading to particle size segregation in the layers of a green body. After binder burn-out, the particle segregated regions in the green body generated property-degrading defects such as delamination, distortion, and excessive shrinkage. In order to prevent segregation in a layer, the effect of particle size distribution on the segregation is

discussed in Chapter 3.

The tendency for particles to segregate during SLA building was modeled with a parameter called degree of segregation (β). Expressions were derived to predict the segregation in a layer when a UV laser exposes the ceramic suspension to write a layer. The degree of segregation was related to two time constants; settling time and writing time. If settling time is shorter than writing time, the coarse powder has already settled down in a layer, separating two main phases that are composed of a polymer and a silica powder dominated phase. Therefore, in order to suppress the segregation in a layer, criteria for no segregation are defined in Chapter 4.

Refractory grade fused silica is used to make ceramic molds for Ni-based superalloy turbine blades. During sintering of silica molds, the fused silica is partially transformed to cristobalite. The cristobalite fraction is a major property determining the stability and mechanical strength of ICC molds. Quantitative X-ray diffraction (QXRD) was used to calculate the amount of transformed cristobalite in fused silica compact and understand the transformation kinetics of fused slica. The transformed kinetics of fused silica will be discussed in Chapter 7.

The most important aspect of this work is that ceramic stereolithography (CerSLA) can replace the lost wax process to fabricate an integrally cored ceramic mold (ICCM) which combines the ceramic core with a ceramic mold shell in a single patternless construction. The integrally cored casting ceramic mold (ICCM) fabricated by ceramic stereolithogaprhy (CerSLA) is shown in Chapter 5. Cracks are initiated from the thermal polymerization of residual monomer and photoinitiator in the green body. This will be discussed in Chapter 6.

CHAPTER 2

BACKGROUND ON THE TOPICS RELATED TO THE APPLICATION OF CERAMIC STEREOLITHOGRAPHY (CerSLA):

2.1 Complex interior cooling passages in Turbine Airfoils

Gas turbine engines include a compressor for compressing air, a combustor for mixing the compressed air with fuel and igniting the mixture, and a turbine blade assembly for producing power. The performance of a gas turbine engine generally is dependent on the operating temperature in the combustion chamber, increasing the efficiency of a gas turbine engine with the working temperature. For increasing the efficiency of a gas turbine engine, it should be workable at the high operation temperature of 1,400 degrees Celsius.[1] With the consideration of new material development to resist the catastrophic failure of the engine components at high temperatures, the design of complex internal hollow structure has been considered. The airfoils, such as blades and vanes, within the engine are among the components exposed to significant thermal loading during engine operation.[2] Therefore, to prevent the degradation of the airfoils when exposed to high temperatures, complex hollow interior passages are used to conduct cooling air through one or more passageways in the turbine airfoil.

Honeywell is the industrial partner on this project, but the details of their cooling passages cannot be published. Instead we work with a model design. The attributes of

airfoil will be illustrated with a generic airfoil form the literature.[1] Figure 2.1 shows a perspective view of airfoil, where airfoils are formed from a root portion having a platform at one end and an elongated portion forming a blade that extends outwardly from the platform coupled to the root portion. The blade is ordinarily composed of a tip opposite the root section, a leading edge, and a trailing edge. Figure 2.2 is a cross-sectional view of airfoil, showing that the inner aspects of most turbine airfoils typically contain three intricate cooling channels forming a cooling system. The three cooling channels are a leading edge cooling channel, a mid-chord serpentine cooling channel, and a trailing edge cooling channel. The mid-chord serpentine cooling channel facilitates the efficient removal of heat from the airfoil, especially at the intersection between the tip section and the trailing edge. For greater cooling efficiency of airfoils in turbines, these more complex internal passageways have been required.

2.2 Lost wax process for investment casting

Investment casting (IC) is a widely used technique for modern metal casting, and provides an economical means of mass producing shaped metal parts containing complex features.[3] Superalloy airfoils have been produced by investment casting, which use ceramic cores and wax patterns with ceramic shell molds. To build a core representing hollow cavities and wax pattern to define metal, the permanent tooling firstly takes the form of dies. After fabricating dies for a core and wax pattern, several processing steps of a lost wax process are required to produce the ceramic cores and shell molds for superalloy airfoils. Figure 2.3 shows a schematic diagram of a conventional lost wax process with several processing steps; core preparation, injection molding for wax pattern,

and dipping process for ceramic shell molds.

Hollow cavities in cast airfoils have been produced using preformed ceramic cores located within the injection mold. The pieces of the complex ceramic core are formed separately using injection molding, assembled together. Wax is injected into the mold and over cores to make a pattern for the cast metal. Patterns are normally assembled in clusters around a common sprue and feeder system prior to building-up the external mold shell. Dipping the ceramic core encased in wax, and adding coarse refractory grit onto the wet slurry, the ceramic shell mold is built up around each wax pattern. The previous procedures are repeated several times to make a shell mold with sufficient thickness, for strength and integrity, before being fired.

Although lost wax process has been used to produce ceramic cores and shell molds for investment casting, problems that need to be solved are associated with improving accuracy, reproducibility, cost and production delay. For example, given several steps in the lost wax process, when the wax is usually injection molded around the core, wax lifting occurs as wax cools. This wax lifting problem has been particularly detected at the concave core surfaces. Another problem is movement or shifting of the core in the mold during injection molding. Those problems result in the distortion of the shape of the wax pattern and hence the shape of the cast objects. Since this slight displacement of the core results in unacceptable variations in the wall thickness of the hollow structure, it will decrease the consistency and accuracy of the ceramic core and shell mold designed for turbine airfoils. In addition, costly tooling is required to produce mold dies for complex cores and wax patterns by injection molding. The cost and production delays associated with this tooling are disadvantageous for prototypes and

smaller production runs.

2.3 Ceramic Stereolithography (CerSLA)

2.3.1 Stereolithography (SLA) vs. Ceramic stereolithography (CerSLA)

Solid freeform fabrication (SFF) techniques can be used to directly fabricate the mold without several intermediate steps of the conventional lost wax process.[4] SFF is the general name for an emerging technology in which sophisticated three dimensional (3D) objects can be produced directly from a layer-by-layer process based on computer aided design (CAD) files. Stereolithography (SLA) invented by Chuck Hull is the most commercialized technique among the SFF processes.[5]

As a general explanation of SLA, this is done with a monomer resin, typically an acrylate or an epoxy, which cures upon exposure to radiation from a UV laser. Figure 2.4 shows a schematic of SLA process that builds the solid polymer object layer-by-layer. From a computer aided design (CAD) file, sliced into two dimensional cross-sections, each layer is solidified by scanning a laser beam onto the surface of the resin. After finishing the 'build' of one layer, the support platform on which the layer has been build, moves downward into the vat of liquid resin. A new layer flows across the surface, where a recoat blade sets the exact thickness of the layer. The laser proceeds to build the second layer of the part, where this layer is knitted to the one below. The process is repeated until the final object is complete.

SLA is considered to be the most accurate technique in terms of dimensional accuracy among the SFF techniques since it can produce 3D objects with exact tolerances and the best surface finishes. SLA is limited in its ability to produce a complex 3D IC

pattern composed of only polymers due to the fact that it is a resin-based system. Thus, it is difficult to build any 3D complex ceramic mold using the SLA process since this process requires extra steps similar to those used here in the lost wax process.

Griffith and Halloran have addressed a new area for direct fabrication of 3D complex ceramic parts by replacing a resin-based system with a ceramic suspension based system.[6,7] They have prepared ceramic suspensions for dispersing various types of ceramic including alumina, silica and zirconia in both aqueous and non-aqueous liquid media. Given the ceramic suspension, the SLA process has been called ceramic stereolithography (CerSLA). CerSLA builds ceramic green objects from CAD files from many thin liquid layers of powder in monomer, which are solidified by polymerization with a UV laser, thereby "writing" the design for each slice.

They have used the SLA process, but initially created a ceramic green body instead of a solid polymer part. Ceramic green bodies were shaped composites of ceramic powder in a polymeric binder, containing about 50 volume percent ceramic. Ceramic green bodies were readily converted to solid ceramics by removing the binder and firing the ceramic. In their research, forming the ceramic green body was accomplished by photopolymerizing a highly loaded ceramic suspension in an appropriate photopolymerizable liquid. The CerSLA suspension must have the following characteristics: 1) it must contain at least 40 volume percent ceramic powder to provide for subsequent sintering, 2) it must be fluid enough for recoating, so must have a viscosity less than 3000 mPa-s at low shear rates and must be self-leveling, 3) it must have a depth of cure upon UV irradiation at least as large as a practical CerSLA layer thickness, or at least 200 micrometers.

2.3.2 Photo-polymerization using free radical polymerization

Radiation curable polymer technology was developed to reduce volatile organic components in coating formulations by government mandates. Radiation curing of coatings, inks, and adhesives has enjoyed relatively rapid commercial growth within the last 10-20 years. It involves the polymerization and cross-linking of functional monomers and oligomers (usually liquid) into a 3-D polymer network (usually a solid film) induced by photons (UV curing) or electrons (EB curing).[8]

There are many advantages to using UV radiation curing which is focused on this experiment. UV radiation curing allows fast, almost instant, transformation of a liquid resin into a solid material by polymerization of a solvent-free formulation at ambient temperature selectively in the irradiated areas.[9] The cure time is reduced and, since heating of the whole component is not required, the overall energy consumption is lower than for thermally initiated curing processes, thermal stresses are reduced, and less expensive tooling can be used. Another important advantage is the reduction of organic emissions into the environment. Since curing starts on the component surface, which is exposed to the radiation first, unreacted organic is trapped below the surface and is available for ongoing polymerization.

For example, polymerization of acrylate monomer is an energetically favorable UV curing reaction with the reaction heat 19.2 kcal/mole. UV curing of acrylate monomer is based on photoinitiated polymerization that is mediated by photoinitiators. Photoinitiators are required to absorb light in the ultraviolet visible spectral range, generally 250-550 nm, and generate free radicals, which subsequently initiate and catalyze polymerization, from the reaction with photon. There are three basic steps to

photopolymerization: initiation, propagation, and termination.[10,11] At the step of initiation, the photoinitiator absorbs the photons (if at the appropriate frequency, e.g. in the UV range), and this photoinitiator photochemically cleaves to produce a free radical. These radicals then react with the monomers to start the polymerization reaction. For laser induced photopolymerization, an initiator must be chosen that absorbs efficiently at the frequency of the incident photons, and then generates the initiating species with a high quantum yield. The time to initiate polymerization is on the order of 10^{-6} seconds.

Next is the propagation of the polymerization reaction which takes place in micro-regions near the site of radical initiation. The growing macro-radical becomes a cross-linked gel at a relatively low degree of conversion. The rate of polymerization steadily decreases as the concentration of unreacted monomer decreases and the viscosity of the gel increases. The mobility of free monomer to the site of the macro-radical is thus restricted at higher conversion.

After time, termination starts to occur, mainly due to recombination and oxygen inhibition. Recombination involves two radicals joining together to form a non-reactive molecule. Oxygen inhibits the polymerization reaction due to oxygen molecules diffusing into the surface of the polymerizing micro-region and terminates the polymerization reaction. An extra concern in photopolymerization is the amount of 'dark reaction' occurring after the laser has moved from the micro-region. Dark polymerization is a result of macro-radicals with long lifetimes that proceed to continue the photopolymerization process.

2.3.3 Photocurable monomers and photoinitiator used in Ceramic suspension

CerSLA suspensions can be prepared by dispersing powders in essentially pure monomers and polymerizing the entire system to create a ceramic green body consisting of a solid polymer filled with ceramic powder. Pure monomer is useful for CerSLA. However, it has the disadvantage of relatively large polymerization shrinkage, high exothermic heat production, and the presence of a large volume fraction of polymer, which makes subsequent binder burnout (removal of the binder) difficult. Alternatively, the powders can be dispersed in a solution of monomer, which gels upon solidification. This gel is quite rigid when it contains a high loading of powder. These photo-gelling solutions have the advantages of smaller polymerization shrinkage, less heat evolution, and smaller solid polymer residue.

The low viscosity of monomer is necessary to facilitate the increase of solids loading and to minimize the final suspension viscosity. Pure monomers widely used in the CerSLA are 1, 6-hexane diol diacrylate (HDDA[1], M_w=226 g/mol), Ethoxylated pentaerythritol tetraacrylate (EPTA[2], M_w=528 g/mol), isobornyl acrylate (IBA, M_w=208 g/mol), and propoxylated neopentyl glycol diacrylate (PNPGDA, M_w=328 g/mol).

Figure 2.5 show the material properties and chemical structure of HDDA. HDDA is highly reactive difunctional acrylate monomer commonly used in the paint and ink industries. HDDA is a low-viscosity (9 mPa-s at 25^{o}C), fast curing monomer with low volatility, and good solvency for use in free radical polymerization. In addition, EPTA shown in Figure 2.6 is mixed with HDDA to provide excellent cross-linking with high stiffness, but it has the skin irritant problem.

[1] SR238B, Sartomer Inc., Exton, PA
[2] SR494, Sartomer Inc., Exton, PA

As a formulation with low-irritation monomers, the mixture of IBA [1] and PNPGDA[2] has been used. The material properties and chemical structure of IBA and PNPGDA are listed in Figure 2.7. IBA is a low-viscosity (8 mPa-s at 25^{o}C) and monofunctional monomer utilized as an excellent reactive diluent. After polymerization through free radical polymerization, the cyclic group in IBA increases the glass transition temperature. PNPGDA is a low viscosity (15 mPa-s at 25^{o}C), low skin irritation monomer, and difunctional monomer employed as a crosslinker.

Chemical structures and UV absorption characteristic of Irgacure 184 is shown in Figure 2.8. The photoinitiator, Irgacure 184[3] (a hydroxyketone) has been used due to its high solubility in monomers such as HDDA, IBA, and PNPGDA and its high absorption at long ultraviolet wavelength. High absorption is necessary for the creation of free radicals and for efficient photopolymerization. Another useful property of the ketone photoinitiator is the ability to scavenge the oxygen from near the surface. Since oxygen molecules diffusing into the suspension react with radicals, they terminate or quench the polymerization reaction. The ketone photoinitiator catches oxygen molecules in the suspension and combine with some of the photoinitiator's free radicals so that it increases the efficiency of polymerization.

2.4 Refractory Ceramics for Investment Casting

Refractory materials, by definition, are supposed to be resistant to heat and are exposed to different degrees of mechanical stress and strain, thermal stress and strain, corrosion/erosion from solids, liquids and gases, gas diffusion, and mechanical abrasion

[1] SR506A, Sartomer Inc., Exton, PA
[2] SR9003, Sartomer Inc., Exton, PA
[3] Irgacure 184, Ciba specialty chemicals, Tarrytown, NY

at various temperatures.[12,13] Different refractories are designed and manufactured so that the properties of the refractories will be appropriate for their applications. Refractory ceramics are widely used in investment casting. Investment casting is also known as the "lost wax" process.[14] Ceramic slurry to make a shell mold with a uniform face coating is used to coat wax patterns produced by injection molding. In order to build up a mold strong enough and thermal shock resistant enough, the dip-coating operation is repeated. The selection of refractory ceramics is an important process to make ceramic molds with their interior precisely duplicating the shape of the part to be cast. In investment casting, the ceramic nature of the mold is crucial to the process and lends itself to a wide variety of casting applications and an even wider selection of alloys.[15,16]

Among the refractory ceramics, silica is the material extensively used for ceramic molds due to its advantages; a low thermal expansion and easy removal of silica. Although the core is subjected to thermal shock by the mold being plunged into an oven at about 1000ºC, fused silica with a very low expansion makes less difference of thermal expansion between mold and core when heat is applied. However, the silica core, being composed of a glassy material, starts to soften and will be susceptible to bow or twist if the differential expansion forces are imposed on the system. This problem is improved by using a modified composition such as 90% silica glass and 10% crystalline cristobalite having stiff structure. It would be difficult to use pure cristobalite as a raw material because of the disruptive phase change between α and β phases at 220ºC on heating, but if it forms at high temperature below 220ºC it will disrupt on cooling, which is ideal for assisting easy removal of molds after casting. These peculiarities of silica can also be used as a great advantage in preformed ceramic core technology, where it also meets the

other essential requirement of being soluble in caustic soda solutions and therefore easily removed from the inside of casting.

In order to limit the effect of the phase change of silica core, alumina or zircon powder is used to dilute the silica. These are not soluble in the core leach process but will separate as sludge as the silica dissolves. Ceramic materials or impurities added into silica promote crystallization while others may retard it. Silica as supplied is usually much purer than some of the other ceramic materials used for investment casting, mainly because of the natural purity of the silica sand or rock crystal used in its manufacture. Most problems therefore arise from other materials added to the silica based core. Zircon very slightly degrades the high temperature stiffness because of its own impurities, while alumina may significantly modify and retard the amount of cristobalite formed at the core firing stage. High levels of alumina greatly reduce the resistance to deformation of a silica core. Traces of alkali metals, as in water based binders, promote cristobalite with beneficial effects.

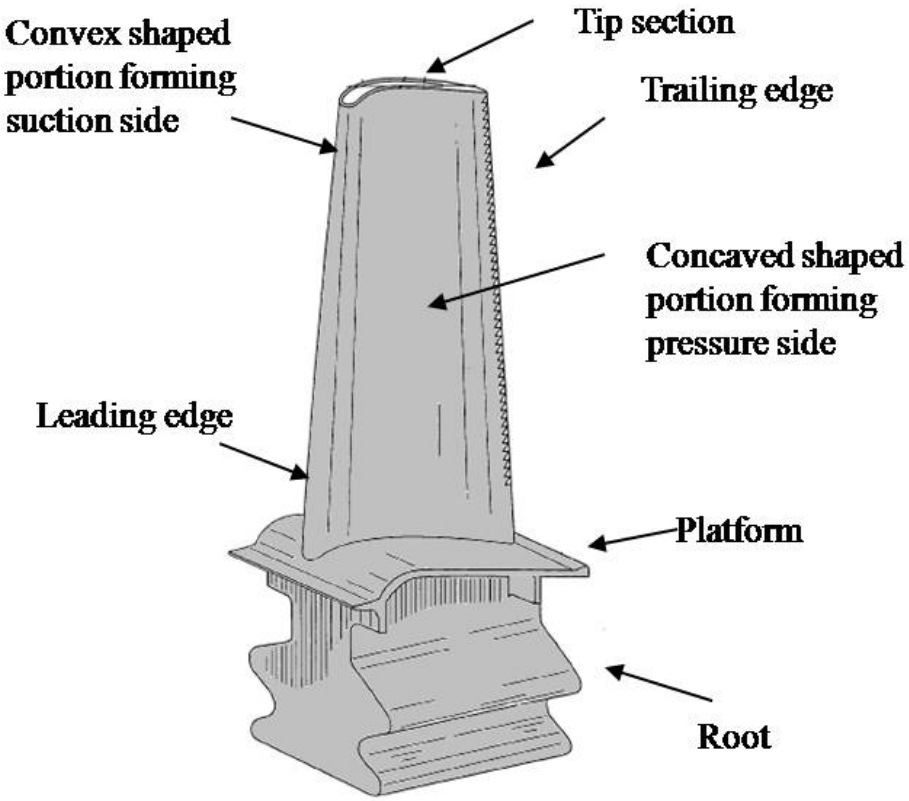

Figure 2. 1 A perspective view of a turbine airfoil. Illustration from Siemens's turbine airfoil[1]

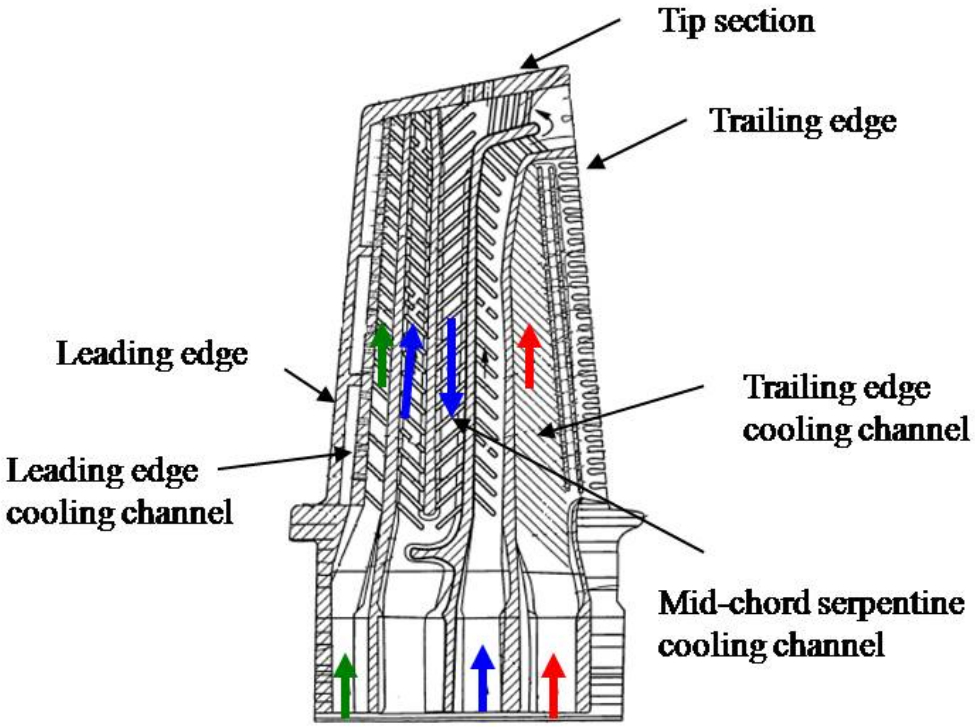

Figure 2. 2 A cross-sectional view of a turbine airfoil. Illustration from Siemens's turbine airfoil[1]

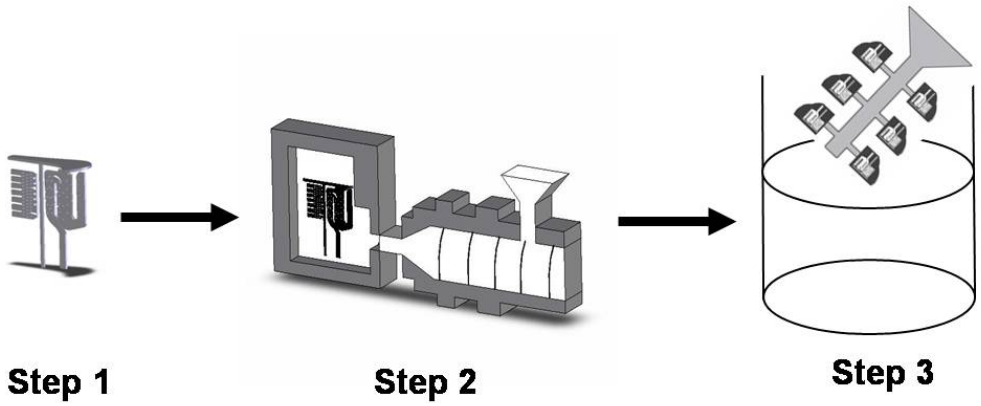

Figure 2. 3 Schematic diagram of the several processing steps in the conventional lost wax process how to build ceramic mold for super alloy airfoils; Step1: make core, Step2: mold wax pattern to define metal, and Step3: build shell mold over wax pattern.

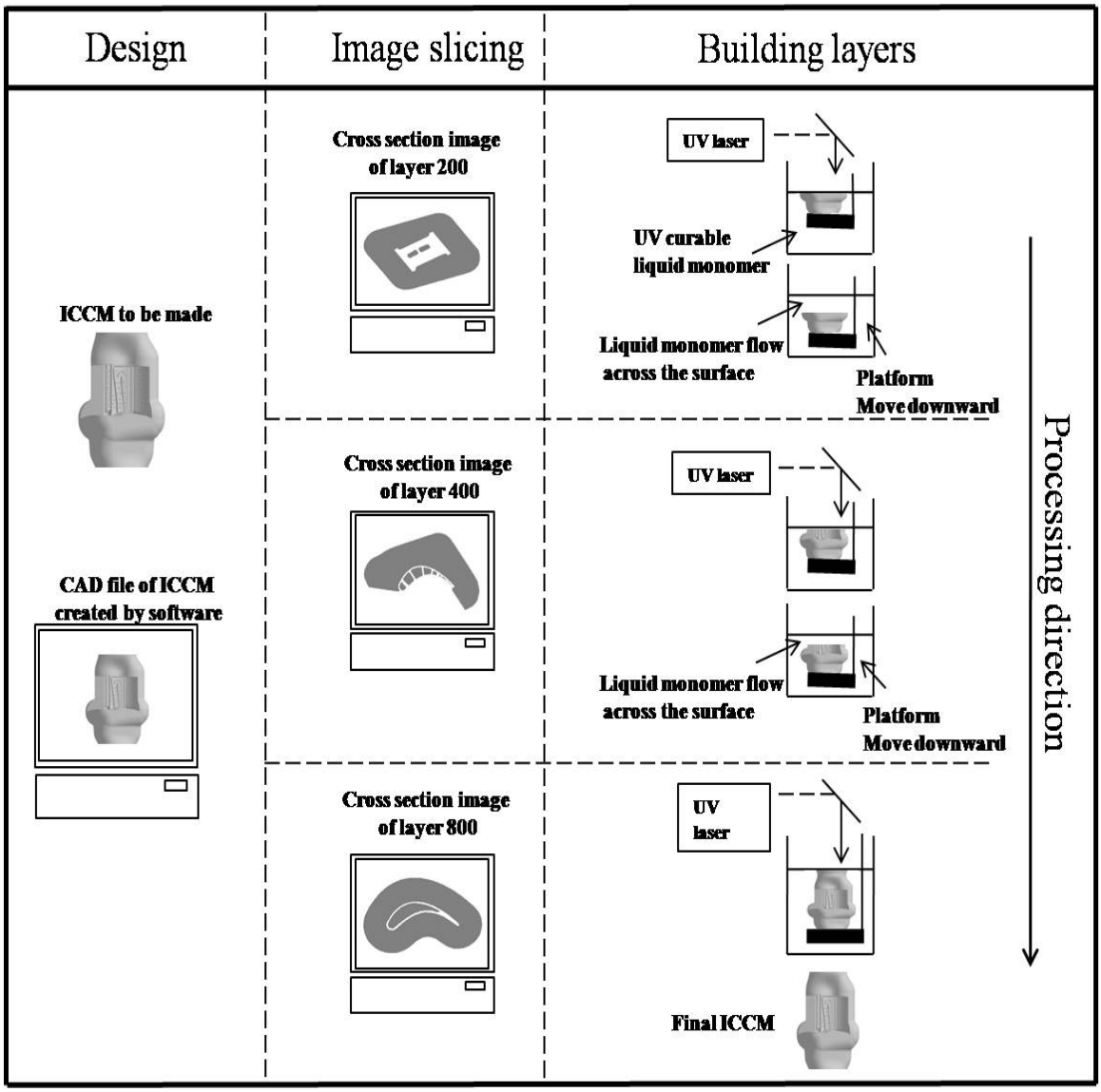

Figure 2. 4 Illustrated SL process

1, 6 Hexanediol diacrylate (HDDA)	
Functionality	**2**
Density @ 25°C	**1.02 g/mL**
Viscosity @ 25°C	**9 mPa-s**
Refractive index @ 325nm	**1.456**
Molecular weight	**226**

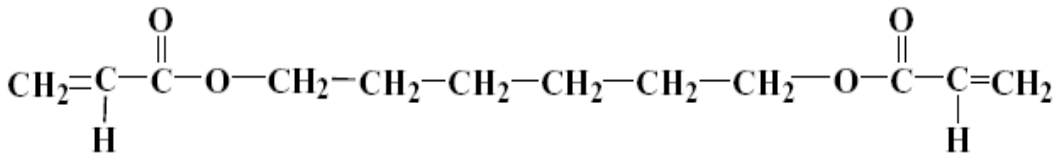

Figure 2. 5 Material properties and chemical structure of Hexanediol diacrylate (HDDA)

Ethoxylated pentaerythritol tetraacrylate (EPTA)	
Functionality	**4**
Density @ 25°C	**1.12 g/mL**
Viscosity @ 25°C	
Refractive index @ 325nm	**1.471**
Molecular weight	**528**

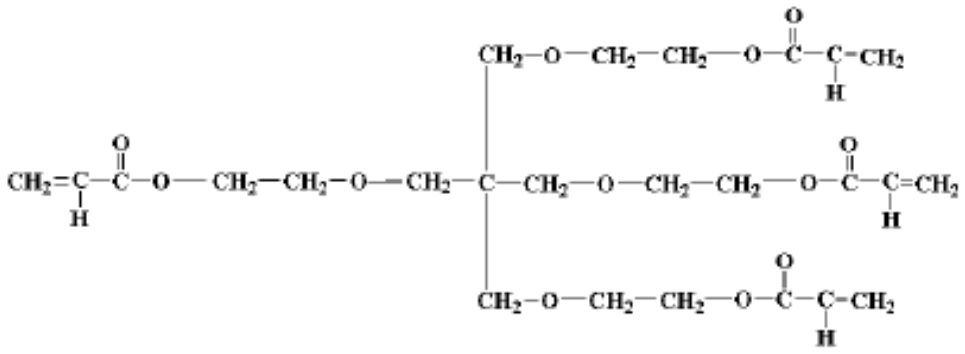

Figure 2. 6 Material properties and chemical structure of Ethoxylated pentaerythritol tetraacrylate (EPTA)

	IBA	PNPGDA
Functionality	**1**	**2**
Density @ 25°C	**0.987 g/mL**	**1.005 g/mL**
Viscosity @ 25°C	**8 mPa-s**	**15 mPa-s**
Refractive index @ 325nm	**1.472**	**1.447**
Molecular weight	**208**	**328**

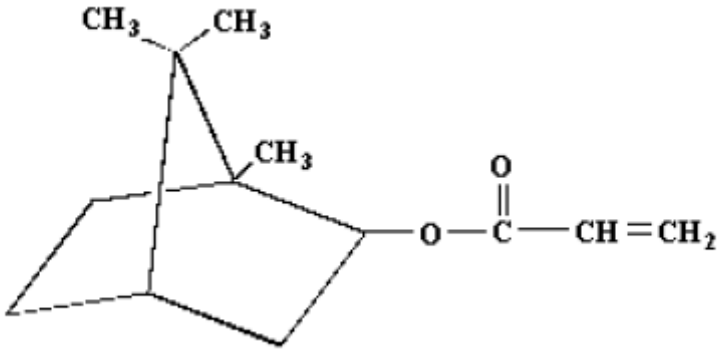

Isobornyl acrylate (IBA)

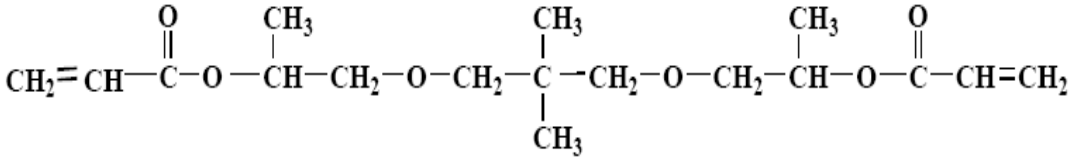

Propoxylated neopentyl glycol diacrylate (PNPGDA)

Figure 2. 7 Material properties and chemical structure of Isobornyl acrylate (IBA) and Propoxylated neopentoglycol diacrylate (PNPGDA)

Irgacure 184	
Appearance	**White to off-white Crystalline powder**
Melting point (^{o}C)	**45-49 ^{o}C**
Specific gravity (water=1)	**1.1-1.2**
Molecular weight	**204.3**

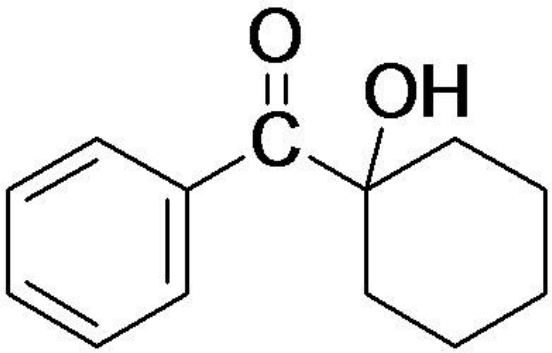

Figure 2. 8 Material properties and chemical structures of Irgacure 184

References

1. G. Liang, “Turbine airfoil cooling system with enhanced tip corner cooling channel”, *US Patent* 0085193, 2008.
2. D. J. Frasier, M. Kush, M. E. Schlienger, and M. Baldwin, “Method and apparatus for production of a cast component”, *US Patent* 6932145, 2005.
3. P. R. Beeley, R.F. Smart, *Investment Casting*, The university press, Cambridge, UK, 1995, 65.
4. J. W. Halloran, “Freeform fabrication of ceramics,” *Br. Ceram. Trans. J*., *98*, 299, 1999.
5. P.F. Jacobs, Rapid Prototyping & Manufacturing– Fundamentals of Stereolithography, SME, La Crescenta, California, 397, 1992.
6. M.L. Griffith, “Stereolithography of Ceramics”, Ph.D. Thesis, University of Michigan, 1995.
7. M. L. Griffith, J. W. Halloran, “Freeform fabrication of ceramic via stereolithography,” *J. Am. Ceram. Soc*., *79* [10], 2601, 1996
8. S.P. Pappas, “Radiation Curing of Printing Inks”, in Radiation Curing: Science and Technology, Pappas, editor, Plenum Publishing, New York, NY, 1-19, 1992
9. J.P. Fouassier, “An Introduction to the Basic Principles in UV Curing”, in Radiation Curing in Polymer Science and Technology, Vol. I, Fouassier and Rabek, editors, Elservier Applied Science, London, 49-117, 1993
10. A.J. Bean, “Radiation Curing of Printing Inks”, in Radiation Curing: Science and Technology, Pappas, editor, Plenum Publishing, New York, NY, 301-32, 1992
11. C.E. Hoyle, “Calorimetric Analysis of Photopolymerization”, in Radiation

Curing: Science and Technology, Pappas, Plenum Publishing, New York, NY, 57-134, 1992

12. G.B. Rothenberg, “Refractory Materials”, 1-11, NDC, Park ridge, New jersey, 1976

13. C.A. Schacht, “Refractories Handbook”, 1-10, MD Inc., Pittsburgh, Pennsylvania, 2004

14. D.W. Richerson, “Opportunities for Advanced Ceramics to Meet the Needs of the Industries of the Future”, Metal casting Industry, chap. 8, 1998

15. S. Banerjee, “Monolithic Refractories”, 1-18, World Scie., Illinois, 1998

16. E.W. Washburn, “Refractory Materials as a Field for Research”, J. Am. Ceram. Soc., 2[1], 3-31 (1919)

CHAPTER 3

INFLUENCE OF PARTICLE SIZE DISTRIBUTION (PSD) ON REFRACTORY SILICA USED IN CERAMIC STEREOLITHOGRAHY (CerSLA)

Ceramic stereolithography (CerSLA) requires a highly loaded but fluid suspension of ceramic powders in a photopolymerizable solution to produce a dense, uniformly particle dispersed green body after solidification and sintered body after firing. In the current work, a suspension of refractory grade powders dispersed in monomer has been used to make ceramic casting molds in ceramic stereolithography (CerSLA), which increases creep resistance and prevent severe dimensional change at high temperature. However, suspensions of coarser or denser particles can undergo differential sedimentation, leading to particle size segregation in which the population of larger or denser particles is greater near the bottom. The particle segregation in a layer should be removed to produce a dense, uniform sintered ceramic mold. This chapter describes the influence of particle size distribution (PSD) of refractory silica on the viscosity of ceramic suspension and the segregation in layers solidified by ceramic stereolithography (CerSLA).

3.1 INTRODUCTION

Ceramic stereolithography (CerSLA) builds ceramic green objects from CAD files from many thin liquid layers of powder in monomer, which are solidified by polymerization with a UV laser, thereby "writing" the design for each slice. Given the easy and convenient process of CerSLA, it has been widely used as the one of the most popular methods for free form fabrication that builds complex ceramic objects without the use of molds or tooling. In the this work, CerSLA is used to build silica based refractory molds as complex "integrally cored ceramic molds" (ICCM), which are novel investment casting shell molds with the core already in place. Ceramic casting molds have been made from refractory grade powders to increase creep resistance and prevent severe dimensional change of ceramic mold from high temperature of casting metal.

In CerSLA, the properties of the ceramic suspension directly relate to the processing time and quality of complex ceramic objects produced, CerSLA requires a highly loaded but fluid suspension of ceramic powders in a photopolymerizable solution.[1] Suspensions require a fairly high solid fraction of ceramic powder to be dispersed (usually > 50 vol %) in a monomer of liquid state, depending on the monomer and the powder. The goal in the CerSLA suspension is to increase the solids loading while lowering the viscosity and maintaining sufficient stability against aggregation and agglomeration of the particles.

The rheology of concentrated suspensions is governed by the effect of different factors; interparticle forces, Brownian motion of the particles, hydrodynamic interactions, as well as physical characteristics of the particles such as volume fraction of solids and

particle size distribution (PSD).[2] Among the several factors affecting the rheology of concentrated suspensions, particle size polydispersity rend a significantly lower viscosity than the one containing only mono-sized particles.[3,4] The viscosity of a suspension diverges at the maximum packing fraction where the behavior of the system transits from a liquid to a solid-like behavior. Farris firstly showed that PSD strongly affected the viscosity and solid loading of slurry.[5] For example, suspensions made of multimodal spherical particles have up to 50-fold reductions in shear viscosity, whilst maintaining the same solid volume fraction. Modifying PSD enables to increase the maximum solids loading without increasing viscosity. In the model, especially, the transition from monomodal to bimodal distribution displays the most significant effect on the reduction of relative viscosity among the multimodal PSD in the suspension.

Segregation in layers solidified by CerSLA should be considered to produce a dense, uniform sintered ceramic casting mold. Previous CerSLA work used submicron sized powders, the particles remain in suspension without settling for longer periods.[1,2] However, in this work, since refractory-grade powders were dispersed in the photopolymerizable monomer to impart stability at high temperatures, coarser or denser particles in suspension quickly sediment during building a layer, leading to particle size segregation in which the population of larger or denser particles is greater near the bottom.[6-8] Particle segregation through fast sedimentation of coarse powders resulted in two segregated areas, a particle dominated region and a liquid dominated region; each region is largely separated in the green body. After binder burn-out, when the liquid is removed from the liquid dominated region, property-degrading defects such as delamination, distortion, and excessive shrinkage develop within the remaining green

body. Thus, in order to maintain a homogeneous dispersion of particles in the green body, solid particle segregation in the liquid should be prevented during processing before the slurry is solidified.

There are several approaches for preventing segregation of particles. Using attractive interparticle forces to group particles together into agglomerates overcomes different sedimentation rates of individual particles, preventing segregation in colloidal processing (particle size ~ < 1μm).[9] However, agglomeration is not suitable for the refractory powders (particle size ~ 20 μm). Another approach is to control particle size and particle size distribution (PSD) in a liquid, wherein segregation of fast settling particles is hindered by interparticle forces such as repulsions with slower settling particles in the highly concentrated suspension.[10,11]

This paper demonstrates the viscosity of suspensions of refractory powders and segregation in layers resulting from the fast sedimentation of refractory powders and describes the effect of particle size distribution (PSD) on the suspension viscosity and segregation in layers solidified by ceramic stereolithography (CerSLA).

3.2 EXPERIMENTAL PROCEDURE

3.2.1 Characteristic of the fused silica powders

The suspension consists of irregular glassy silica powders (SiO_2, PCC airfoils, Sanford, NC) in monomer solution based on hexane diol diacrylate (HDDA, SR238, Sartomer Company, Exton, PA). HDDA is a Newtonian liquid with viscosity 9 mPa-s and density of 1.02 gm/cm^3. The silica powders were milled fused silica (density of 2.2 gm/cm^3). Blends of two powders were used such that Figures 3.1 and 2 show the particle size distributions of the coarse and fine powders. A particle size distribution and a volume distribution were determined by Laser diffraction pattern using Malvern Mastersizer 2000 Laser diffractor at Particle Technology Labs (PTL, Downers Grove, IL). The "coarse" powder had a particle size range with a finer decile d_{10} of 4 microns, median d_{50} of 27 microns, and upper decile d_{90} of 93 microns. The "fine" powder had a particle size range with finer decile d_{10} of 2 microns, median d_{50} of 7 microns, and upper decile d_{90} of 24 microns. The particle size of a bimodal powder computed from a binary mixture (50 wt% coarse: 50 wt% fine) is an average size range of 3 μm d_{10}, 12 μm d_{50} and 66 μm as d_{90}. The stokes settling velocity for the median particle in HDDA is 52 μm/sec for the coarse powder and 3.5 μm/sec for the fine powder.

3.2.2 Suspension preparation

A quaternary amine dispersant (CC-59, Goldschmidt,) in an amount equal to 3% of the weight of the SiO_2 powder was added to lower the viscosity and aid in ceramic dispersion. The photopolymerizable monomer and monomer mixture were prepared using

1,6-hexanediol diacrylate (HDDA, SR238) and ethoxylated pentaerythritol tetraacrylate (EPTA, SR494) as received from Sartomer company (Exton, PA). 1-Hydroxy cyclohexyl phenyl ketone (Irgacure 184, Ciba Specialty Chemicals, Tarrytown, NY) used as a photoinitiator decomposed on UV- radiation, releasing free radicals, which initiated the polymerization reaction of monomer mixtures. SiO2 powder and CC-59 as a dispersant for stable colloidal dispersion were added to UV-curable monomer mixtures without photoinitiator to prepare the ceramic suspensions. Up to a solid loading of 40 vol%, the suspension was mixed and homogenized in a high speed shear mixer for 5 min. At a solid loading of 50 vol%, more time was required for the dispersants to adsorb and colloidally stabilize the suspension, the mixtures were ball-milled for 24h. Hydroxy cyclohexyl phenyl ketone (HK) at a concentration of 2 wt% with respect to the monomer was added to a 50 vol% suspension and the final mixture was ball-milled again for 2h.

3.2.3 Rheological measurement and Tap density

Five groups of suspensions with total solid loading of 60 volume percent silica were prepared by the addition of “coarse” (C) powder into “fine” (F) powder; F100 wt%, F75-C25, F50-C50, F25-C75, and C100 wt%. The suspensions were formulated at 60 volume percent silica, using a quaternary amine dispersant (CC-59, Degussa, Parsippany, NJ) as a colloidal dispersant. A photointiator 1-Hydroxy cyclohexyl phenyl ketone (Irgacure 184, Ciba Specialty Chemicals, Tarrytown, NY) was added at 2 wt % to render the monomer photopolymerizable. The viscosity of the five suspensions was measured with a rheometer (Model CS-50, Bohlin, East Brunswick, NJ) in a parallel plate settling at shear rate of 0.1-100 sec^{-1}. All experiments were conducted at 25^{o}C and the sample

temperature was controlled to within ±0.1^{o}C using water as the heat transfer fluid.

Tap density is used to determine how particles are packed, which shows the effect of packing fraction on the viscosity. In this study, tap densities of five samples were determined from the mixture of dry "coarse" powder and dry "fine" powder; F100 wt%, F75-C25, F50-C50, F25-C75, and C100 wt%. For each tap density measurement, approximately 1.2g of power was poured into the graduated cylinder, and vibrated using mini mixer for 5 minutes before measuring volume. The tap density of a powder was calculated by

$$\text{Tap density} = \frac{\text{mass of powder}}{\text{bulk volume after vibration}} \quad \frac{\text{g}}{\text{cm}^3} \qquad 3.1$$

3.2.4 Photocuring of layers

Layers were produced in a commercial stereolithography apparatus (SLA-250, 3D Systems, Inc. Valencia CA), by dipping a substrate into a reservoir of well-stirred suspension to make 250 micron thick liquid layers. After a delay time of either 40 seconds or 300 seconds, the layer was solidified within 4 seconds by scanning the surface in a raster pattern at 1369 mm/sec with a UV laser beam focused in a diameter spot size of 120 microns. The UV radiation was provided by using diode-pumped solid state lasers in quasi-CW 355 nm air-cooled format (Xcyte, JDS Uniphase, Milpitas, CA). The experiments were conducted for the coarse powder and for a bimodal mixture of 50 wt% fine powder and 50 wt% coarse powder.

3.3. THE EFFECT OF PARTICLE SIZE DISTRIBUTION ON THE VISCOSITY OF CERAMIC SUSPENSION

Suspensions containing the highest possible fraction of particles are required to avoid excessive shrinkage during binder burn-out and densification. For lower volume percentages, the suspensions are more fluid. However, the addition of more powder results in a more viscous suspension. In ceramic stereolithography (CerSLA), a ceramic suspension should be fluid enough to decrease processing time, while increasing the quality of complex ceramic objects in the build process. For this reason, an upper limit to the viscosity for feasibility of CerSLA should be satisfied. Given the HDDA monomer viscosity of 9 mPa-s, the viscosity and relative viscosity of suspension in CerSLA is considered to be 3 Pa-s and 333, respectively. Figure 3.3 shows the relative viscosity versus the particle size distribution (PSD) with a constant solid loading of 60 vol%. The suspension's viscosity and relative viscosity at 100% "coarse" silica powder with median d_{50} of 27 microns is 6.3 Pa-s and 742 for a shear rate of 10 s^{-1}. Those viscosities did not be included into the upper viscosity limit of ceramic suspension. However, the viscosity abruptly decreased as coarse powder was replaced by "fine" powder with median d_{50} of 7 microns. Viscosity and relative viscosity of a silica suspension containing 75 wt% fine powders was decreased down to 1.2 Pa-s and 139, thus satisfying the upper limit to the viscosity of ceramic suspension.

The flow of suspension has two end member ideal cases; 1) Flocculated suspensions, where the particles are aggregated into structures (Floccs). The viscosity of flocced suspension is much higher because the aggregate must be disrupted by the floccs.

Flocced suspensions are typically shear-thinning because increasing flow rate progressively disrupt the aggregates. Colloidal forces dominate the viscosity of flocked suspension. 2) Dispersed suspensions, where the particles are not aggregated but faster flow dispersed single particles. The viscosities of dispersed suspensions are limited only by hydrodynamic effects, as the liquid flows around the solid particles. For dilute suspensions, the hydrodynamic viscosity is given by the Einstein equation, which can be derived exactly. At higher concentration, various corrections to the hydrodynamic viscosity have been proposed.

The Krieger-Dougherty (K-D) Equation is a popular expression for the Newtonian hydrodynamic viscosity at high volume fraction ϕ.[12] The relationship between viscosity and solid loading is well described by a relative viscosity as a function of volume fraction:

$$\eta_r = \frac{\eta(\phi)}{\eta_0} = \left(1 - \frac{\phi}{\phi_0}\right)^{-n} \qquad 3.2$$

where η_γ is the relative viscosity of the suspension, η_0 is the viscosity of the liquid, n is an exponent, and ϕ_0 is K-D limit, the particle volume fraction where the particles are "jammed". Ideally the K-D limit is related to the maximum packing fraction for particles (ϕ_m), so $\phi_0 \sim \phi_m$. The K-D exponent n ideally is $2.5\phi_0$. Equation 3.2 indicates that the suspension viscosity is abruptly increased as the particle volume fraction approaches its maximum volume fraction or packing fraction ϕ_m. Therefore, increasing the maximum volume fraction, ϕ_m, decreases the viscosity of a suspension at a given ϕ.

It is well known that the maximum packing fraction ϕ_m depends on particle size distribution.[13,14] For example, ϕ_m=0.63 for uniform sphere, ϕ_m=0.72 for optimal binary mixtures (7:1 size ratio, certain mass ratio), ϕ_m=0.78 for optimal ternary mixtures. These relationships have been extensively treated for ideal mixer spheres and for realistic irregular particles.

The influence of PSD on viscosity in hydrodynamic limit of dispersed particles is known as the Farris effect. The maximum solid loading in the Farris effect can be expressed in terms of the concentration of fine and coarse particles

$$\phi_1 = \frac{V_1}{V_0 + V_1} \qquad \phi_2 = \frac{V_2}{V_0 + V_1 + V_2} \qquad 3.3$$

where V_0 is the volume of suspending liquid, V_1 the volume of fine powder, and V_2 the volume of coarse particles in the suspension. Total concentration ϕ_m and the relative viscosity of the suspension, can be expressed as

$$\phi_m = \phi_1 + \phi_2 - \phi_1\phi_2 = \phi_2 \text{ if } \phi_1 = 0 \qquad 3.4$$

$$\eta_r = H(\phi_1)H(\phi_2) = H(\phi_2) \text{ since } H(\phi_1) = 1 \text{ if } \phi_1 = 0 \qquad 3.5$$

where ϕ_1 is the effective volume concentration of the fines and ϕ_2 the effective volume concentration of the coarse. $H(\phi_1)$ and $H(\phi_2)$ are some functions which can be determined either by theoretical modeling or experiments. With equation 3.5, Farris[5]

calculated the relative viscosities for bimodal systems versus blend ratio for a number of concentrations, as shown in Figure 3.4. Modifying the PSD from monomodal to bimodal distribution (point P to Q) does not only decrease the relative viscosity of original suspension from 1000 to 15 while the same total concentration of solids was dispersed, but it also shows that the bimodal PSD (point P to S) allows the solid loading to be increased from 60 to 75% without increasing viscosity. This effect considerably influences the viscosity at a total phase volume of more than 50%. Increasing higher solid loading of suspensions with minimal viscosity increase is more important in ceramic processing, allowing higher ceramic green density and improved sinterability.

Figure 3.5 shows the effect of particle size distribution on the tap density obtained with the mixture of fine and coarse powder. The tap density at 100% "coarse" silica powder with median d_{50} of 27 microns is 0.74 ± 0.03 g/cm^3. However, as "coarse" powder was replaced by 75 wt% "fine" powder with median d_{50} of 7 microns, the tap density increased to 0.93 ± 0.02 g/cm^3. As shown in Figure 3.5, the tap density increases by the transition from monomodal to bimodal distribution, which represents closely packed particles so that the higher maximum volume fraction, ϕ_m, is reached. Equation 3.2 already showed that increasing the maximum volume fraction, ϕ_m, decreases the viscosity of a suspension at a given ϕ. Therefore, higher tap density induced by the bimodal particle size corresponds to higher maximum volume fraction, which reduces the relative viscosity shown in Figure 3.3.

3.4. THE EFFECT OF PARTICLE SIZE DISTRIBUTION ON THE SEGREGATION IN A LAYER

This section describes the influences of particle size distribution (PSD) of refractory silica in terms of segregation in layers via solidification by ceramic stereolithography (CerSLA). Using bimodal PSD, a significant decrease in the suspension viscosity is achieved as compared to a suspension of a mono-modal PSD. Large segregations in solidified layers are detected when the settling time is long and the PSD is mono-modal. However, much less segregation occurs with bimodal PSD due to suppressed segregation. To determine the distribution of particle size within each layer, a linear intercept method is used, which quantifies the vertical changes in PSD. Initial spatially-resolved particle size distribution results contained a great deal of scatter and variation.

3.4.1 Spatially resolved size distribution using Diagnostic with Comb Marker

In order to characterize the effect of particle size distribution on the segregation of ceramic powder in each layer, each layer should be individually detected and analyzed. However, it is difficult to distinguish each layer due to the continuous layers along the Z-axis, thus affecting to the accurate analysis on the particle size distribution in a layer. As shown in Figure 3.6, we design a Diagnostic with Comb Marker (DCM) like our teeth to easily separate each layer. The diagnostic is composed of 40 layers stacked by two different structures; a first fully cured layer and a second partially cured layer which has two uncured parts at the both side regions and a fully cured part in the center region.

These layers are continually aligned in turn, thus able to determine the top and bottom of each layer with an accuracy of 10 microns.

After 40 layers were built, the object was removed from the SLA apparatus and sectioned normal to the direction of the layers using a diamond wafering saw. Careful grinding and polishing was conducted to reveal the cross-section of the microstructure. Figure 3.7 shows the cross-section of comb-shaped object showing the microstructure of particles dispersed in a layer with 250 microns thickness in the green body built used 52 vol% coarse silica powder. When a green body is fabricated, holding time of 300 seconds is used prior to building a next layer. Severe segregation resulting from the fast sedimentation of coarse silica powder exists in the layers, which are separated to the two main phases composed of a polymer and a silica powder dominated phase; particle free zone at the top of a layer and segregated coarse SiO_2 powders (circles) at the bottom of a layer.

Given the segregation shown in Figure 3.7, the linear intercept is used to represent particle size distribution in a layer, as shown in Figure 3.8. A layer with the thickness of 250 microns was sliced by nine 28 micron intervals. Given the linear intercept method[15] on a layer, the nine intervals including various sizes of particles were denoted from I (Top) to A (Bottom), where two totally separated regions of a particle free zone at the top (I) and segregated coarse SiO_2 powders at the bottom (Z) in a layer are included. Given the figure 3.7, Table 3.1 demonstrates size and number of particles measured from nine 28 micron intervals (A to I) in a layer. Most of particles larger than 40 microns are located below the position E (height of 112 to 140 microns) and a particle with the largest diameter of 82.9 microns was detected at the position B (height of 28 to 56 microns). On

the other hand, no particle larger than diameter of 40 microns exists above the position G (height of 168 to 196 microns).

Given the results in Table 3.1, Figure 3.9 shows particles dispersed in a position of a layer. Since the layers were small, only 5-20 particles in each 28 micron interval, the scatters within the distributions were considerable. Using repeated linear intercept method measures particle size of coarse powder segregated in cross section of comb-shaped object shown in Figure 3.7. Figure 3.10 shows particle size distribution in 4 sequential layers obtain from the cross section of comb-shaped object. Although particles are dispersed like random noise, 4 sequential layers show a repeated pattern on the particle size variation in layer; more fine powders on the top and coarser powders on the bottom.

3.4.2 Effect of particle size distribution (PSD) on the segregation

Given the effect of PSD on viscosity, using a bimodal powder (solid loading of 60 vol%) allows for a more concentrated suspension than can be made using coarse powder s (52 vol%) at similar viscosity (~ 1 Pa·sec). Figures 3.11 (a) and (b) are the cross sections of comb-shaped objects fabricated using both coarse powders and bimodal powders respectively (50% fine and 50% coarse powders), which takes holding time of 300 seconds before the next layer of the comb-shaped object is built.

Figure 3.11 (a) shows a microstructure image representing severe segregation resulting from the fast sedimentation of coarse silica powder in the layers and a plot of particle size distribution versus position in combined 4 layers. As shown in Figure 3.7, there is bad segregation with two totally separated regions: a particle free zone at the top

and segregated SiO_2 powders at the bottom of each layer. Given the line intercept method on the nine intervals in a layer, the particle size distribution versus position shown in Figure 3.11 (a) confirms that there is segregation of particles in each layer. Although each layer exhibits particle size variation, the particle size distribution is widely affected by the size difference of coarse vs. fine powders. Powders much smaller than 10 microns and consisting of pure resin are found at the top region of the first layer, but larger sized powders of about 80 microns exist in the bottom region.

Figure 3.11 (b) shows the microstructure of a cross section of a green body built using bimodal PSD. As expected, much less segregation is detected due to the shorter sedimentation time of the coarse silica powders. Although these powders are dispersed in a layer with a large random noise of particle size distribution, they mainly range in size from 20 to 50 microns and are dispersed evenly in a layer. Consequently, the segregation pattern is not visually obvious.

Bad segregation or much less segregation in layers is directly related to the sedimentation velocity of ceramic powder. In a dilute suspension, the sedimentation velocity, v_{stokes}, of a single particle in a fluid of viscosity η is calculated by Stoke's law:

$$v_{stokes} = \frac{1}{18}\frac{(\rho_c - \rho_f)gd^2}{\eta} \qquad 3.6$$

where d is the diameter of ceramic powder, ρ_c the density of ceramic powder, ρ_f the density of fluid, and g the acceleration due to gravity. Equation 3.6 shows that the settling rate of a single particle is greatly accelerated by an increase in the particle size

(proportional to d^2), and retarded by an increase in the liquid viscosity. However, in a concentrated suspension, the Stokes velocity is modified since hindered settling occurs and reduces the settling velocity of a particle, resulting in a longer residence time for the interaction between a particle and its neighboring particles in the hindered region where there is a higher solids concentration.

In a highly concentrated suspension with a more than 50 solid volume percent of silica, large particle sizes of fused silica used in this work were governed by the hydrodynamic interaction forces and gravitational force so that the settling velocity of large particle sizes is calculated by the Richardson-Zaki (R-Z) equation.[16] This equation is widely accepted to correlate the superficial fluidizing velocity ν_g and the particle volume fraction ϕ of fluidized beds and suspensions of non-agglomerated particles:

$$\begin{aligned} v &= v_{stokes}(1-\phi)^n \\ &= \frac{1}{18}\frac{(\rho_c-\rho_f)gd^2}{\eta}(1-\phi)^n \end{aligned} \qquad 3.6$$

Where ρ_c and ρ_f are the density of the solid ceramic particle and the monomer liquid, g is the gravitational acceleration, d is diameter of ceramic powder, η is the fluid viscosity, ϕ is the concentration of solid, respectively. The exponent n is an empirical parameter whose value has been a discrepancy. For example, Richardson and Zaki reported n = 4.65 in the small particle Reynolds number (Re_t) regime, while n decreased as Re_t increased.

The concentration of solid in Equation 3.6 is considered to the main reason of the bad segregation and much less segregation, as shown in Figure 3.11. As already

mentioned above, using a bimodal powder (solid loading of 60 vol%) allows for a more concentrated suspension than can be made using coarse powder (52 vol%) at similar viscosity (~ 1 Pa·sec). The particle size of a bimodal powder (50 wt% coarse: 50 wt% fine) is an average size range of 3 microns as d_{10}, 12 microns as d_{50} and 66 microns as d_{90}. The "coarse" powder had a particle size range with a finer decile d_{10} of 4 microns, median d_{50} of 27 microns, and upper decile d_{90} of 93 microns.

In order to apply two phenomena of bad segregation and much less segregation to Equation 3.6, median deciles d_{50} of a coarse powder and a bimodal powder were selected as a diameter of particles. Diameters and solid loading of a coarse powder are 27 microns and 52 vol%, while a bimodal powder has diameter of 12 microns and solid loading of 60 vol%. Equation 3.6 is used to calculate the settling velocity for a coarse powder or a bimodal powder. In the case of a coarse powder inducing bad segregation, the coarse powder with diameter of 27 microns has the settling velocity of 0.84 microns/sec. On the other hand, in the other case of a bimodal powder showing much less segregation, the settling velocity for a bimodal powder with diameter of 12 microns was 0.06 microns/sec.

Given the solid loading and settling velocity according to the powders, Table 2 shows the settling distances of the coarse or bimodal powder for 300 seconds. The settling distance is $\nu * \tau$, where τ is the time delayed to build a next cross section of a green body. The settling distance of the coarse powder is 252 microns, while the bimodal powder settles 18 microns. Using the bimodal powder increases the solid concentration and decrease the median particle size, thus modifying the sedimentation velocity of fused silica powder. Therefore, slow settling velocity in the bimodal powder leads to less settling distance, which prevents segregation in a layer. No segregation or much less

segregation exists in layers when bimodal powders are used to suppress segregation.

3.5 Conclusion

The suspension viscosity and segregation in layers solidified from suspension prepared from refractory silica was investigated as a function of particle size distribution (PSD). In the case of bimodal mixture, relative viscosity of suspension is significantly decreased by the increase of the maximum solid loading resulting from the presence of small particles between the larger ones. The transition from monomodal to bimodal distribution increases maximum volume fraction, ϕ_m, thus exerting the most significant effect on the reduction of relative viscosity among the multimodal PSD in the suspension. The reduction of relative viscosity, shown in Figure 3.3, is a result of the increase of the maximum volume fraction induced by the bimodal particle size distribution.

The use of a linear intercept method can determine the distribution of particle size within each layer to quantify the vertical changes in PSD. The distribution of particle size vs. position in each layer shows clear segregation patterns in the case of long settling time and mono-modal PSD. However, subtle patterns can be seen visually due to a great deal of scatter and variation in the spatially-resolved particle size distribution in the other conditions. Severe segregation associated with mono-modal PSD is suppressed by using bimodal PSD. In a concentrated suspension, the Stokes velocity is modified since hindered settling occurs and reduces the settling velocity of a particle, resulting in a longer residence time for the interaction between a particle and its neighboring particles in the hindered region where there is a higher solids concentration. The median diameters

of the coarse powder or the bimodal powder are used to calculate the settling velocities. In the case of a coarse powder inducing bad segregation, the settling velocity of 0.84 microns/sec was calculated from a coarse powder with diameter of 27 microns. On the other hand, in the other case of a bimodal powder showing much less segregation, the settling velocity for a bimodal powder with diameter of 12 microns was 0.06 microns/sec. Using a bimodal powder increases the solid concentration and decreases the particle size, thus modifying the sedimentation velocity of fused silica powder and preventing segregation in a layer due to slow settling velocity. No segregation or much less segregation exists in layers when bimodal powders are used to suppress segregation.

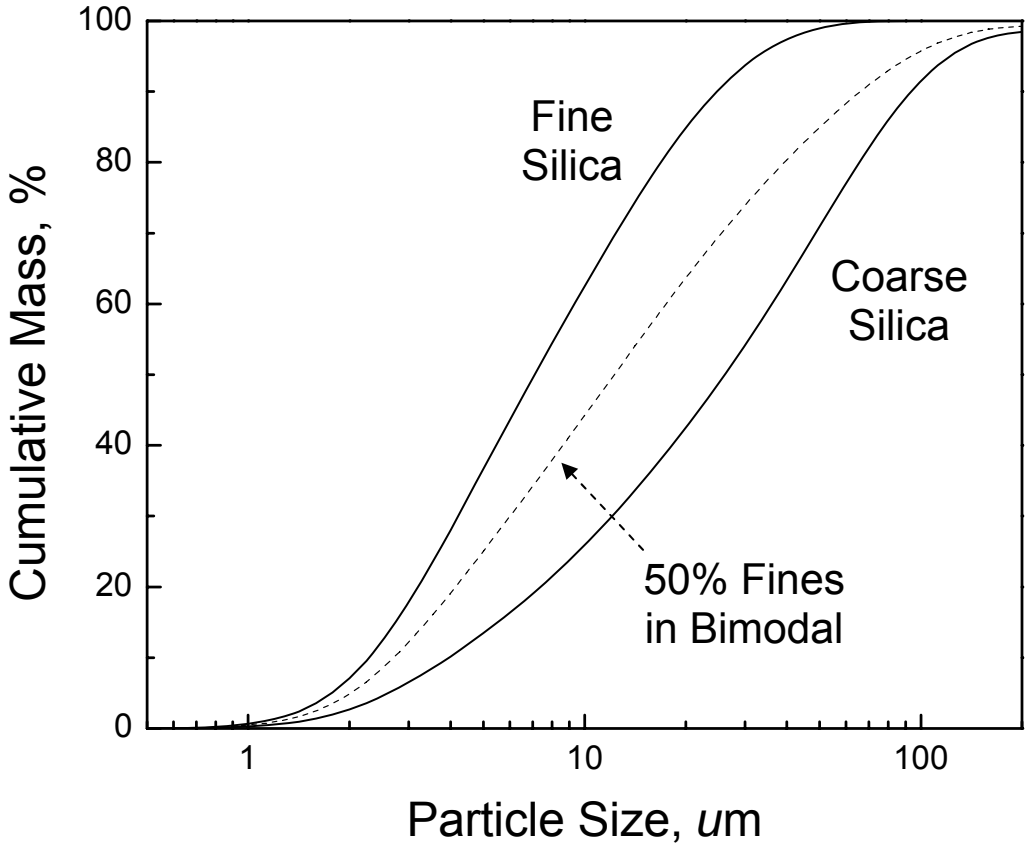

Figure 3. 1 Cumulative mass percent versus particle size distribution (PSD) of coarse and fine powders used to decrease the high viscosity of a 60 vol% coarse SiO_2 particles dispersed in the hexane diol diacrylate (HDDA)

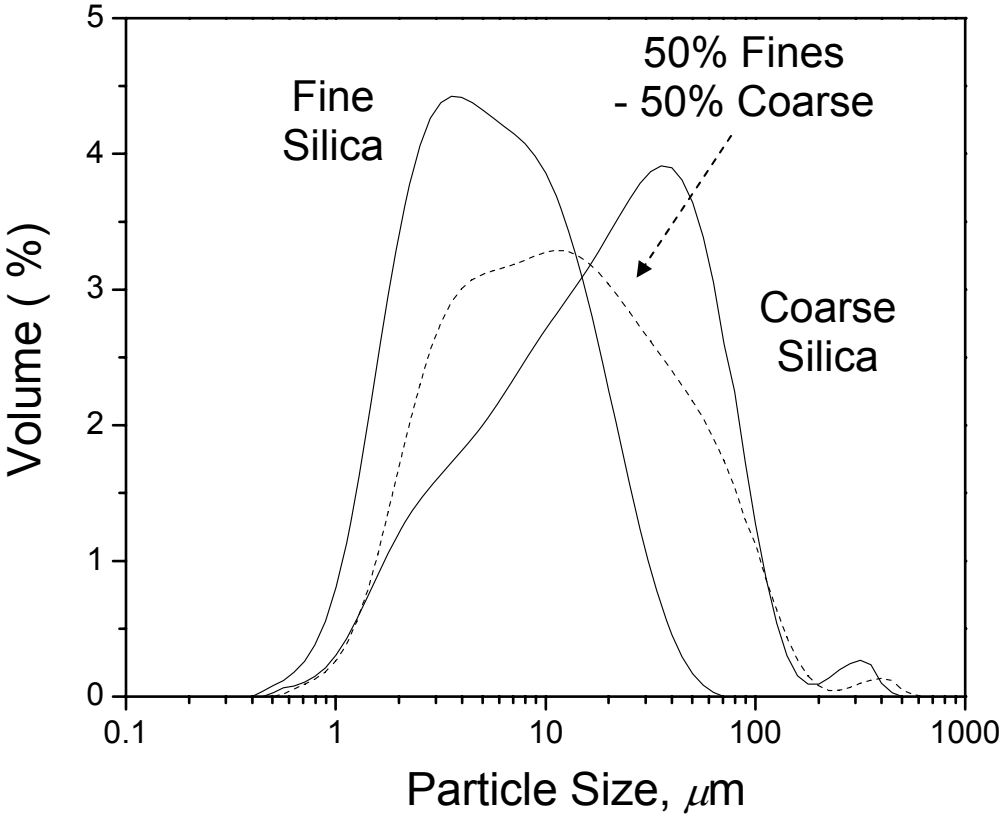

Figure 3. 2 Volume percent versus particle size distribution (PSD) of coarse and fine powders used to decrease the high viscosity of a 60 vol% coarse SiO_2 particles dispersed in the hexane diol diacrylate (HDDA)

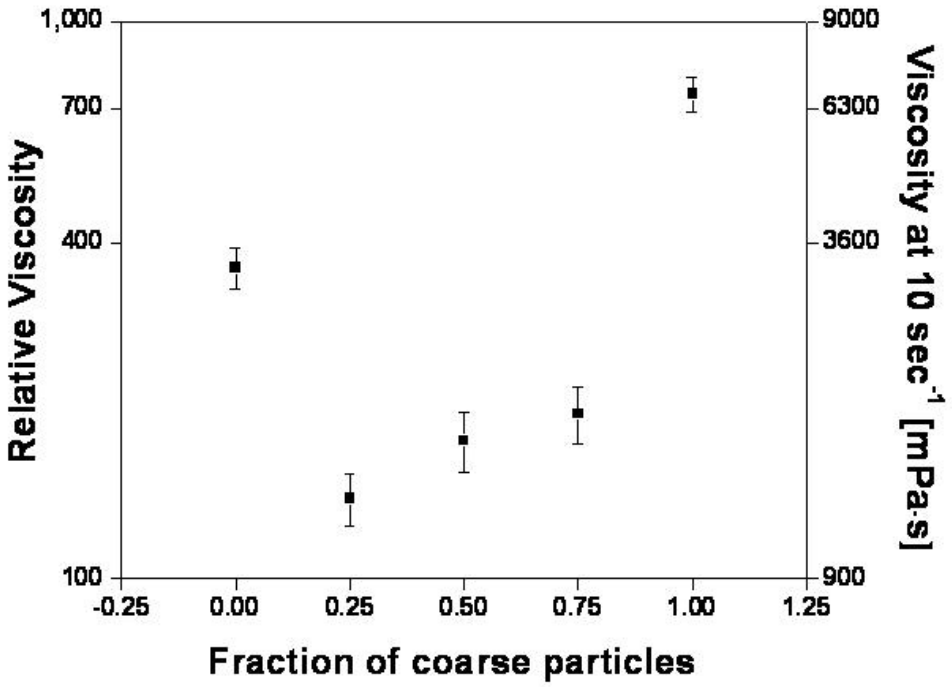

Figure 3. 3 The effect of particle size distribution on the relative viscosity of suspension. 60 volume percentage of silica dispersed suspensions are prepared by two different particle sizes; coarse (d_{50}:26 μm) and fine (d_{50}:7 μm) fused silica suspensions.

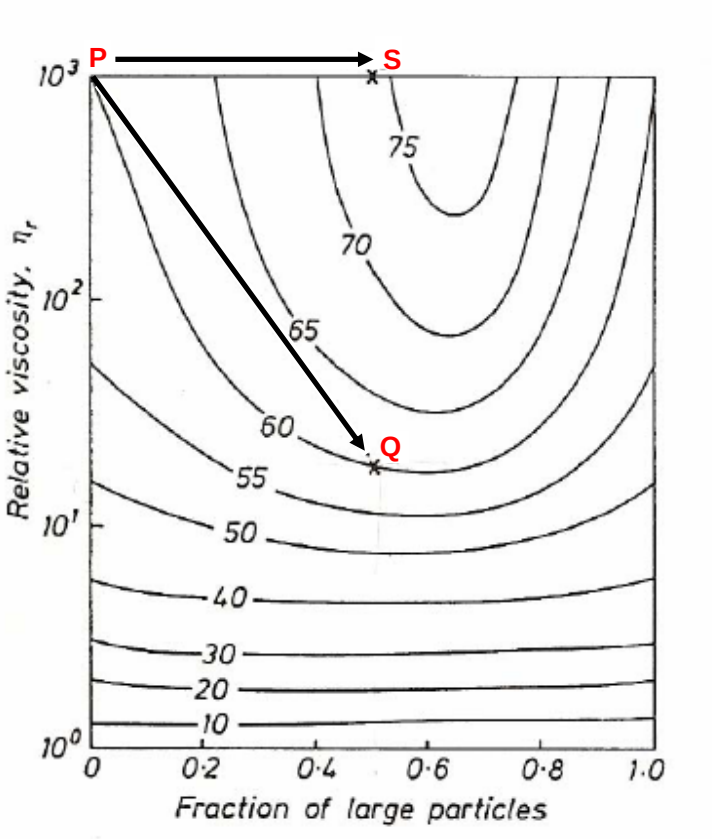

Figure 3. 4 Dramatically decreased relative viscosity can be explained by the Farris effect; Line PQ exhibits a 50% reduction in viscosity at the same solids loading. Line PS: An increase in the solids loading, from 60 to 75%, without an increase in viscosity.

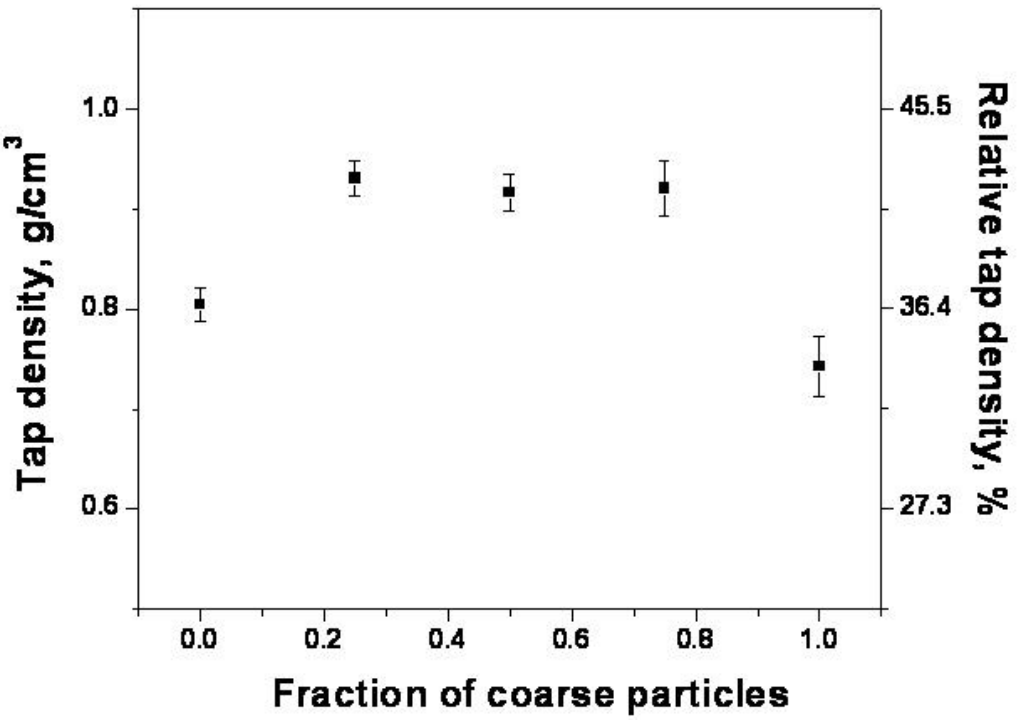

Figure 3. 5 The effect of particle size distribution on the tap density obtained with the mixture of two different particle sizes; coarse (d_{50}:26 μm) and fine (d_{50}:7 μm) fused silica suspensions.

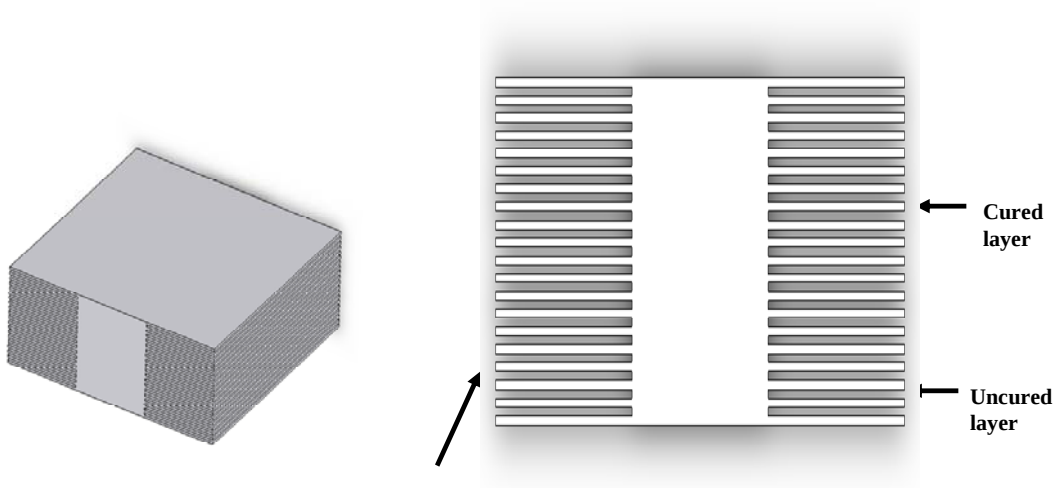

Figure 3. 6 Comb-shaped object to detect segregation in a layer: Comb marker like our teeth is used to distinguish layers.

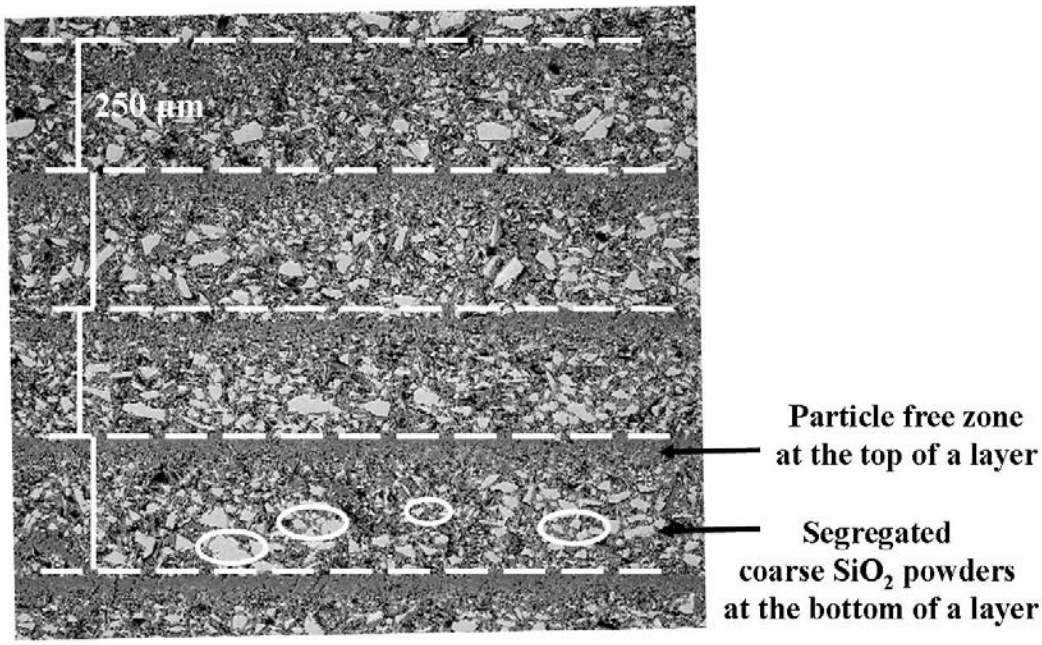

Figure 3. 7 The cross-section of the microstructure from a comb-shaped object showing the segregation of coarse powder in a layer having 250 μm thickness in a green body built used 52 vol% coarse silica powder: Particle free zone at the top of a layer and segregated coarse SiO_2 powders (circles) at the bottom of a layer. When a green body is fabricated, holding time of 300 seconds is used prior to building a next layer.

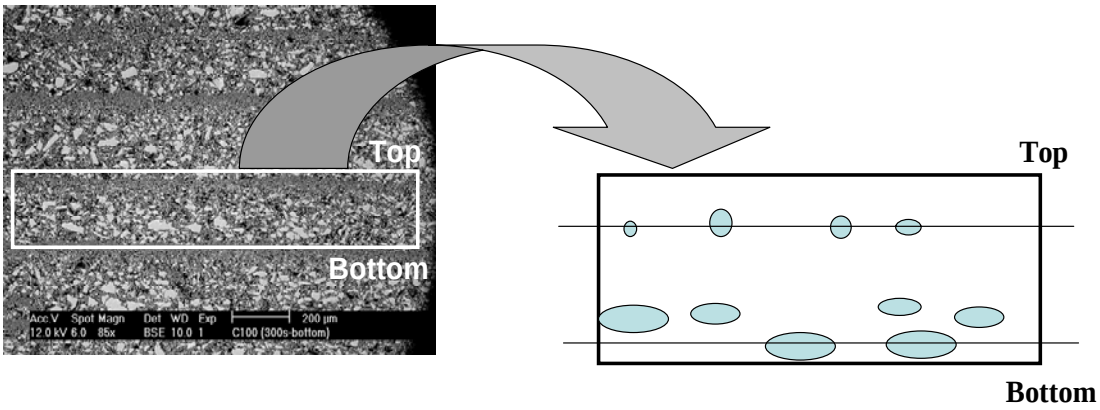

Figure 3. 8 Schematic diagram to represent particle size as a function of position in a layer. Average particle sizes are determined by line intercept in layers.

Table 3.1 Size of particles measured from nine 28 micron intervals from A (bottom) to I (top) in a layer with layer thickness of 250 μm and number of particle.

Position	Height [μm]	Particle size [μm]														
I (Top)	224-250	0.0														
H	196-224	8.9	9.5	11.4	13.9											
G	168-196	13.3	15.8	16.5	19.0	19.0	19.6	20.3	20.3	21.5	22.2	23.4	25.3	26.0	30.4	
F	140-168	19.0	19.6	20.9	22.2	25.3	26.0	28.9	30.4	31.7	33.5	34.6	37.3	43.0	44.3	46.2
E	112-140	23.4	26.0	27.9	29.8	32.9	35.4	36.1	38.0	39.6	40.8	42.9	44.3	44.3	45.6	50.0
D	84-112	25.3	30.4	31.7	31.7	38.0	38.0	38.0	47.5	53.2	57.0					
C	56-84	27.9	30.4	31.7	36.7	44.3	50.6	53.8	58.2	63.3	69.0	72.2				
B	28-56	31.7	32.9	38.0	39.2	39.2	41.1	44.3	57.0	60.8	64.6	76.0	82.9			
A (Bottom)	0-28	38.0	49.4	53.2	56.3	58.2	69.6	79.1								

Position	Height [μm]	Number of Particle								
I (Top)	224-250									
H	196-224	4								
G	168-196		8	6						
F	140-168		3	5	4	3				
E	112-140			4	6	5				
D	84-112			2	5	1	2			
C	56-84			2	2	2	2	2	1	
B	28-56				5	2	2	1	1	1
A (Bottom)	0-28				1	1	3	1	1	
		10	20	30	40	50	60	70	80	90
		Particle size [μm]								

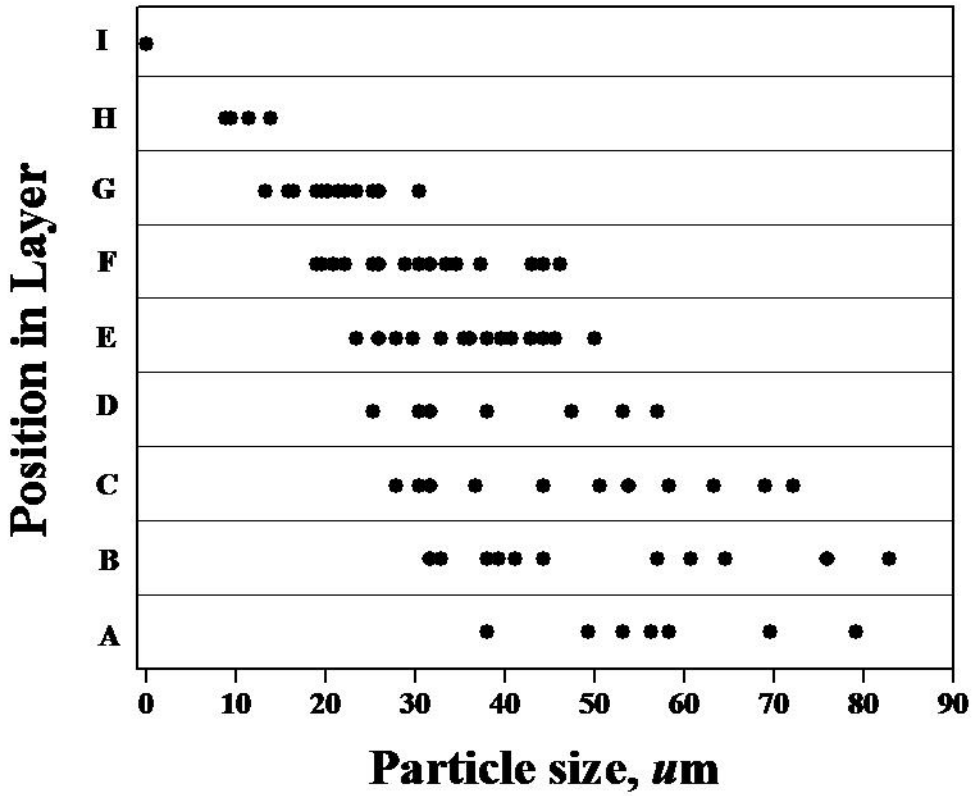

Figure 3. 9 Particle size versus position in a layer. Data for dispersed Particles contain random noise.

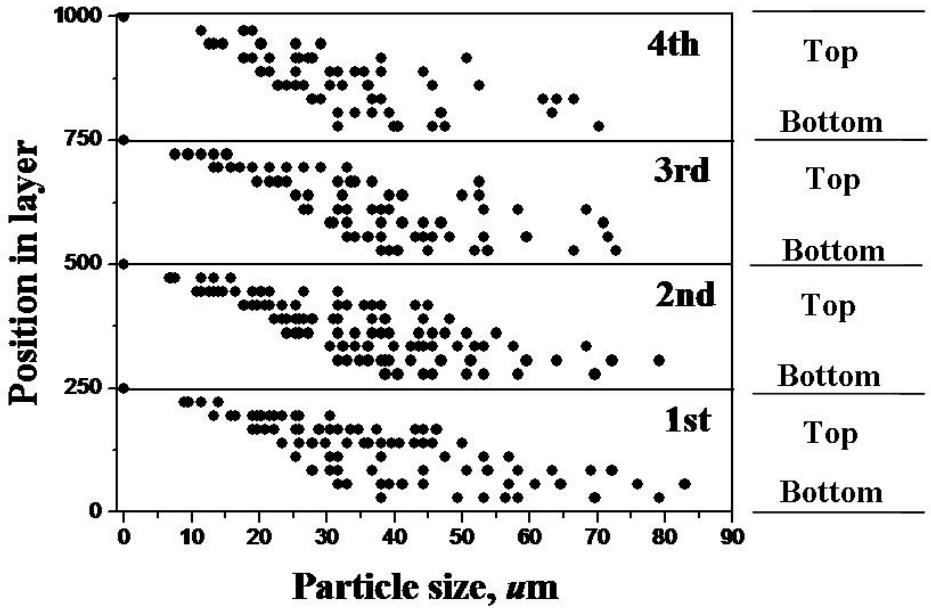

Figure 3. 10 Particle size versus position in combined 4 layers. Data for dispersed Particles contain random noise, but the particle size variation in a layer show a repeating pattern; more fine powders on the top and more coarse powders on the bottom.

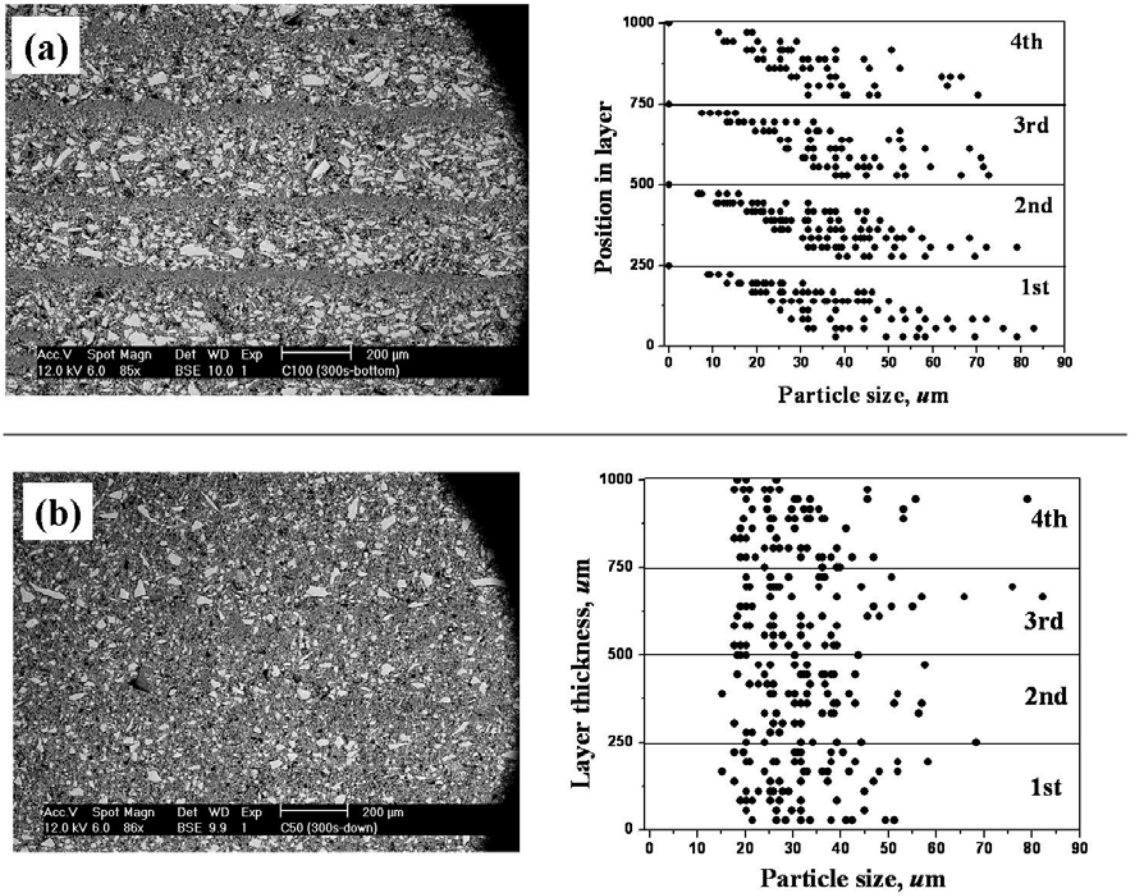

Figure 3. 11 The effect of particle size distribution (PSD) within a CerSLA layer as a function of segregation as represented by SEM images and data generated by line count method: (A) Coarse powder and (B) Bimodal powder; Layers in image (B) built use bimodal PSD to suppress segregation. When a green body is fabricated, holding time of 300 seconds is used prior to building a next layer.

Table 3. 2 The settling distance modified according to the particle size distribution (PSD)

	Coarse powder	Bimodal powder
d_{50}	27 μm	12 μm
Solid loading (%)	52	60
Settling velocity (μm/sec)	0.84	0.06
Time* (sec)	300	300
Settling distance (μm)	252	18

Time* : **the time delayed to build a next cross section of a green body**

References

1. M.L. Griffith, "Stereolithography of Ceramics", Ph.D. Thesis, University of Michigan, 1995
2. A. A. Zaman and C. S. Dutcher, "Viscosity of electrostatically stabilized dispersions of monodispersed, bimodal, and trimodal silica particle," *J. Am. Ceram. Soc.* **89** [2], 422-30 (2006).
3. C. Chang and R. Powell, "Effect of particle size distributions on the rheology of concentrated bimodal suspensions," *J. Rheol.,* **38**, 85-98 (1994).
4. R. Greenwood, P. F. Luckham, and T. Gregory, "Minimizing the viscosity of concentrated dispersions by using bimodal particle size distribution," colloids *Surf. A*, **144**, 139-147 (1998).
5. R. J. Farris, "Prediction of the viscosity of multimodal suspensions from unimodal viscosity data," *Trans. Soc. Rheol.,* **12**, 281-301 (1968)
6. H. A. Makse, S. Havlin, P.R. King, and H. E. Stanley, "Spontaneous stratification in granular mixtures," *Nature,* **386**, 379-382 (1997).
7. K. M. Hill, A. Caprihan, and J. Kakalios, "Bulk segregation in rotated granular material measured by magnetic resonance imaging," *Phys. Rev. Lett*., **78**, 50-53 (1997).
8. J. C. Williams, "The segregation of particulates materials. A review," *Powder Technol.,* **15**, 245-251 (1976).
9. B. V. Velamakanni and F. F. Lange, "Effect of interparticle potentials and sedimentation on particle packing density of bimodal particle distributions during pressure filtration," *J. Am. Ceram. Soc.,* **74** [1], 166-172 (1991).

10. M. A. Hassen and R. H. Davis, “Effects of particle interactions on the determination of size distributions by sedimentation,” *Powder Technol*., **58** [4], 285-89 (1989).
11. R. K. Roeder, G.A. Steinlage, K. P. Trumble & K. J. Bowman, “Preventing segregation during centrifugal consolidation of particulate suspensions: particle drafting,” *J. Am. Ceram. Soc.,* **78**, 2367-2373 (1995).
12. I. M. Krieger and T. J. Dougherty, “ A Mechanism for Non-Newtonian Flow in Suspensions of Rigid Spheres”, *Trans. Soc. Rheol*., **3**, 137-52 (1959)
13. C. C. Furnas, “Grading Aggregates: I, Mathematical relations for beds of broken solids of maximum density,” *Ind.Eng. Chem.,* **23** [9], 1052-58 (1931)
14. R. K. Mcgeary, “Mechanical packing of spherical particles,” *J. Am. Ceram. Soc.,* **44** [10], 513-22 (1961).
15. E. D. Case, J. R. Smyth & V. Monthei, “ Grain-size determinations,” *J. Am. Ceram. Soc.,* **64**, C 24-25 (1981).
16. J. F. Richardson & W. N. Zaki, “Sedimentation and fluidization: Part I,” *Trans. Inst. Chem. Engrs.,* **32**, 35-53 (1954).

CHAPTER 4

PROCESS MODEL FOR CERAMIC STEREOLITHOGRAPHY AND SEGREGATION MODEL

This chapter covers the aspects of predicting the process model to represent the relationship between the time to write a layer (τ_{write}) and several process parameters, and the segregation model to suppress the segregation in a layer when UV laser expose on the ceramic suspension to write a layer. The goal is to understand the fundamental aspects governing the ceramic stereolithography process, and establish the criteria for segregation resulting from the consideration of time to write a layer in acrylate-powder mixture and settling time. Given the process model and the segregation model, the stereolithography operator can easily select optimum variables and maximize the efficiency of ceramic stereolithography (CerSLA), thus able to suppress segregation in a layer.

4.1 PROCESS MODEL FOR CERAMIC STEREOLITHOGRAPHY (CerSLA): TIME TO WRITE A LAYER (τ_{write})

4.1.1 Process Parameters used in CerSLA

Ceramic stereolithography (CerSLA) builds ceramic green objects from CAD files from many thin liquid layers of powder in monomer, which are solidified by polymerization with a UV laser, thereby "writing" the design for each slice. A certain energy dose, E (J/cm^2) for the UV laser is required to cure the resin by photopolymerization. We used a cure depth (C_d) which is comparable to the layer thickness (λ). Faster laser velocity permits a shorter time required to write a layer (τ_{write}). Factors affecting to the writing time are the resin sensitivity (D_p) and the critical energy dose (E_c). The D_p which is a material-dependent and wavelength-dependent characteristic length and is defined as the resin "penetration depth" at the laser wavelength. For an energy dose, the cure depth (Cd) is given by the Jacob's version of the Beer-Lambert law[1]

$$C_d = D_p \ln\left(\frac{E}{E_c}\right) \qquad 4.1$$

where C_d is the absolute cure depth, D_p is the resin sensitivity representing the distance at which the laser intensity is reduced by 1/e, E_c is the critical exposure for the resin to gel, and E is the exposure or energy density at the surface.

The resin sensitivity for a ceramic resin depends on the solid volume fraction, particle size of ceramic powder, and refractive index of ceramic powder. When ceramic particles are added to the acrylate monomers, the ceramic particles in the suspension serve as scattering centers to the incoming radiation. The scattering in ceramic SLA resin

is dependent upon the ceramic solids loading and the refractive index difference between the ceramic powder and the medium, or $\Delta n = n_{ceramic} - n_0$.[2] The detailed description of scattering in concentrated suspension is complex. However, we can describe the essential relationship between resin sensitivity [D_p] and volume fraction powder [ϕ] with an approximation derived by Griffith[1,3]

$$D_p = \frac{2}{3}\frac{d}{Q}\frac{1}{\phi}\left(\frac{n_0}{\Delta n}\right)^2 \qquad 4.2$$

$$D_p = \frac{2}{3}\frac{d}{Q}\frac{1}{\phi}\left(\frac{n_0}{\Delta n}\right)^2 = \gamma\frac{\mathrm{d}}{\phi} \qquad 4.3$$

where d is particle diameter, Δn^2 is the square of the refractive index difference between the ceramic and the monomer [$\Delta n^2 = (n_c - n_0)^2$], ϕ the volume fraction solids, and Q is the scattering efficiency term. Note that Equation 4.2 is for a scattering dominated resin. The relationship between resin sensitivity and refractive index difference or solid loading with several refractory ceramics such as silica (n_{sio2}=1.56), alumina (n_{Al2O3}=1.72), and silicon nitride (n_{si3n4}=2.1) at the aqueous-based and HDDA-based system was previously measured.[1,3] Due to the large refractive index of alumina, alumina suspension has the smaller value of resin sensitivity than silica. These results illustrate the very important role of $1/\Delta n^2$ because Δn is the major parameter for different material. Thus for a certain ceramic material, which has a particular reflective index $n_{ceramic}$, the resin sensitivity will be strongly dependent upon the refractive index of the monomer, n_r. In addition, if the ceramic powder with the similar index is dispersed into monomer, the resin sensitivity is dominated according to the particle size of ceramic powder and solid volume fraction. Equation 4.2 can be simplified as a function of particle size of ceramic

powder and the solid volume fraction in Equation 4.3.

When a laser scans on the ceramic suspension to solidify a layer, the laser drawing speed is influenced by several variables including laser beam width, hatch spacing, and power of laser. With these parameters, the laser drawing speed is expressed by[4]

$$V_L = \frac{P_L}{h_s E} \qquad 4.4$$

where P_L is power of laser (mW), h_s is hatching spacing (cm), and E is the exposure or energy density at the surface at the surface (mJ/cm^2). Hatch space is the distance from the center of cured lines. Figure 4.1 shows laser power, layer thickness, and hatch space, which are apparatus parameters relating to the time to write a layer. When higher beam power, thinner layer thickness, and wider hatch space are used, it takes much shorter time to write a layer. Therefore, using apparatus parameters controls the beam speed to write a layer (τ_{write}), finally adjusting total build time (τ_b) for 3D complex shape.

4.1.2 Total Build Time (τ_b): Time to build an object

Total build time is the time required to produce an object with n layers, expressing the sum of the time for recoating τ_r and the time to write each layer τ_{write}[5]

$$\tau_{b,\,total} = n\,\tau_r + \sum_{1}^{n} \tau_{write} \qquad 4.5$$

where $\tau_{b,\,total}$ is the total build time, τ_r is the time for recoating each layer, and τ_{write} is the time to write a layer. The number of layers (n) is an important processing parameter, which is directly related to build time and surface finish.[6] For example, it take less time

to build a green body with thicker layers, but surface quality may be diminished by stair-stepping problems resulting from thicker layers existing on the non-vertical surfaces. The recoating time, τ_r, is limited by the three operations: dipping to prepare the fresh layer using the mechanical method, wiping away excess material using blade to make a flat surface, and the time required for the surface of the new layer to become smooth. All depend on the rheology of the suspension.

The viscosity of a suspension depends on the amount of solid volume fraction (ϕ) of the suspension. The lowest possible viscosity is the hydrodynamic limit when all particles are dispersed as single particles. For this case, the viscosity can be calculated by the Krieger - Dougherty model[7]

$$\eta = \eta_0 \left(1 - \frac{\beta\phi}{\phi_m} \right)^{-[\eta]\phi_m} \qquad 4.6$$

where η is the viscosity of the suspension and η_0 is the viscosity of the solvent. The variable ϕ_m is the theoretical packing factor and the true volume fraction of the powder dispersed in the suspension is represented by the variable ϕ. In equation 4.6, the viscosity remains low until the particle packing hinders the flow of the suspension, $\phi \rightarrow \phi_m$. The viscosity diverges as the concentration approaches ϕ_m, where this asymptotic value is used as an index of dispersion. For dispersed suspension, $\phi_m \rightarrow \phi_p$, the maximum packing of singlets where $\phi_p = 0.64$ for random packing of uniform spheres. If the suspension is highly flocculated, and the particles are agglomerated into flocs, ϕ_m is much less than ϕ_p. $[\eta]$ is the intrinsic viscosity of the suspension and a function of particle geometry. The term β is the effective packing factor of the ceramic powder. Since the effective packing factor is used to account for the thickness of the dispersant absorbed on

the particles, this factor is the important in the submerge particles.

The Krieger – Dougherty in equation 4.6 does not have an explicit particle size dependence, but the only variable is volume fraction. However, dispersed particles have a layer of adsorbed dispersant of finite thickness b. For similar particles in hexane diol diacrylate (HDDA) monomer, chu et al. found finite thickness of 13 nm.[8] The β factor can be estimated by the following expression;

$$\beta = (\frac{d+2b}{d})^3 \qquad 4.7$$

where d is the diameter of the particle and b is the adsorbed layer thickness. Figure 4.2 shows the value of effective packing factor (β) as a function of particle size such that β is dominated by the diameter of the particle as the size difference between diameters of the particle. For particles larger than 1 μm, β approach to 1 so that the effect of β on the viscosity can be disregarded. However, for smaller particle size, β is larger than l and dominated by the diameter of the particle. When the diameter of the particle decreases from 1 μm to 0.3 μm, β largely increases from 1.08 to 1.283. The result indicates that large β resulted from the smaller particle size largely influence the viscosity of suspension.

Given the Krieger and Dougherty model, Figure 4.3 shows the viscosities of suspension as a function of volume fraction of ceramic powder with different particle size. For lower volume percents, as expected, the suspensions are more fluid. However, the addition of more powder results in a more viscous suspension. For all suspensions in

CerSLA, a highly loaded but fluid suspension of ceramic powders in a photopolymerizable solution is required to produce a dense, homogeneous particle dispersed green body after solidification and sintered body after firing. In CerSLA, 3000 mPa-s as an upper limit to the viscosity for feasibility have been considered.[1] Figure 4.4 show the maximum solid loading of fused silica in the HDDA monomer as a function of particle size with an upper limit of viscosity of 3000 mPa-s. Due to the larger β of smaller particle size, as particle size changes from 0.3 μm to 40 μm, the maximum solid loading increased from 49 to 62.

The equations 4.6 and Figure 4.4 show the relationship between viscosity and volume fraction silica in the HDDA. The suspension viscosity is abruptly increased as the particle volume fraction approaches its maximum volume fraction or packing fraction ϕ_m. In order words, increasing the maximum volume fraction, ϕ_m, decreases the viscosity of a suspension at a given ϕ. Therefore, increasing the maximum volume fraction and decreasing the viscosity can be achieved by the Farris effect. As previously explained in chapter 3, this effect shows that the transition from monomodal to bimodal distribution increases maximum volume fraction, ϕ_m, thus exerting the most significant effect on the reduction of relative viscosity among the multimodal particle size distribution (PSD) in the suspension. This reduction in relative viscosity by the incorporation of fine particles is known as the Farris effect in which the PSD strongly affects the solid loading of suspension at the same relative viscosity.[9]

4.1.3 Writing Time (τ_{write}): Time to write a layer

For CerSLA, the recoat time is the same for all layers, while the time to write a layer, τ_{write} can be different for each layer due to the different exposure layer A_i. The time to write a layer can be calculated by the relationship between area (design factor) and the beam velocity[4]

$$\tau_{write} = \frac{A}{h_s v_L} \qquad 4.8$$

where τ_{write} is the writing time (sec), A the area of a layer (cm^2), h_s hatching spacing (cm), and V_L the beam velocity (cm/sec). Calculation of the writing time is more difficult than that of settling time because the writing time is largely affected by two factors: apparatus and material properties. Apparatus parameters considered in the current experiment are hatch spacing and power of laser influence scanning on the sliced layers. The equation derived by combination of Jacob's version of the Beer-Lambert law (equation 4.1) and laser velocity (equation 4.4) is:

$$\frac{1}{h_s v_L} = \frac{E}{P_L}$$

$$= \frac{1}{P_L} E_c \exp(\frac{\lambda}{D_p}) \qquad 4.9$$

where h_s is hatching spacing (cm), V_L the beam velocity (cm/sec), P_L laser power (mW), E_c the critical exposure for the resin to gel (mJ/cm^2), λ layer thickness (μm), and D_p the resin sensitivity, the distance at which the laser intensity is reduced by 1/e. From the addition of equations 4.9 into the addition of eq.4.8,

$$\tau_{write} = \frac{A}{h_s v_L} = \frac{A}{P_L} E_c \exp(\frac{\lambda}{D_p}) \qquad 4.10$$

From Equation 4.3, $D_p=\gamma d/\phi$, for the case of a scattering-dominated system

$$\tau_{write} = \frac{A}{h_s v_L} = \frac{A}{P_L} E_c \exp(\frac{\lambda \phi}{\gamma d}) \qquad 4.11$$

where A is an exposure surface area (cm^2), λ layer thickness (μm), P_L power of laser (mW), E_c the critical exposure for the resin to gel (mJ/cm^2), ϕ the concentration of solid, γ the term for the resin sensitivity related to the refractive index difference between ceramic powder and resin, and *d* is light scattering diameter. In equation 4.11, τ_{write} is dependent on the several factors. Factors affecting the time to write a layer can be divided by the three different main categories; Design factor (a surface area (A) and layer thickness (λ)), Apparatus factor (laser power P_L), and Material factor (volume fraction ceramic (ϕ), resin sensitivity (γ), and particle size (d)).

In order to take the shorter time to write a layer, several approaches can be applied. Two conditions in the design factor, a surface area (A) and layer thickness (λ), are related to τ_{write}. Given equation 4.11, an average surface area and layer thickness have a linear and an exponential relationship with τ_{write}, respectively. With the layers with small surface areas (A) as well as thicker layer thickness (λ), it takes shorter τ_{write}, and then decreasing τ_b for an object. Another approach is to adjust a laser power (P_L), the main variable in the apparatus factor capable of adjusting τ_{write}. When a large laser power is applied, a fast laser speed results in much less τ_{write}, thus leading to a shorter τ_b to build an object. The main material factor affecting τ_{write} is γ representing the resin sensitivity,

which is dependent on the difference of the refractive indices of the ceramic and medium. Therefore, the fast writing for a layer is achievable under the refractive index match between the ceramic and medium. For example, since fused silica powder has a small refractive index difference compared to that of the resin, γ increases and τ_{write} exponentially decreases, thus resulting in the shorter τ_b for several objects and increasing the production efficiency.

4.1.3. a. Writing Time in the Case of Building Several Objects

Given the equations 4.10, if n objects will be built at a time, the time to build a layer will be obtained from the recoating time and the writing time for the n surface areas of n objects. Therefore, with an average exposure layer A_{av}, the time to build a layer for several objects can be expressed in terms of the time for recoating and writing each layer τ_r and the time to write each layer τ_{write}

$$\tau_{b,\,a\ layer} = \tau_r + n\,\tau_{write}$$
$$= \tau_r + n\,\frac{A_{av}}{P_L}E_c\,\exp\left(\frac{\lambda}{D_p}\right) \qquad 4.12$$

where $\tau_{b,\,a\ layer}$ is the time to build a layer for several objects, τ_r is the time for recoating each layer, and τ_{write} is the time to write a layer. A_{av} is an average exposure surface area (cm^2), λ layer thickness (μm), P_L power of laser (mW), ϕ the concentration of solid, and D_p the resin sensitivity related to the refractive index difference between ceramic powder. There are several initial conditions. As already explained, the recoat time for all layers is the same. Conditions used to write a layer for several objects are the average surface area (16 cm^2), laser power (P_L=40mW), solid loading (ϕ=60 vol%), and

critical energy dose (E_c=10.19 mJ/cm^2), layer thickness (λ=100 μm) and resin sensitivity (D_p=803 microns) of fused silica dispersed suspension with 40 second recoating time.

Time to build a layer for several objects ($\tau_{b,\ a\ layer}$) in equation 4.12 is limited by the recoating time (τ_r) and the writing time ($\tau_{writing}$). Figure 4.5 shows the $\tau_{b,\ a\ layer}$ as a function of number of objects in tank, which is divided by two dominated regions: the recoating time and the writing time dominated region. When a layer for an object is fabricated under the previous conditions, it takes about 5 seconds for $\tau_{writing}$ and 45 seconds for $\tau_{b,\ a\ layer}$ so that $\tau_{b,\ a\ layer}$ is dominated by τ_r. However, increasing number of objects takes longer time to write a layer for several objects. When $\tau_{writing}$ takes as much as τ_r, the transition point from the recoating time to the writing time dominated region can be detected. For example, since $\tau_{writing}$ for 9 objects takes longer than τ_r, the transition point under the previous conditions is 8. The transition point means extra objects can be built within the same $\tau_{b,\ a\ layer}$, directly relating to the production yield. Consequently, delaying the transition point is the same as the increase of the production yield, which is achievable from the shorter $\tau_{writing}$. Therefore, the production yield increases by controlling the three different factors in order to take the shorter $\tau_{writing}$: Design factor (a surface area (A) and layer thickness (λ)), Apparatus factor (laser power P_L), Material factor (volume fraction ceramic (ϕ), and the resin sensitivity (γ), and particle size factor (particle size (d)). The time required to complete build of many layers in a more general case of D_p in which scattering and adsoption limit was presented in a recent paper.[10]

4.2 SEGREGATION MODEL: SEGREGATION PARAMETER (β) IN THE CASE OF UNIFORM PARTICLES

In the case of suspensions of coarser or denser particles, fast sedimentation of coarse particles lead to particle size segregation in which the population of larger or denser particles is greater near the bottom of the layer, as shown in Figure 4.6. The segregation in a layer is dependent on the two time constants: writing time and settling time. Figure 4.7 shows the effect of two time constants on the segregation in layers that segregation or no segregation in a layer occurs. If the writing time in equation 4.10 is longer than the settling time, coarse powder settles down, separating two main phases in a layer that is composed of a polymer and a silica powder dominated phase. The condition to suppress the segregation in a layer is that the time required to write a layer must be shorter than the time required for the suspended particle to settle a short distance.

The degree of segregation in a layer can be estimated based on the relationship of two time constants: the time to write a layer, $\tau_{writing}$, and the time how long it takes for particle to settle a layer thickness, $\tau_{settling}$. As shown in equation 4.10, $\tau_{writing}$ is dependent on the layer geometry, laser power, and resin photosensitivity. The photosensitivity varies with the type of ceramic and the particle volume fraction, depending on the adsorption parameters for the photoinitiator and scattering parameters for the powder, a function of the particle refractive index and particle size. To derive the segregation parameter (β) representing the degree of segregation, $\tau_{settling}$ is calculated by Stokes settling rate and time and is based on the particle size, density, monomer viscosity, and volume fraction. In order to calculate $\tau_{settling}$ using the Richardson-Zaki (R-Z) equation to, the uniform

particles with an average particle size in Stokesian hindered settling is applied.

4.2.1 Settling Rate and Time

The sizes of particles in suspension affect the stability of suspensions. Colloidal particles will remain suspended within fluid systems even after long times. Large particles will settle quickly when suspensions are at rest and flow velocities are low. The fast sedimentation rate of large particles is directly related to the segregation in a layer. In previous CerSLA work, since submicron sized powders are used, the particles remain in suspension without settling for periods longer than the time required building a layer. But refractory-grade powders have coarse particles to impart creep resistance at high temperatures, inducing segregation in a layer resulting from the fast sediment of coarse powder during building a layer in CerSLA. Thus, settling time, a time constant related to the segregation, is calculated in order to prevent segregation in a layer as considering the time how long it take for particle to settle a layer thickness.

Any discussion of silica powder settling must start with a consideration of simple systems, since the downward migration of silica through photo-curable monomer occurs. Hence, the steady settling rate on the various particle sizes of silica powder as a given particle in isolation in fluid is calculated by Stokes' law[11], with

$$v_{stokes} = \frac{1}{18}\frac{(\rho_{ceramic} - \rho_{liquid})gd^2}{\eta} \qquad 4.13$$

where ρ_c and ρ_l are the density of the solid ceramic particle and the monomer liquid, g is the gravitational acceleration, d is diameter of ceramic powder, and η is the fluid viscosity, respectively. Inspection of equation 4.13 shows that the settling rate of a

single particle is much larger by an increase in the particle size (proportional to d^2), and retarded by an increase in the liquid viscosity.

When increasing solid loading in a suspension, the rate of sedimentation is less than the velocity given by the Stokes law. Stoke's law does not apply when circumstances cause settling to be 'hindered'. One example of this is when too many particles are in suspension, and particles crowd one another. Another example is when coarse particles settle and the turbulence in their wakes drags along other particles. In the hindered region with more concentrated solid, hindered settling occur and reduce the settling velocity of a particle, and longer residence time from the interaction between a particle and its neighboring particles.[12]

Large particle sizes[1] of fused silica used in this work were governed by the hydrodynamic interaction forces and gravitational force. The settling rate of large particle sizes is calculated by the Richardson-Zaki (R-Z) equation. This equation is widely accepted to correlate the superficial fluidizing velocity ν and the particle volume fraction ϕ of fluidized beds and suspensions of non-agglomerated particles[13]

$$\begin{aligned} v &= v_{stokes}(1-\phi)^n \\ &= \frac{1}{18}\frac{(\rho_p-\rho_f)gd^2}{\eta}(1-\phi)^n \end{aligned} \qquad 4.14$$

Where ρ_c and ρ_l are the density of the solid ceramic particle and the monomer liquid, g is the gravitational acceleration, d is diameter of ceramic powder, η is the fluid viscosity, ϕ is the concentration of solid, respectively. The exponent n is an empirical

[1] At large size, turbulence sets in and Stokes law (a laminar flow mode) does not work. In particular sedimentation, Stokes law is for the case of low Reynolds number, Re= (diameter)(fluid density)(stokes velocity)/(fluid viscosity). Given the values of coarse particles, the particle Reynolds number is $5.18 * 10^{-4}$.

parameter whose value has been a discrepancy. For example, Richardson and Zaki reported n = 4.65 in the small particle Reynolds number (Re_t) regime, while n decreased as Re_t increased. Given the Richardson-Zaki (R-Z) equation 4.14, the settling rate of silica with different particle sizes in the suspension as a function of volume faction silica is calculated, as shown in Figure 4.8. Note that the exponent of 4.65 was applied due to the small particle Reynolds number. In the dilute region, coarser silica powders by rapid settling rate quickly settle. However, in the concentrated region, when the amount of silica increased from 40 to 60 volume fraction silica in the HDDA, the settling rate for silica powders with diameter of 60 microns decreased from 2.2 x 10^{-5} m/sec to 3.3 x 10^{-6} m/sec.

Given the settling rate, two regions relating to the settling are divided by Micro-sedimentation and Macro-sedimentation, as shown in Figure 4.9. Micro-sedimentation shows the settling time for the length scale with micrometer unit of a layer thickness (10 μm) and Macro-sedimentation settling time is considered for the centimeter scale on the tank scale (10 cm).

4.2.1. a. Settling Time in Micro-Sedimentation

Figure 4.10 show the settling time for particles to settle a layer thickness of 100 microns. With on the rate represented by the Stokes velocity multiplied by a term of function of concentration, the settling time is calculated, with

$$\tau_{settle} = \frac{\lambda}{\nu} = \frac{\lambda}{v_{stokes}(1-\phi)^n} \qquad 4.15$$

where λ is a layer thickness, ν is the settling rate of fused silica calculated by the

Richardson-Zaki (R-Z) equation, and ϕ is the concentration of solid, respectively. When the settling time of particles in a layer thickness of 100 microns is calculated as a function of silica particle size at the 60 volume fraction silica added into suspension, Figure 4.10 shows that it takes 30.1 seconds for silica powders with particle size of 60 microns and 76.3 seconds for silica powders with particle size of 40 micron.

4.2.1. b. Settling Time in Macro-Sedimentation

Given equation 4.15, the settling time in macro-sedimentation is calculated for long range settling of particles. Figure 4.11 shows the settling time in Macro-sedimentation, which is based on the centimeter length scale of a full tank size (10 cm), as a function of volume fraction of silica with different particle sizes. At the suspension including 60 volume fraction of silica powder, it takes 8.3 or 21.2 hour for silica powders with diameter of 60 microns or 40 microns for sedimented sludge to form in bottom of tank.

4.2.2 Segregation Parameter (β) for Degree of Segregation

To estimate the degree of segregation parameter, we have calculated derived the segregation parameter (β). In order to suppress the segregation in a layer, a prerequisite was established such that the time required to write a layer must be shorter than the time required for the suspended particle to settle a short distance. Given the relation of two time constants; the writing time and the settling time, a parameter (β) representing the severe or little segregation in a layer is

$$\beta = \frac{\tau_{write}}{\tau_{settle}}$$

$$\beta = 1 \quad \text{when} \quad \tau_{settle} = \tau_{write} \qquad 4.16$$

where τ_{write} is time to write a layer and $\tau_{settling}$ is time to settle particles. For preventing segregation in a layer, the segregation parameter, β in Equation 4.16 should be less than 1 to prevent segregation in a layer. For example, when writing time takes less than the settling time, β is smaller than 1 or approaches to 0 and generates less or no segregation in a layer. On the other hand, when β is larger than 1, since the writing time takes longer than the settling time, particle size segregation shown in Figure 4.6 will be detected such that full segregation with two completely separated regions, a ceramic and a polymer part, in a layer exist. Therefore, since small β represents short writing time or long settling time, small β is required for no segregation in a layer.

Given the prerequisite, segregation in a layer will be suppressed when writing time and settling time are equal. According to equation 4.16, the segregation parameter (β) can be derived from the comparison between the writing time in equation 4.10 and the settling time in equation 4.15. The segregation parameter (β) is expressed by

$$\beta = \frac{\tau_{write}}{\tau_{settle}} = \frac{A_{av}}{\lambda}\frac{1}{P_L} v_{stokes}(1-\phi)^n E_c \exp\left(\frac{\lambda\phi}{\gamma d}\right) \qquad 4.17$$

where A_{av} is the average surface area (cm^2), λ layer thickness (μm), P_L power of

laser (mW), ν_{stokes} the stoke's settling rate, ϕ the concentration of solid, γ the term for the resin sensitivity related to the refractive index difference between ceramic powder and resin, and *d* is light scattering diameter. In equation 4.17, the segregation parameter (β) representing the degree of segregation is dependent on the several factors. Among the factors affecting the degree of segregation, the relationship between β and layer thickness (λ) are characterized in detail using two regimes of layer thickness. In addition, for the parametric study to define the criteria for the region of no segregation, there are several initial conditions; layer thickness (λ=250 microns), area (A=16 cm^2), and laser power (P_L=40 mW). For low degree of segregation at β=0.1, the dependence of segregation on several parameters is demonstrated by the relationship between the following factors governing segregation: surface area A vs. layer thickness λ (the design factor) and laser power P (the apparatus factor) vs. particle size (d_{90}).

4.2.2. a. Segregation Parameter (β) vs. Layer Thickness (λ)

Equation 4.17 shows the dependence of the degree of segregation on several factors. Among the factors related to the segregation in a layer, the segregation parameter (β) and the layer thickness in equation 4.17 are able to express two different regimes, the linear or exponential regime. Figure 4.12 shows the connection between β and the layer thickness, where linear or exponential association is dependent on the size difference between layer thickness and resin sensitivity. For considering the β, the resin sensitivity (D_p) is necessary to compare the ratio of layer thickness to resin sensitivity in the exponential term. The resin sensitivity of 60 volume percent of fused silica in the

hexanediol diacrylate monomer (HDDA) with 2 wt% photoinitiator is 803 microns, which is calculated from the relationship between cure depth and energy dose in Beer-Lambert equation. Given the relationship between layer thickness and resin sensitivity, where two regimes according to the size difference between layer thickness and resin sensitivity are divided to thinner or thicker layer thickness. The degree of segregation depending on the layer thickness can be simplified by;

$$\beta \sim \frac{1}{\lambda} \qquad (\lambda << D_P) \qquad (4.18.1)$$

$$\beta \sim exp(\frac{\lambda}{D_P}) \qquad (\lambda \geq D_P) \qquad (4.18.2)$$

where β is the segregation parameter, λ layer thickness, and D_p is the resin sensitivity, the distance at which the laser intensity is reduced by 1/e. Given equation 4.18.1 for the thinner layer thickness, the degree of segregation is limited by inverse proportion to the layer thickness since resin sensitivity of 803 microns is much larger than the layer thickness of 100 microns. Therefore, β linearly decreases according to the increase of the layer thickness. On the other hand, for the thicker layer thickness shown in equation 4.18.2, when the layer thickness is larger than the resin sensitivity of 803 microns, βexponentially increases according to the layer thickness. Since the thickness of layers built by ceramic stereolithography is less than 200 microns, the linear relationship between the degree of segregation and layer thickness will be mainly considered.

In chapter 3, Figures 3.11 (a) and (b) showed severe segregation and much less segregation in sequential layers according to the conditions, respectively. The criteria for no segregation should be necessary for a thorough understanding the segregation in a

layer and solve the segregation problem. In order to suppress the segregation in a layer, we already established the prerequisite that the time required to write a layer must be shorter than the time required for the suspended particle to settle a short distance. Given the prerequisite, the segregation parameter (β) can be expressed by

$$\beta = \frac{\tau_{write}}{\tau_{settle}} = \frac{A}{\lambda}\frac{1}{P_L} v_{stokes}(1-\phi)^n E_c \exp(\frac{\lambda\phi}{\gamma d}) \qquad 4.19$$

where β is the segregation parameter, A surface area (cm^2), λ layer thickness (μm), P_L power of laser (mW), v_{stokes} the stoke's settling rate, ϕ the concentration of solid, γ the term for the resin sensitivity related to the refractive index difference between ceramic powder and resin, and *d* is light scattering diameter. Equation 4.19 represents the degree of segregation, and is used to define the criteria, thus revealing the region of segregation or no segregation. Additionally, equation 4.19 represents the degree of segregation from the ratio of writing time to settling time. β less than 1 or approaching 0 induces less or no segregation, while β larger than 1 causes full segregation with two completely separated regions, a ceramic and a polymer part, in a layer.

4.2.2. b. Surface Area (A) vs. Layer Thickness (λ)

The surface area (A), as a design factor, was compared with layer thickness (λ) to determine the conditions required to write a layer without segregation. By looking at the equation for the degree of segregation parameter, the relationship between area and layer thickness is shown below:

$$A_s = \frac{\beta P_L}{E_c \exp(\frac{\lambda}{D_p})} \frac{1}{v_{stokes}(1-\phi)^n} \lambda$$

$$\approx \frac{\beta P_L}{E_c e} \frac{1}{v_{stokes}(1-\phi)^n} \lambda \quad (\lambda << D_p) \qquad 4.20$$

where A is the surface area of a largest layer among the several layers, and λ is the layer thickness. There are several initial conditions; laser power (P_L=40mW), solid loading (ϕ=60 vol%), and critical energy dose (E_c=10.19 mJ/cm^2) and resin sensitivity (D_p=803 microns) of fused silica dispersed suspension. Initial conditions are applied to Equation 4.20 in order to predict the region where segregation occurs or the region of no segregation. Figure 4.13 shows the relationship between surface area and layer thickness, and also the effect of layer thickness on segregation. When layers with the maximum area of 40 cm^2 are built from a suspension including silica powder with uniform particle size of 40 microns, layers with thickness larger than 200 microns are required to build a 3D complex part without segregation.

Figure 4.14 shows the influence of layer thickness and particle size on the surface area of a layer. Given layer thickness, the figure helps to find a proper large area for the 3D complex part without segregation. For example, when a layer is fabricated under the following conditions, layer thickness of 200 microns and silica powder with particle size of 60 microns, ceramic stereolithography can build layers with the surface area less than 18.4 cm^2 without segregation. However, if five parts will be built at a time, the segregation in a layer is resulted from the large surface area of 92 cm^2. This segregation problem can be fixed based on the modification of particle size distribution shown in

Figure 4.14. Under suspension including particle size of 20 microns, ceramic stereolithography can build a layer with the surface area less than 165.8 cm^2 without segregation. Therefore, using a powder with uniform particle size of 20 microns can write a total surface area of 92 cm^2 for five parts at a time or a larger surface area of 92 cm^2 for a part without segregation.

4.2.2. c. Laser Power (P_L) vs. Particle Size (d_{90})

In the case of the apparatus parameter, since the scanning speed on the sliced layers is proportional to the power of laser, segregation in a layer is largely influenced by the laser power. Given equation 4.19, the relationship between laser powder and particle size is obtained by:

$$P_L = AE_c \exp\left(\frac{\lambda\phi}{\gamma d}\right)\frac{1}{\lambda} v_{stokes}(1-\phi)^n \qquad 4.21$$

where P_L is a laser power, λ is the layer thickness, and $\nu(\phi)$ is settling velocity calculated from the silica powder with uniform particle size. Several initial conditions, solid loading (ϕ=60 vol%), surface area (A=16 cm^2), and critical energy dose (E_c=10.19 mJ/cm^2) and resin sensitivity (D_p=803 microns) of fused silica dispersed suspension, were used to build layers. Values of laser powder required to prevent segregation in a layer are calculated from Equation 4.21 and largely varies according to particle size, where laser powder ranges from 10 to 150 mW for a layer thickness of 100 microns. Larger particles can be used in the resin without segregation if laser power is increased. As shown in Figure 4.15, the region of no segregation is detected in the upper region above plot. No segregation is originated from the shorter writing time than the settling

time, where the shorter writing time is resulted from the high laser speed induced by the high laser power. On the other hand, the area below plot is the region where segregation occurs and it should be avoided. When 3D complex parts are prepared under the following conditions; a layer thickness of 100 micron and a suspension including fused silica powder with uniform particle size of 40 microns, laser power larger than 26.5 mW is required to prevent segregation.

However, since high laser power usage is limited due to its expensive price, it would be much better to consider the dependence of laser power on the layer thickness in order to find the region of no segregation under the current laser power (40 mW) and particle size. Figure 4.16 shows the effect of the laser power and PSD with different layer thickness, 50 to 250 microns. The layer thickness is directly related to the settling time so that changing layer thickness is a strategy to prevent segregation in a layer. For example, at the current condition (laser power of 40 mW), segregation is expected for 100 microns layers if particles are larger than 48 microns. The segregation can be prevented by modifying layer thickness from 100 to 150 micron, thus able to use fused silica powder with uniform particle size of 48 microns without any segregation. In addition, since the degree of segregation depends on the relationship between layer thickness and laser power, laser powers required for no segregation can be calculated according to the different layer thickness. In the particle dispersed suspension with uniform particle size of 40 microns, laser powers larger than 89 mW or 60 mW is required to build layers with layer thicknesses of 150 microns or 250 microns, respectively.

4.3 CONCLUSTION

Ceramic stereolithography (CerSLA) is a repeated layered manufacturing process where thin liquid layers of powder in monomer are solidified by photopolymerization with a UV laser, thereby "writing" the design for each slice. Total build time τ_b to produce an object is the same as the sum of the time for recoating τ_r and the time to write each layer τ_{write}. Since the recoat time is the same as 40 seconds for all layers, τ_b is mainly limited by τ_{write}. In order to take the shorter τ_b, τ_{write} can be modified by the several factors in the three different main categories; Design factor (a surface area (A) and layer thickness (λ)), Apparatus factor (laser power P_L), and Material factor (volume fraction ceramic (ϕ), resin sensitivity (γ), and particle size (d)). With the layers with small surface areas (A), thicker layer thickness (λ), and high laser power, it takes shorter τ_{write}, and then decreasing τ_b for an object. Moreover, a small refractive index difference between the ceramic and medium increases γ, thus reducing the τ_b and increasing the production efficiency.

In the case of suspensions of coarser or denser particles, fast sedimentation of coarse particles lead to particle size segregation in which the population of larger or denser particles is greater near the bottom of the layer. For the optimization of parameter used in CerSLA to suppress segregation in a layer, the segregation parameter (β) is derived from the ratio of the writing time, τ_{write} to settling time, $\tau_{settling}$. β larger than 1 indicates severe segregation, while β smaller than 1 represents little or no segregation in a layer. The small β for little segregation is generated when τ_{write} should be shorter than

$\tau_{settling}$. For low degree of segregation at β=0.1, the dependence of segregation is demonstrated by the relationship among particle size (d_{90}), laser power P (the apparatus factor), and layer thickness λ (the design factor). In the particle dispersed suspension with uniform particle size of 40 microns, laser powers larger than 89 mW or 60 mW is required to build layers with layer thicknesses of 150 microns or 250 microns, respectively.

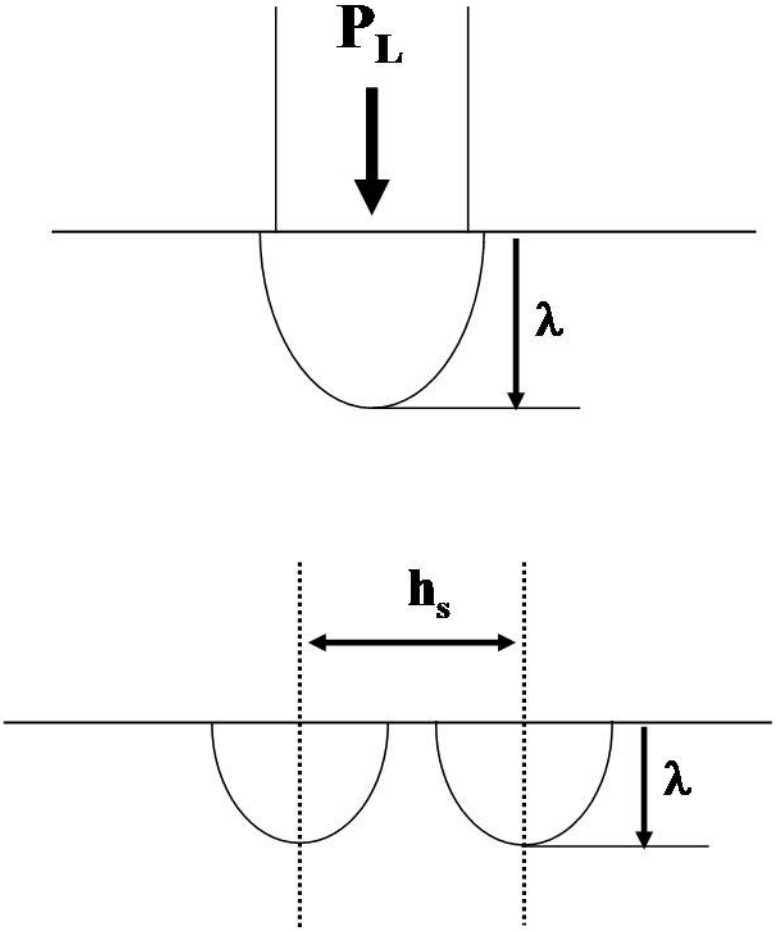

Figure 4. 1 Apparatus parameters, Laser power (P_L), Layer thickness (λ), and hatch space (h_s), related to the time to write a layer.

	β
1 μm	1.080
3 μm	1.026
7 μm	1.011
12 μm	1.006
26 μm	1.003
40 μm	1.001

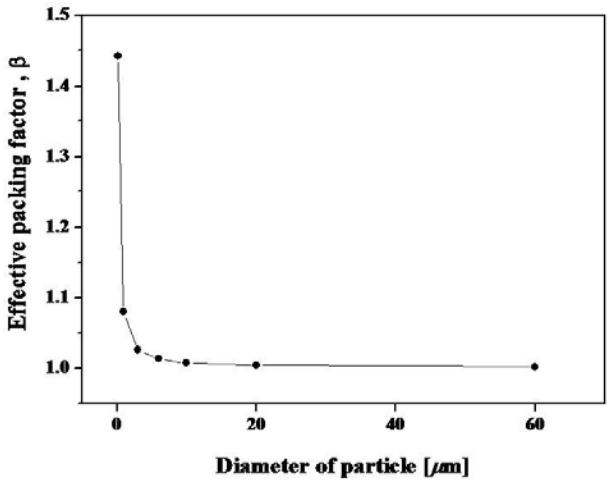

Figure 4. 2 Effective packing factor (β) as a function of particle size of fused silica.

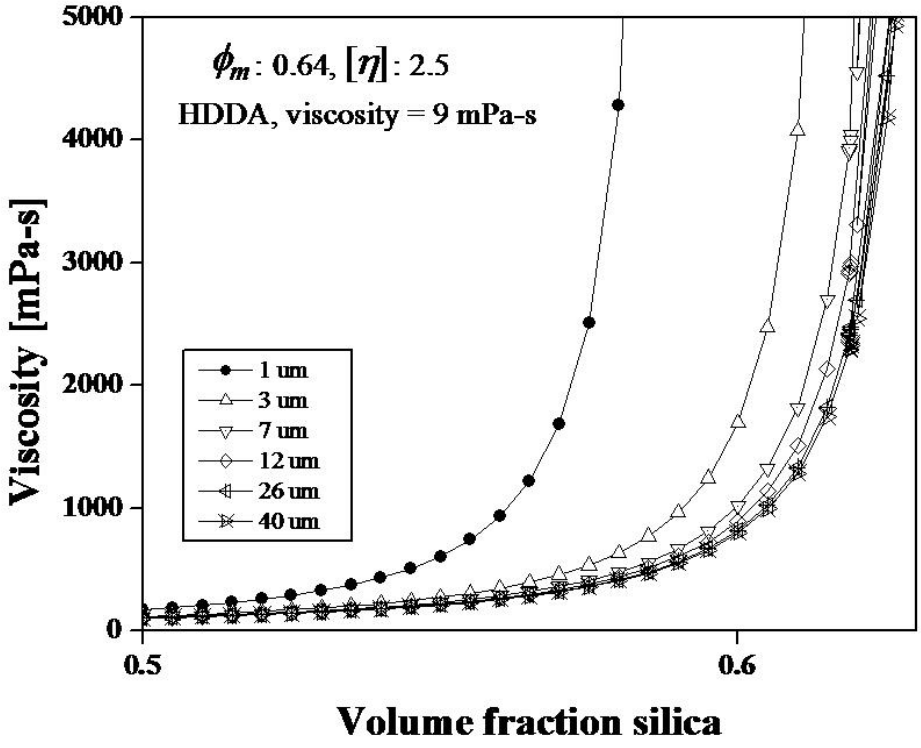

Figure 4. 3 Model calibration of the viscosity versus volume faction silica dispersed in the HDDA ultraviolet curable solution. Silica powder between 1 and 40 μm are shown. The maximum loading amount of silica is determined by the Krieger-Dougherty model.

	ϕ_{max} ($\eta \approx 3000$ mPa-S)
1 μm	58.8
3 μm	61.9
7 μm	62.8
12 μm	63.1
26 μm	63.3
40 μm	63.4

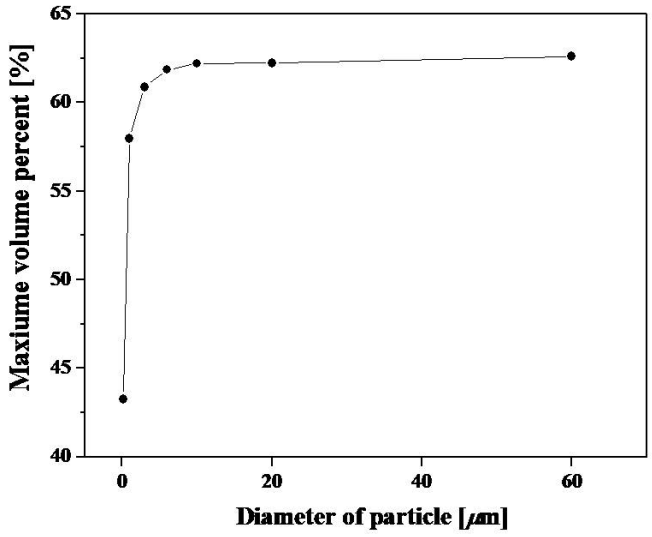

Figure 4. 4 Maximum solid loading as a function of particle size at an upper limit to the viscosity of 3000 mPa-s for feasibility of CerSLA .

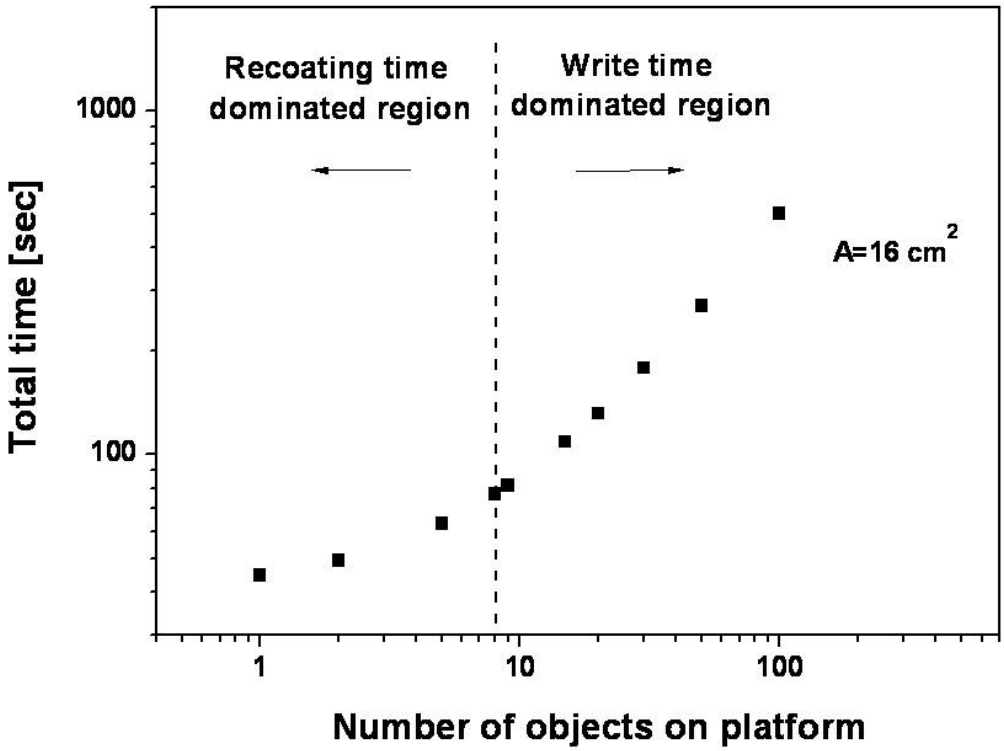

Figure 4. 5 Time to build a layer for several objects as a function of number of objects on the platform, for the case when each object has an area of 16 cm^2 and recoat time is 40 seconds.

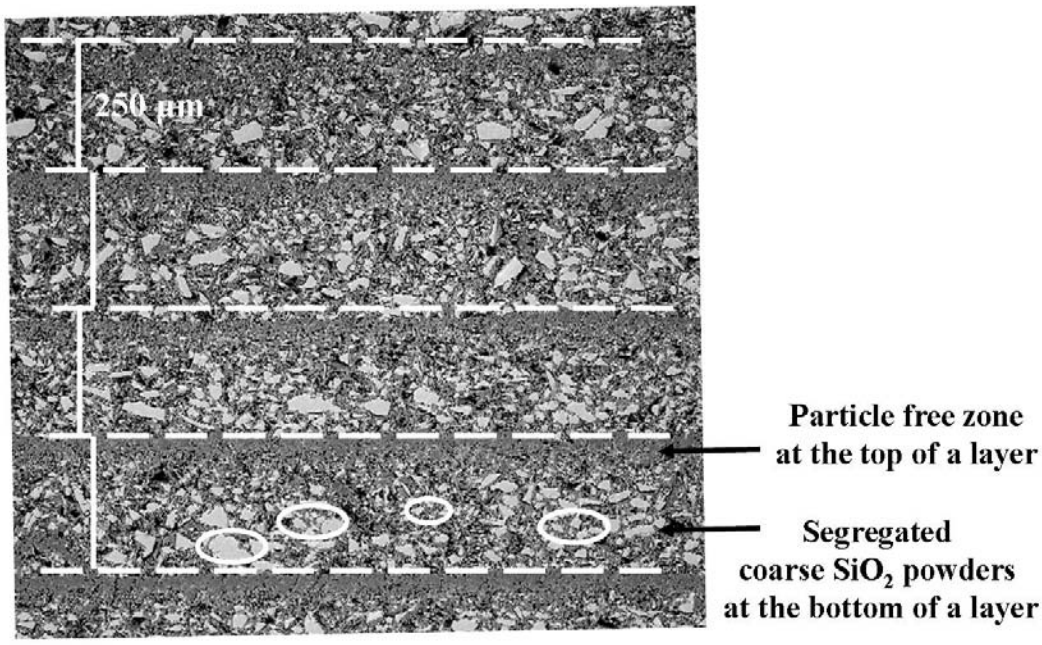

Figure 4. 6. Particle size segregation in a layer due to the fast sedimentation of coarse powder. Suspensions of coarser or denser particles can undergo differential sedimentation, leading to particle size segregation in which the population of larger or denser particles is greater near the bottom.

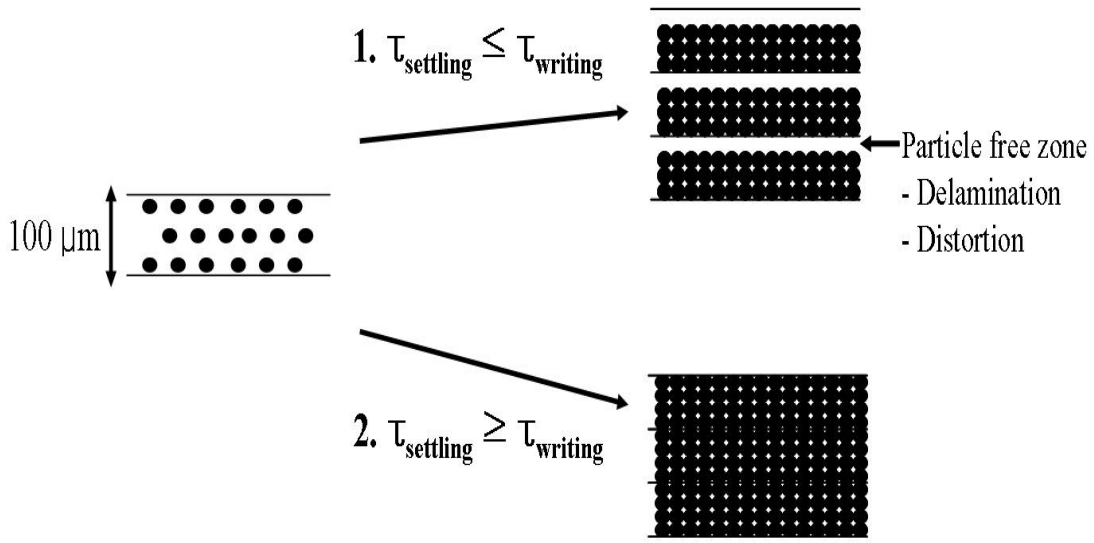

Figure 4. 7 Schematic diagram representing segregation or no segregation in a layer. In order to prevent segregation in a layer, the time required to write a layer must be shorter than the time required for the suspended particle to settle a short distance.

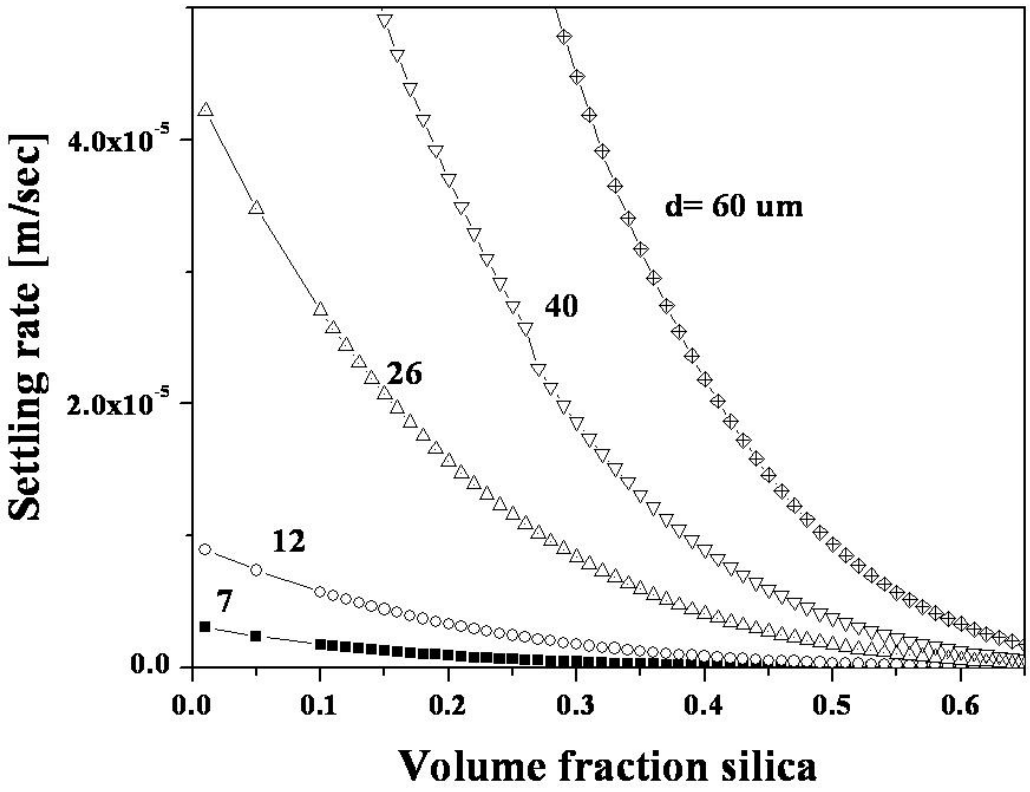

Figure 4. 8 Settling rate as a function of volume fraction silica.

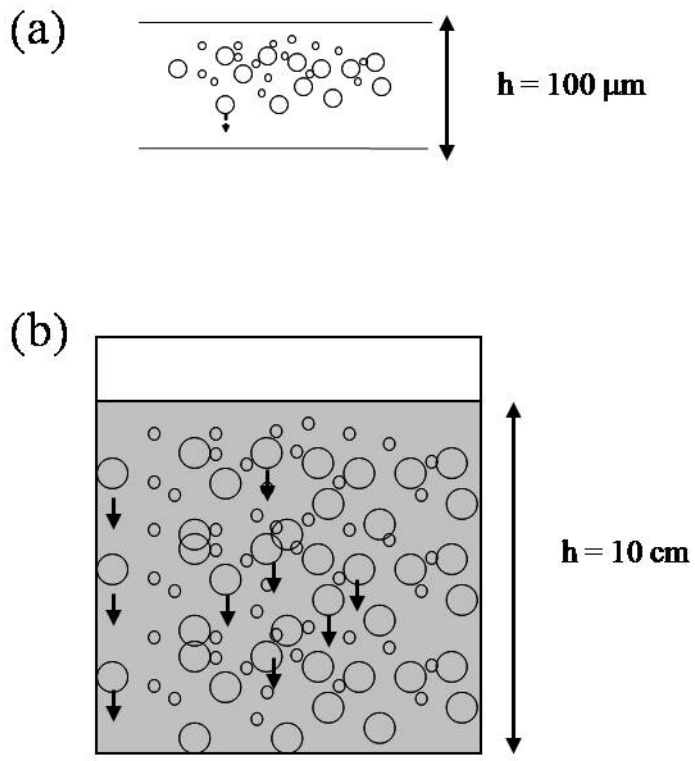

Figure 4. 9 (a) Micro-sedimentation with length scale of the layer thickness of 100 microns and (b) Macro-sedimentation with length scale of the height of tank of 10 centimeter.

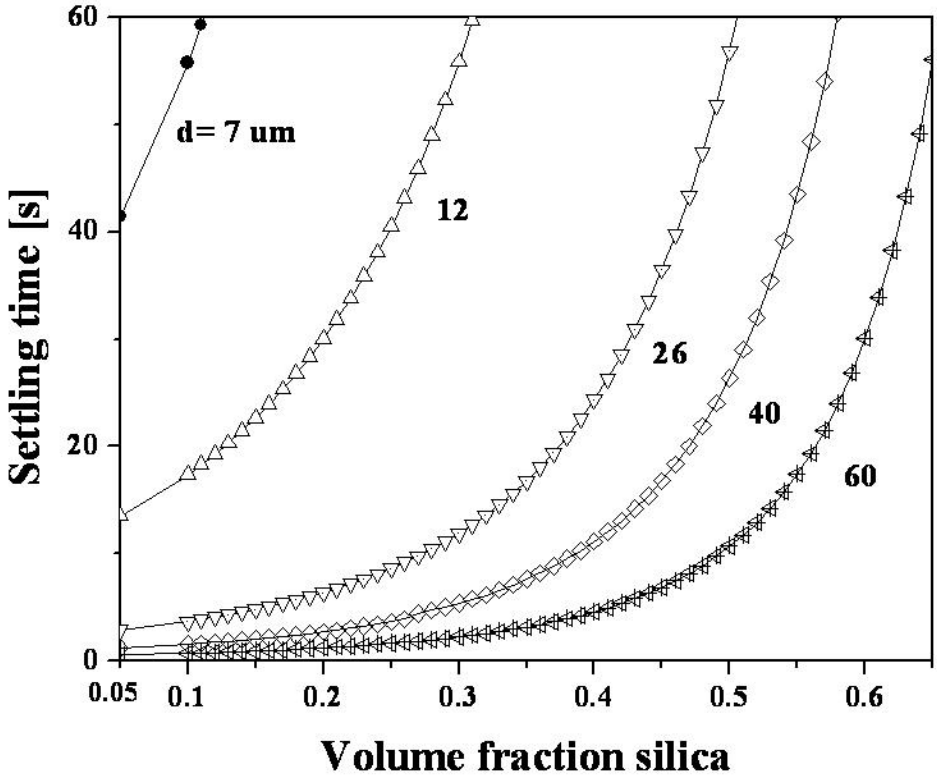

Figure 4. 10 Settling time for a layer thickness of 100 μm, as a function of volume fraction of silica with different particle size

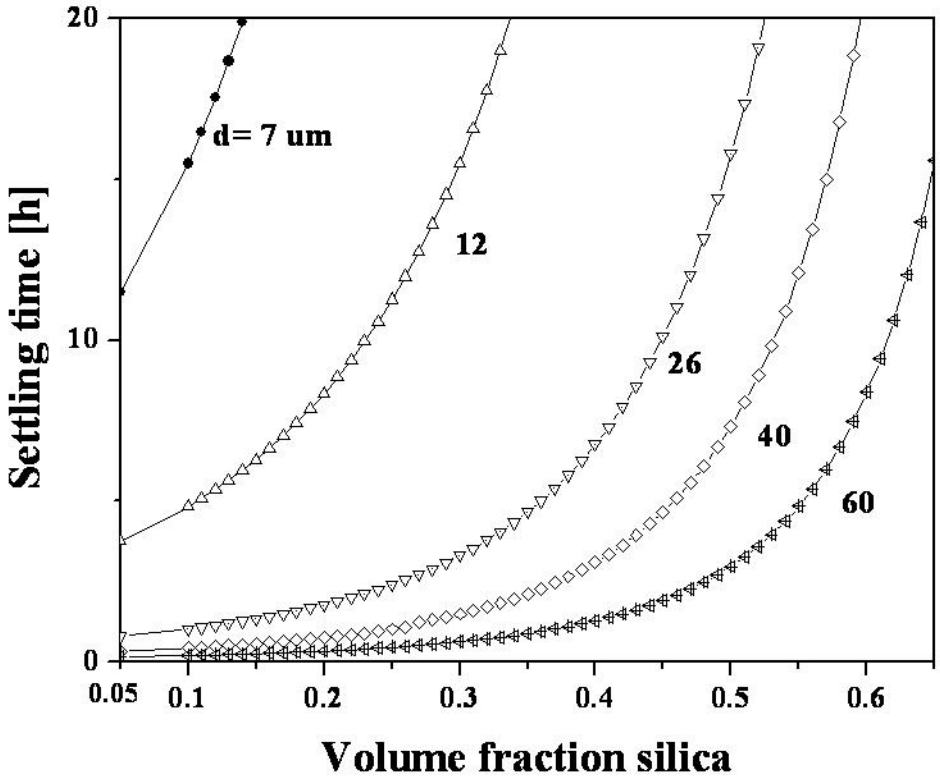

Figure 4. 11 Settling time in Macro-sedimentation on the length scale of a full tank (10 cm) for long range settling of particles, as a function of volume fraction of silica with different particle size

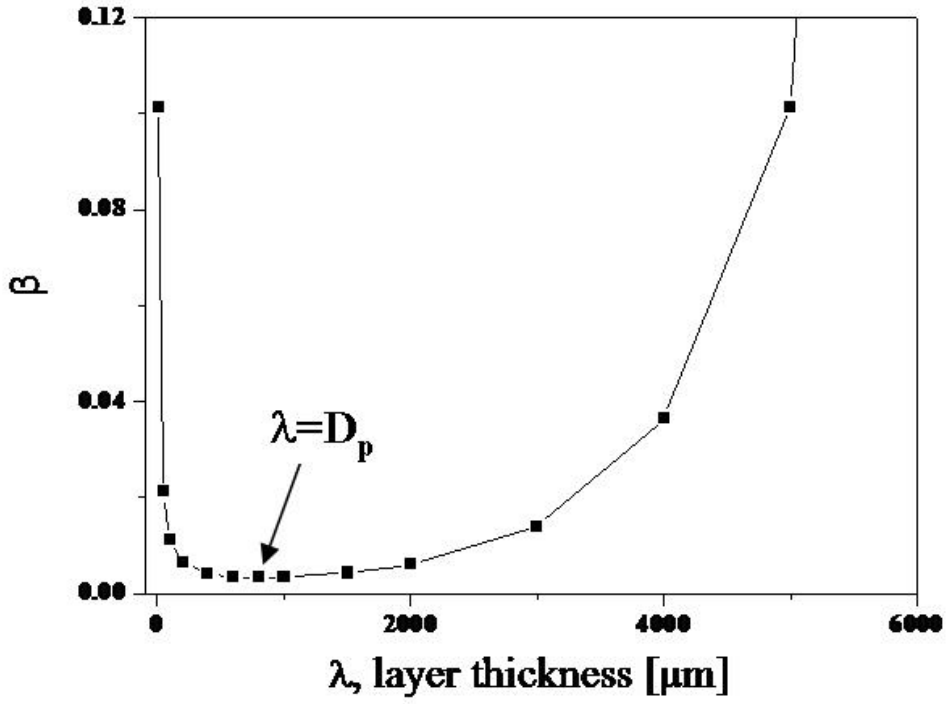

Figure 4. 12 Degree of segregation as a function of layer thickness. The degree of segregation and the layer thickness show two different regimes; the linear regime in the thinner layer thickness ($\lambda \ll D_p$) and the exponential regime in the thicker layer thickness ($\lambda \geq D_p$).

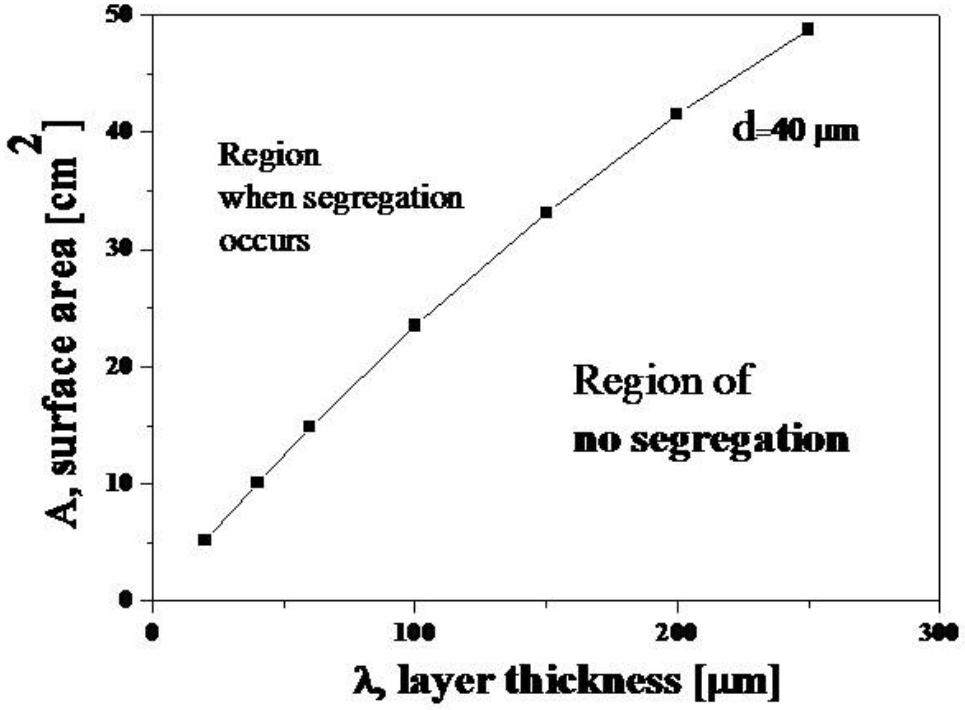

Figure 4. 13 Regions representing segregation and no segregation in a layer at the degree of segregation parameter (β=0.1). The occurrence of segregation is dependent on the design factors (surface area, A and layer thickness, λ).

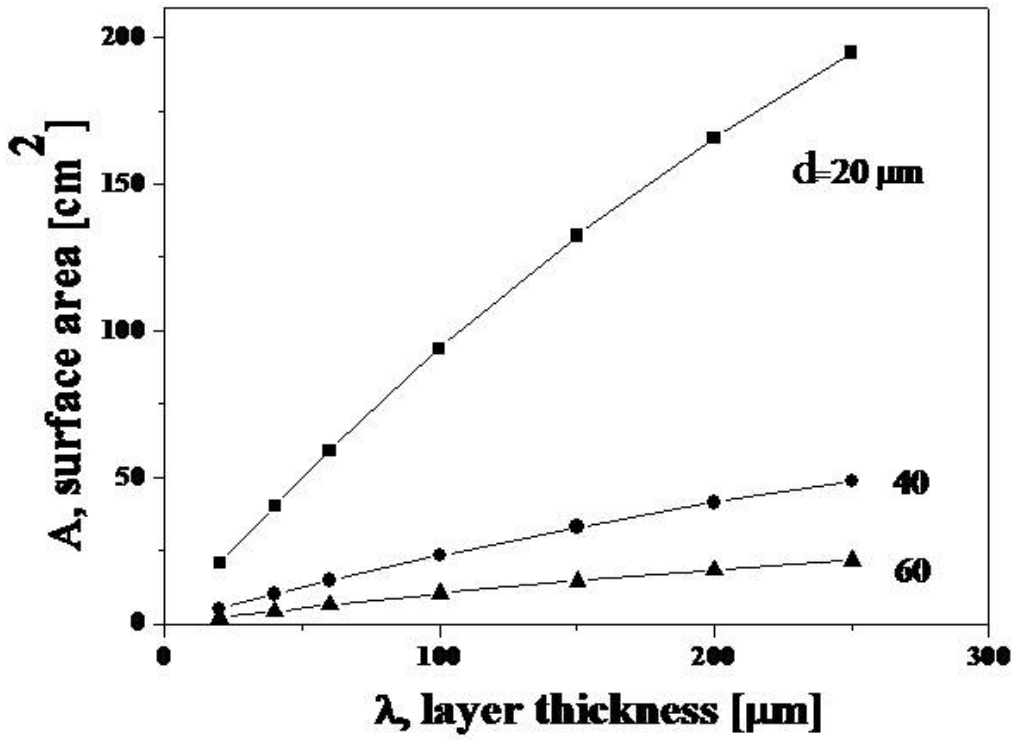

Figure 4. 14 Effect of design factor (area, A and layer thickness, λ) on the segregation in a layer at the degree of segregation parameter (β=0.1). Three different parameters (area vs. layer thickness vs. particle size) are used to determine conditions escaping segregation in a layer.

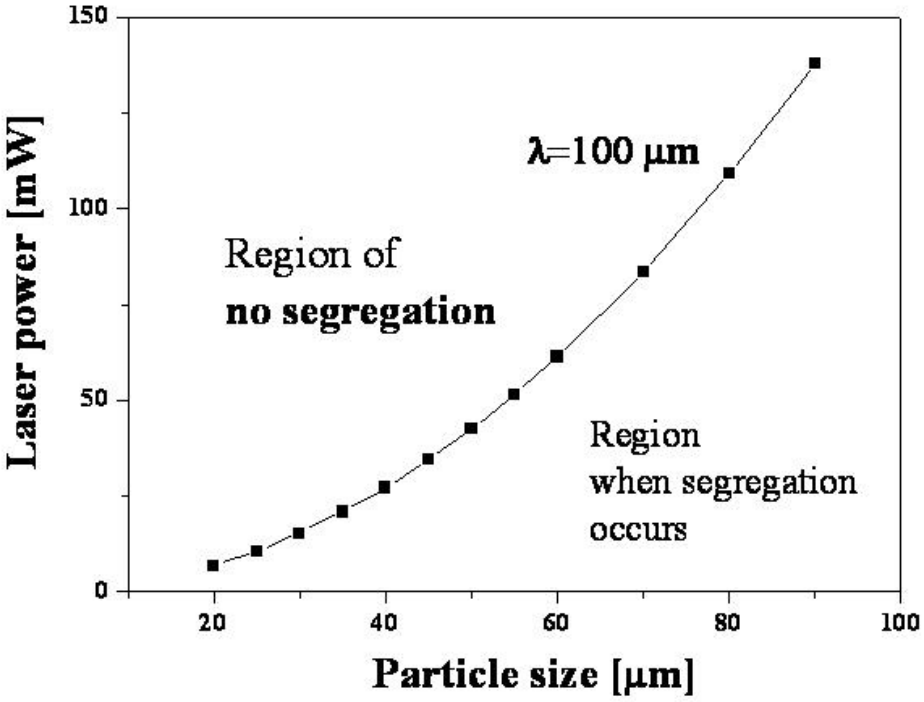

Figure 4. 15 Regions representing segregation and no segregation in a layer at the degree of segregation parameter (β=0.1). The occurrence of segregation is dependent on the Apparatus factor (laser powder, P_L).

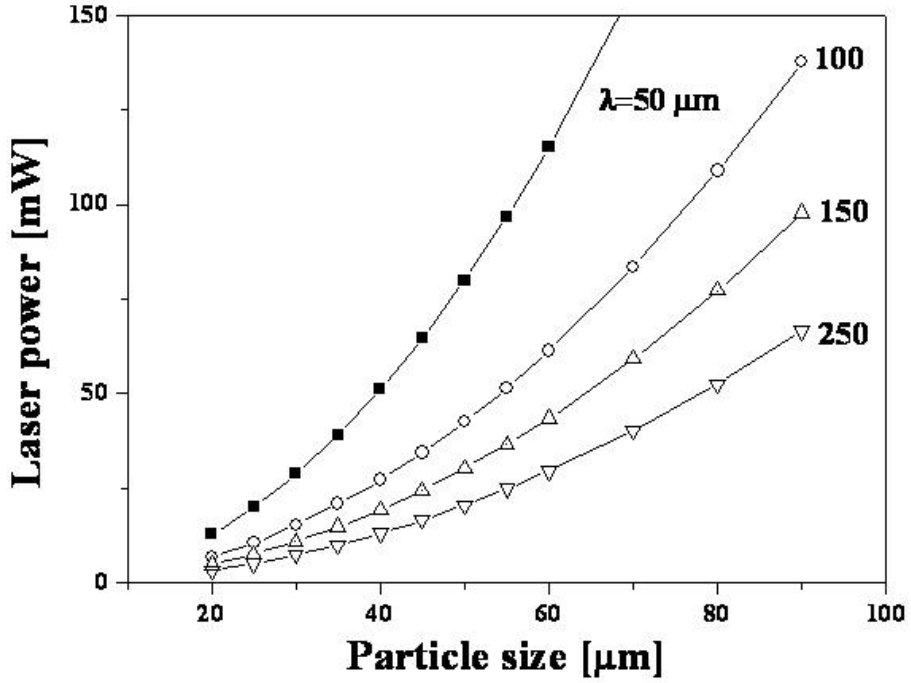

Figure 4. 16 Effect of apparatus factor (laser power, P) on the segregation in a layer at the degree of segregation parameter (β=0.1). Three different parameters (laser power vs. particle size vs. layer thickness) are used to determine conditions escaping segregation in a layer. Larger particles can be used in the resin without segregation if laser power is increased.

Reference

1. M.L. Griffith, "Stereolithography of Ceramics", Ph.D. Thesis, University of Michigan, 1995
2. K.C. Wu, K.F. Seefeldt, M.J. Solomon, and J.W. Halloran, "Prediction of Ceramic Stereolithography resin sensitivity from theory and measurement of diffusive photo transport", J. Appl. Phys. 98, 024902 (2005)
3. M.L. Griffith and J.W. Halloran, "Scattering of Ultraviolet radiation in turbid suspensions", J. Appl. Phys. 81, 2538 (1997)
4. P.F. Jacobs, "Rapid Prototyping & Manufacturing – Fundamentals of Stereolithography", 397-423, SME, La Crescenta, California, 1992
5. G.A. Brady and J.W. Halloran, "Solid freeform fabrication of ceramics via stereolithography", Naval Research Reviews, 3, 39-43, 1998
6. C. M. Lynn, D. W. Rosen, "Usage of accuracy models in stereolithography process planning", *Rapid prototyping journal*, *6* [2], 77, 2000.
7. I.M. Krieger and T.J. Dougherty, "A Mechanism for Non-Newtonian Flow in Suspensions of Rigid Spheres", Trans. Soc. Rheol., 3, 137-52 (1959)
8. T.M. Chu and J.W. Halloran, "High-Temperature Flow Behavior of Ceramic Suspension", J. Am. Ceram. Soc., 83[9], 2189-95 (2000)
9. Farris, R. J. Prediction of the viscosity of multimodal suspensions from unimodal viscosity data. *Trans. Soc. Rheol.* 12, 281-301 (1968)
10. J.W. Halloran, C-J Bae, C. Torres-Garibay, V. Tomeckova, S. Das, and W. Baker, "Manufacture of complex ceramics by photopolymerization", Proceedings of 2nd international congress on ceramics, June 29-July 4 2008, Verona, Italy

11. T.C. Patton, “Paint Flow and Pigment Dispersion”, 530-545, A wiley-interscience pub, Brick Town, New Jersey, 1979

12. J. Happel, “Viscous Flow in Multiparticle Systems: Slow Motion of Fluids Relative to Beds of Spherical Particles”, A.I.Ch.E. Journal, 4 [2] 197-201 (1958)

13. J. F. Richardson & W. N. Zaki, “Sedimentation and fluidization: Part I,” *Trans. Inst. Chem. Engrs.,* 32, 35-53 (1954).

CHAPTER 5

INTEGRALLY CORED CERAMIC MOLD (ICCM) FABRICATED BY CERAMIC STEREOLITHOGRAPHY (CerSLA):

Ceramic casting molds for superalloy airfoils have been produced by lost wax processes, which use ceramic cores, wax patterns, and ceramic shell molds. Due to the several steps involved in the lost wax process, costly tooling is required to produce mold dies for complex cores and wax patterns by injection molding. The cost and production delays associated with this tooling are disadvantageous for prototypes and smaller production runs.

This chapter covers ceramic stereolithography (CerSLA) as an alternative method to replace lost wax processes, for small production runs or designs too complex for conventional cores and patterns. Using layer-by-layer growth enabled by CerSLA, it is possible to eliminate the pattern and produce a one-piece mold integrated with the core, or an Integrally Cored Ceramic Investment Casting Mold (ICCM).

5.1 INTRODUCTION

Investment casting (IC), where refractory shell molds are embedded in wax patterns, is a widely used technique for modern metal casting, and provides an economical means of mass producing shaped metal parts containing complex features. Hollow cored super alloy airfoils are examples of complex IC parts. These complex structures of airfoils are designed to conduct cooling air through one or more passageways in the turbine. Demands for these more complex internal passageways are related to greater cooling efficiency of airfoils in turbines.[1]

For these complex airfoils, a lost wax process that involves several processing steps is used to make ceramic molds as shown in Figure 5. 1.[2] Hollow cavities in cast airfoil are produced using preformed ceramic cores located within the injection mold. The pieces of the complex ceramic core are formed separately using injection molding, assembled together. Wax is injected into the mold and over cores to make a pattern for the cast metal. Patterns are normally assembled in clusters around a common sprue and feeder system prior to building-up the external mold shell. Wax pattern is dipped in ceramic slurry, and adding coarse refractory stucco onto the wet slurry, the ceramic shell mold is built up around each wax pattern. The aforementioned procedures are repeated several times to make a shell mold with sufficient thickness, for strength and integrity, before being fired.

Given steps in the lost wax process, these multiple steps generate high cost and include many artifacts, thereby decreasing the accuracy of the targeted ceramic mold. Costly tooling is required to produce mold dies for complex cores and wax patterns by

injection molding. The cost and production delays associated with this tooling are a disadvantage for prototypes and smaller production runs.[3] Furthermore, when a lost wax pattern over a core part is added, movement or shifting of the core in the mold may occur. Since this slight displacement of the core results in unacceptable variations in the wall thickness of the hollow structure, it will decrease the consistency and accuracy of the ceramic core and shell mold designed for turbine airfoils with complex internal passageways. With one process rather than using separate cores, patterns, and shell molds, would be advantageous to directly produce a mold that has the casting cavity and the ceramic core.[4] In this work we demonstrate the fabrication of an integrally cored ceramic mold (ICCM) which combines the ceramic core with a ceramic mold shell in a single patternless construction, as shown in Figure 5. 2.

Solid freeform fabrication (SFF) techniques can be used to directly fabricate the mold without several intermediate steps of the conventional lost wax process.[5,6] SFF is the general name for an emerging technology in which sophisticated three dimensional (3D) objects can be produced directly from a layer by layer process based on computer aided design (CAD) files. Stereolithography (SL) invented by Chuck Hull[7] is the most commercialized technique among the SFF processes. It is considered to be the most accurate technique in terms of dimensional accuracy among the SFF techniques since it can produce 3D objects with exact tolerances and the best surface finishes.[7,8] However, SL is limited in its ability to produce a complex 3D IC pattern composed of only polymers due to the fact that it is a resin-based system. Thus, it is difficult to build any ceramic mold using the SL process since it requires extra steps similar to those used here in the lost wax process, as shown in Figure 5. 1. CerSLA[9-11] is used to directly build an

ICCM for the turbine airfoil by creating three-dimensional parts as a UV laser draws each layer on a photopolymerizable suspension of ceramic powder.

5.2 EXPERIMENTAL PROCEDURE

5.2.1 Suspension preparation

Irregular glassy silica powders (SiO_2, PCC airfoils, Sanford, NC) with an average size range of 3 μm d_{10}, 12 μm d_{50} and 66 μm as d_{90} was used to prepare a ceramic suspension. The silica powders were milled fused silica (density of 2.2 gm/cm^3). A quaternary amine dispersant (CC-59, Goldschmidt,) in an amount equal to 3% of the weight of the SiO_2 powder was added to lower the viscosity and aid in ceramic dispersion. The photopolymerizable monomer and monomer mixture were prepared using 1, 6-hexanediol diacrylate (HDDA, SR238) and ethoxylated pentaerythritol tetraacrylate (EPTA, SR494) as received from Sartomer company (Exton, PA). 1-Hydroxy cyclohexyl phenyl ketone (Irgacure 184, Ciba Specialty Chemicals, Tarrytown, NY) used as a photoinitiator decomposed on UV- radiation, releasing free radicals, which initiated the polymerization reaction of monomer mixtures. SiO2 powder and CC-59 as a dispersant for stable colloidal dispersion were added to UV-curable monomer mixtures without photoinitiator to prepare the ceramic suspensions. Up to a solid loading of 50 vol%, the suspension was mixed and homogenized in a high speed shear mixer for 5 min. At a solid loading of 60 vol%, more time was required for the dispersants to adsorb and colloidally stabilize the suspension, the mixtures were ball-milled for 24h. Hydroxy cyclohexyl phenyl ketone (HK) at a concentration of 2 wt% with respect to the monomer was added

to a 60 vol% suspension and the final mixture was ball-milled again for 2h.

5.2.2 WINDOWPANE technique

The WINDOWPANE technique is used to measure material properties cure depth (C_d), critical energy dose (E_c), and resin sensitivity (D_p) of fused silica dispersed suspension to obtain the proper energy dose required for writing a layer with 100 μm thickness. This technique consists of one frame and five separate double panes with different cure depths resulting from different laser beam exposure. The laser scans the surface of the suspension to draw a frame with the three horizontal lines, followed by the outline of the "panes". Next the laser scans the interior of each pane at different scanning velocities so that each pane receives a different dose. After fabrication of the windowpanes, the cured part is removed from the rest of the uncured suspension and rinsed in deionized water and then ethanol for acrylate suspension. Each windowpane thickness is measured with a micrometer to obtain the cure depth. From the linear curve resulting from the relationship between the cure depth and the maximum exposure, the resin sensitivity of suspension, Dp, and the critical energy dose of that resin, Ec, are obtained from the slope and intercept of the linear curve, respectively.

5.2.3 Fabrication of integrally cored ceramic mold using photopolymerization (ultraviolet curing)

A three-dimensional green part is fabricated by using a layer-by-layer CerSLA machine having the following steps. First, a 3D computer image is sliced into many cross-sectional layers 100 μm thick. As laser radiation is scanned on the surface of the

liquid monomer to write a layer, the monomer is solidified to a polymer. The laser is a solid state laser (Xcyte, JDSU, Milpitas, CA), which has a quasi-continuous wave (CW) emitting at 355 nm, output power 40 mW, and a beam diameter of 125 μm. The Ec and Dp measured by the WINDOWPANE technique are used to determine the laser speed by controlling the radiation exposure (mJ/cm^2) and build the layer thickness. Figure 5.3 shows the processing steps of CerSLA required to fabricate the ICCM. As laser radiation is focused in predefined areas on the surface of the liquid monomer to write a layer, the monomer is solidified to a polymer in Figure 5.3 (a). When the layer is finished, the support platform and first layer move downward into the vat of liquid monomer resin. The liquid monomer flows across the first polymerized layer, and then takes 40 seconds of "Z-wait time" to make a flat surface of suspension before building the second layer of monomer. The laser scans this new surface, polymerizing the second layer. This process is repeated many times until the part is finished. When part building is done, the platform is raised and the solid polymer part emerges from the vat. After fabricating a green part, the cured part is removed from the rest of the uncured suspension and rinsed in isopropyl alcohol for 20 minutes. As shown in Table 5.1, the solidified polymer in a green body is removed at temperature up to 600^oC in the binder burn-out process consisting of several heating steps. This temperature is maintained for 2 hours, and then the burned part is sintered at 1300^oC for 30 minutes in air. Optical images of the green and sintered bodies were taken by an OVM1000NM (Olympus) microscope.

5.3. RESULTS AND DISCUSSION

5.3.1 Integrally cored ceramic mold (ICCM) for turbine airfoil

Figure 5.4 shows a cross-sectional view of the internal features of most turbine airfoils typically containing three intricate cooling channels that form a cooling system. The channels are a leading edge cooling channel, a mid-chord serpentine cooling channel, and a trailing edge cooling channel. The mid-chord serpentine cooling channel facilitates the efficient removal of heat from the airfoil, especially at the intersection between the tip section and the trailing edge. Three complex internal passageways have been required for greater cooling efficiency of airfoils in turbines. Gas turbine engines workable at higher temperatures are being required for high efficiency of gas turbine engines. The airfoils, such as blades and vanes, within the engine are among the components exposed to significant thermal impact during engine operation. Therefore, as shown in Figure 5.4, interior cooling passages with complex hollow structure in the airfoils are used to prevent the degradation of the airfoils when exposed to high temperature.

Figure 5.5 demonstrates an ICCM with overall dimensions of 38.83 mm x 38.83 mm x 104.78 mm (X x Y x Z) for fabricating a turbine airfoil with complex cooling passages. The ICCM is composed of core, casting cavity, and shell parts, where the core generates internal cooling passages of a turbine airfoil. After molten metal cast into the ICCM through a pouring cup, the fused silica core is leached away in aqueous solutions of either NaOH or KOH.[12] The interior cavities resulting from the leached core are the three different cooling channels in a turbine airfoil, previously described, and shown in Figure 5.6.

Using CerSLA builds the ICCM for the turbine airfoil by creating three-dimensional parts as a UV laser draws each layer on a photopolymerizable suspension of ceramic powder. In order to generate each layer of the ICCM, a slicing step is required in CerSLA processing. The ICCM was sliced with a layer thickness of 100 μm so that 1047 layers were generated based on the Z height of 104.7 mm. Figure 5.7 shows five layers among 1047 layers of a sliced ICCM, where the initial root conducting air for cooling purposes is created in layer 200 and several passage ways mainly ranging from 400 and 800 layers are formed by the core and shell mold.

Given the sliced layers in figure 5.7, the cross section of STL file and a green body of ICCM are shown in Figure 5.8. The line in the image of STL file vertically cross-sectioned represents the position of the cross section. At the 400th layer, two separated parts are growing in the core region, where they turn into the leading edge cooling channel and mid-chord serpentine cooling channel after pouring casting metal and leaching out two parts. It only takes 50 seconds to build a layer, generally requiring 5.5 hours to build the green body of ICCM up to 400 layers.

For the high-quality surface of cast metal, the smooth inner surface in the green body of ICCM is required. During the building of green bodies, if stair stepping problems occur, the surface of sintered body and the interface between sintered body and cast metal will be affected. One of processing parameters affecting stair-stepping problem is the layer thickness, where thicker layers generate harmful surface quality of the green body. Due to the layer-by-layer process of the stereolithography, stair-stepping problems usually occur on the non-vertical surfaces.[13]

In order to investigate the stair-stepping problem at the green body of ICCM, the

inner surface shown in figure 5.9 was selected as the interface with the cast metal. The green body composed of 1024 layers has a layer thickness of 100 μm. An optical image shows 22 layers of the ICCM; there are no stair stepping problems at the inner shell surface.

5.3.2 Processing parameterization for optimum energy exposure in CerSLA

Figure 5.10 shows an image of a support structure, which is used to hold the part while it is being generated. For SL systems, anchor supports have been used to help control warpage that may occur during part fabrication using resins. For example, when photo-curable resin is exposed by UV light, it undergoes a polymerization reaction and shrinkage. Unconstrained shrinkage of pure resin induces curl, which leads to part inaccuracy. Therefore, the support structure has been used to not only hold a part, but to prevent curl and warpage in the case of pure resin for SL systems.

Figure 5.11 shows the gap between the core and shell was generated after building 800 layers, which is the passageway for the cast metal. When ICCM is produced via exposure to ultraviolet radiation on the suspension, the gap should be completely resolved to cast the metal between core and shell. At the initial stage, however, we could not resolve the gap for cast metals. A possibility of unresolved gap may be related to the support structures. We assumed that the unresolved gap was a drainage problem resulting from support structures. In order to examine the effect of support structures on the unresolved gap, an ICCM is built without any support structure. Although an ICCM does not include any support structure, the unresolved gap between the core and the inner wall of the shell was produced as shown in Figure 5.12. Therefore, a drainage problem

resulting from the support structure is not a reason of the unresolved gap.

Another possibility of unresolved gap may result from the complexity in the ceramic stereolithgraphy (CerSLA). The addition of ceramic powders in CerSLA creates a complex suspension having physical properties that differ from the pure resin in SL. Ceramic particles added to the acrylate monomer serve as scattering centers to the incoming radiation, as a result laser illumination occurs by multiple scattering of ceramic particles in the ceramic suspension and absorption by the photoinitiator. During photopolymerization of suspension, the most important parameter affected from this multiplied scattering is the resin sensitivity (D_p). As shown in Chapter 4, when the ceramic and the monomer have a large refractive index difference, the D_p decreases due to multiple scattering. Griffith et al. demonstrated the relationship between the refractive index and the D_p using several refractory ceramics: silica (n_{sio2}=1.56), alumina (n_{Al2O3}=1.72), and silicon nitride (n_{si3n4}=2.1), dispersed in the HDDA-based system (n_{HDDA}=1.46). The large refractive indices of alumina and silicon nitride produce smaller values of resin sensitivity than silica. Additionally, acceptable cure depths (D_c=200 microns stereolithography requirement) were not achievable with silicon nitride due to the large refractive index difference between the ceramic and diacrylate.[9,10]

Due to the complexity in the CerSLA resulting from the multiple scattering, inaccurate processing parameters, D_p and E_c, can be used such that they may lead to an unresolved gap between core and shell mold, as shown in Figure 5.12. If layers are overexposed due to inaccurate values, negative effects on the spatial resolution and overall dimensional control in the layers exist. For example, each layer can be overexposed due to incorrect cure depth, thereby influencing the cure width of each layer

and causing line width that are too large. The large width may block the gap between core and shell mold of ICCM fabricated by CerSLA.

The fundamental properties of the ceramic suspension, the resin sensitivity (D_p) and the critical energy does (E_c), are the most important parameters among the several processing parameters. When a layer is fabricated from the ceramic suspension in CerSLA, two parameters D_p and E_c vary the laser beam speeds (V_L). Figure 5.13 shows the relationship between V_L and E_c at constant D_p of 805 microns: V_L linearly decreased upon the increase of E_c. Therefore, if small or large E_c is used, these inaccurate parameters seriously affect V_L, and the smaller or larger energy dose (E) will be exposed.

D_p and E_c, of suspension including ceramic powders can be calculated from the relationship in Jacob's equation:

$$C_d = D_p \ln\left(\frac{E}{E_c}\right) \qquad 5.1$$

where E_c is the critical (minimum) energy dose required for polymerization, and E the exposure energy dose delivered to the surface. Exposure energy dose is $E=P_L/V_s h_s$, where P_L is laser power, V_s laser drawing speed, and h_s line spacing. Other parameters are cure depth (C_d), the distance of photopolymerization through the surface as targeted by the user and D_P, the distance at which the laser intensity is reduced by e^{-1}.

To resolve the gap between core and shell, Windowpane technique was applied to calculate two accurate parameters: D_p and E_c. Figure 5.14 shows that cure depth as a function of energy doses were measured using WINDOWPANE on the suspension

including 60 volume percentage of fused silica so that D_p of 805 ± 48 microns and E_c of 15 ± 1.29 mJ/cm^2 are calculated from the slope and the x-intercept value, respectively. Figure 5.15 (A) and (B) show the resolved gap of green body and sintered body, respectively. The calculated fundamental properties, D_p 805 microns and E_c 15 mJ/cm^2, are used to build a layer with 100 μm thickness so that the gap between core and shell mold is resolved. Therefore, the unresolved gap shown in Figure 5.12 is not a result of a drainage problem but inaccurate processing parameter.

5.3.3 Consistency and accuracy issues in Ceramic Stereolithography (CerSLA)

Consistency and accuracy are the important factors that should be considered when integrally cored ceramic molds (ICCM) are fabricated using CerSLA. For example, ceramic shell molds are required to have a constant thickness for strength and thermal behaviour predictions to avoid mold failure resulting from the cast metal.[4] In addition, for consistent and accurate cast metal, since the consistency and accuracy of green bodies affect those of sintered bodies, the ICCM green bodies should be produced within dimensional tolerances so that the CerSLA will be a process able to replace the lost wax process.

In the lost wax process, the accuracy and consistency problems generally occur due to the difficult control resulting from several processing steps. Investment casting techniques require very high temperatures, e.g., in the range of about 1450^{o}C to 1750^{o}C, while many conventional ceramic molds do not exhibit sufficient strength at those temperatures. Whiskers or plates as reinforcing materials have been used to increasing mechanical property of ceramic mold.[14,15] However, reinforcements of whiskers or plates

with anisotropic shape undergo preferred orientation during mixing or mold filling in ceramic injection molding process. The pattern of orientation in binder is partly dependent on the mold and gate configuration and on the machine conditions, notably injection speed, resulting in non-uniform distribution of binder.[14,15] Furthermore, mold thickness is not consistently controlled due to several dipping steps, making it difficult to control the mold thickness. Non-uniform distribution of reinforcement materials in binder and non-consistent mold thickness induce differential shrinkage during binder burn-out and sintering and alter the dimension of the mold, finally affecting the dimensional consistency and accuracy of a cast part. Generally, linear tolerances of about ± 0.15-0.25 mm are usually being recommended up to a size of 25 mm in the case of the conventional investment casting.[2]

In order to evaluate how accurately CerSLA can build an ICCM, the sizes of specific areas shown in Figure 5.16 are measured and compared with the core and shell parts in layer 630 of 4 samples. Figure 5.16 (a) and (b) show a STL file including core and shell parts, representing a cross section of the layer in a targeted ICCM and the cross section of a green body composed of polymer and ceramic material fabricated by CerSLA, respectively. Given the STL file of the layer, the size difference of green and sintered body (not shown) and shrinkage factor is compared and calculated. Symbols, A-A' to D-D' in Figure 5.16 (a) indicate positions measured in each demonstration to evaluate the accuracy of CerSLA. Table 5.1 displays the size difference resulting from the comparison between a green and a sintered body with the STL file, for both core and shell parts of the cross section of layer 630. At the positions of cross section measured in the X-Y plane, the linear tolerance of the green body are fairly controlled under ± 0.2

mm. After sintering, sintered ICCM shows the similar sintered factor of ~10 % in all axes (X-Y and Z).

Figure 5.17 demonstrates images showing a full size integrally cored ceramic mold: STL file, green body, and sintered body without any cracks at the core and shell parts. Given the STL file, after the ICCM green body shown in Figure 5.17 (b) was fabricated using CerSLA, the optimum thermal conditions are necessary during a BBO schedule consisting of a series of heating steps and multiple dwell times prior to ceramic densification. The solidified polymer is removed at temperatures up to 600^{o}C in the binder burn-out process. Here, the role of solidified polymer in CerSLA is to bind the homogeneously dispersed ceramic particles together. Since the cured resin will be removed in the binder-burnout step, it does not have to be very strong to impart adequate strength to the green ceramic. After removing the binding polymers, the sintered ICCM shown in Figure 5.17 (C) is fabricated through sintering at 1500^{o}C for 2 hours.

Position G shown in Figure 5.17 represents the trailing edge cooling channel parts, that could not be resolved by CerSLA at the current stage. Unresolved trailing edge parts may be generated by the following reasons: no support structure or tiny small size. The inner support structures used for sustaining the complex curved parts is difficult to completely remove, and hence residual support structures may block the cooling passage of ICCM. In the current experiment, support structures are not used so that trailing edge part is not supported and generated.

Another possibility of unresolved trailing edge parts is the small size of cross section at the trailing edge parts, which has thinnest size of 22 μm. In this case, the resolution of the processing is controlled by the cured line width which is dependent on

the beam size of UV laser. We are currently using a solid state laser with a beam diameter of 125 μm to build ICCM parts. The available smallest line width can be calculated using the beam size and resin sensitivity of the suspension, given by:

$$L_w = B\sqrt{\frac{C_d}{2D_p}} \qquad 5.2$$

where L_w is the line width of cured line, B the beam size, D_p resin sensitivity, and C_d is the thickness of cured line. The cured line width is directly proportional to the laser beam size and the square root of the ratio of the cure depth to the resin sensitivity. Given the current variables: B of 125 microns, C_d of 100 microns, and Dp of 805 microns, the solid state laser can resolve the smallest size with a line width of 44 microns. The resolution limitation in our CerSLA may be the reason that the thinnest size of 22 microns representing trailing edge is not resolved. In order to increase the resolution of CerSLA, since the cured lined width is directly related to the square root of cure depth, an approach is to decrease the cure depth. From the equation 5.2, cure depth of 50 microns is required to resolve the thinnest size of 22 microns.

5.4 CONCLUSION

Ceramic stereolithography (CerSLA) as a novel process is investigated to replace the lost wax process which is a technique widely used to fabricate refractory molds for investment casting. In the lost wax process, however, several problems, lead time delay and high cost for pattern production and the risk of core motion during wax injection, are generated from the several processing steps: core preparation, injection molding, and dipping process. In the CerSLA process, on the other hand, the mold can be directly fabricated without several intermediate steps of the conventional lost wax process. In this work we demonstrate an integrally cored ceramic mold (ICCM), the ceramic core with a ceramic mold shell in a single patternless construction, for turbine airfoils with complex internal passageways.

CerSLA creates a complex ICCM as a UV laser draws each layer on a photopolymerizable suspension of ceramic powder. Due to the layer-by-layer process, stair-stepping problems usually occur on the non-vertical surfaces, while there is no stair stepping problems at the inner shell surface of ICCM. At the initial stage, the gap as the passageway for the cast metal between core and shell could not be resolved. The unresolved gap is induced from inaccurate processing parameter, since the complexity in the CerSLA increases as ceramic powders serve as scattering centers to the incoming radiation, as a result, laser illumination occurs by multiple scattering of ceramic particles in the ceramic suspension and absorption by the photoinitiator.

The WINDOWPANE technique can produce two fundamental properties of ceramic suspension: resin sensitivity (D_p) and critical energy dose (E_c). When 60 volume

percentage of fused silica is dispersed into 1,6-hexanediol diacrylate (HDDA), D_p of 805 ± 48 microns and E_c of 15 ± 1.29 mJ/cm^2 are calculated from the slope and the x-intercept value in the cure depth as a function of energy doses, respectively. Furthermore, CerSLA directly controls the desired thickness of shell molds over inconsistent state resulting from the several dipping steps in the lost wax process and shows fairly accurate geometry dimensions (within 0.20 mm) which are fitted into the linear tolerance required in the conventional casting.

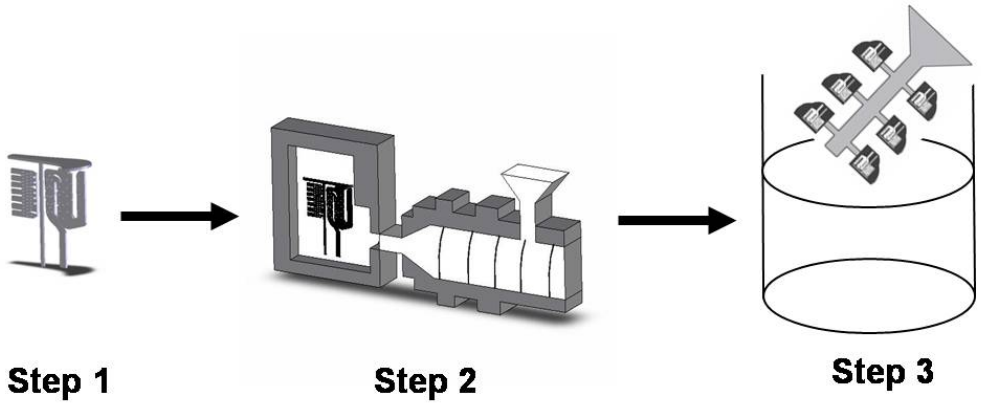

Figure 5. 1 Schematic diagram of the several processing steps in the conventional lost wax process how to build ceramic mold for super alloy airfoils; (a) Step1: make core, (b) Step2: mold wax pattern to define metal, and (c) Step3: build shell mold over wax pattern.

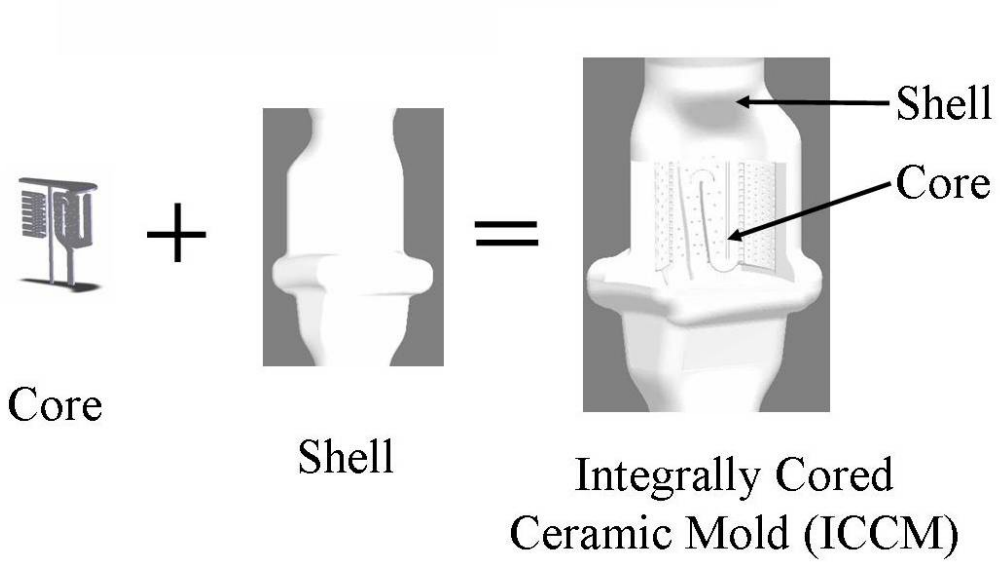

Figure 5. 2 Schematic diagram of targeted integrally cored ceramic mold (ICCM) fabricated by ceramic stereolithography (CerSLA).

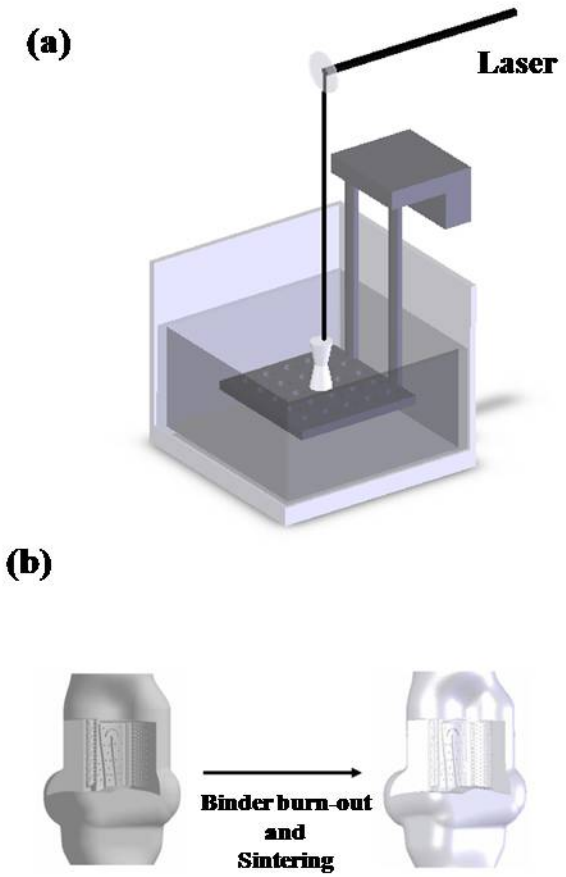

Figure 5. 3 Schematic diagram of the fabrication of integrally cored ceramic mold (ICCM): Outline of fabrication procedures for ICCM made by ceramic stereolithography (CerSLA)

Table 5. 1 Thermal condition for binder burn-out and sintering

	Temperature (^{o}C)	Rate (^{o}C/min.)	Holding time (hour)
Binder burn-out	25 (room temp.) - 100	5	1
	100 - 200	5	2
	200 – 335	3	2
	335 – 415	1	2
	415 – 480	3	2
	480 – 600	2	2
Sintering	25 – 1300	3	0.5
Cooling	1300 – 300	5	0
	300 – 25 (room temp.)	1	0

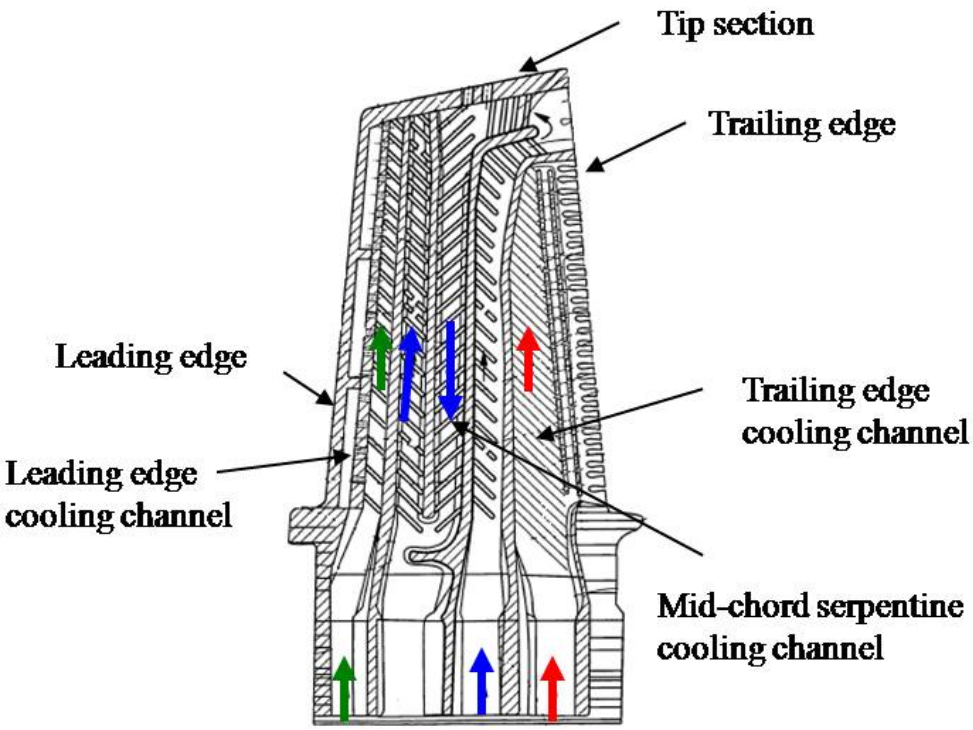

Figure 5. 4 A cross-sectional view of a turbine airfoil.

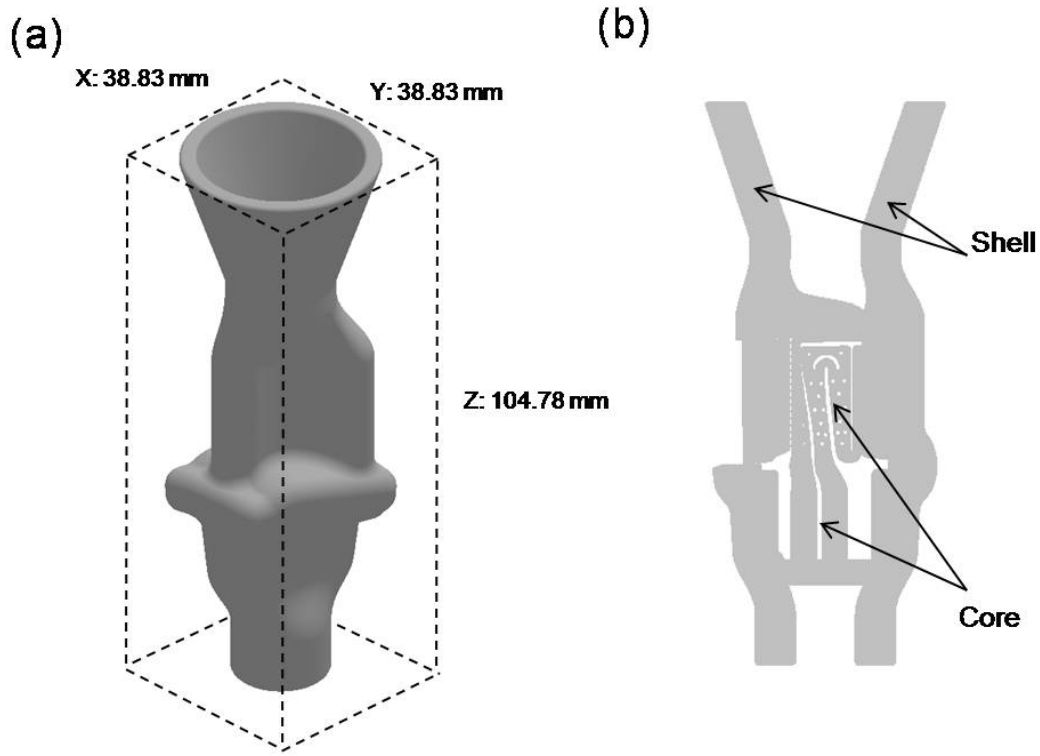

Figure 5. 5 Integrally cored ceramic mold (ICCM); (a) the size of ICCM and (b) the cross section of ICCM showing core and shell parts.

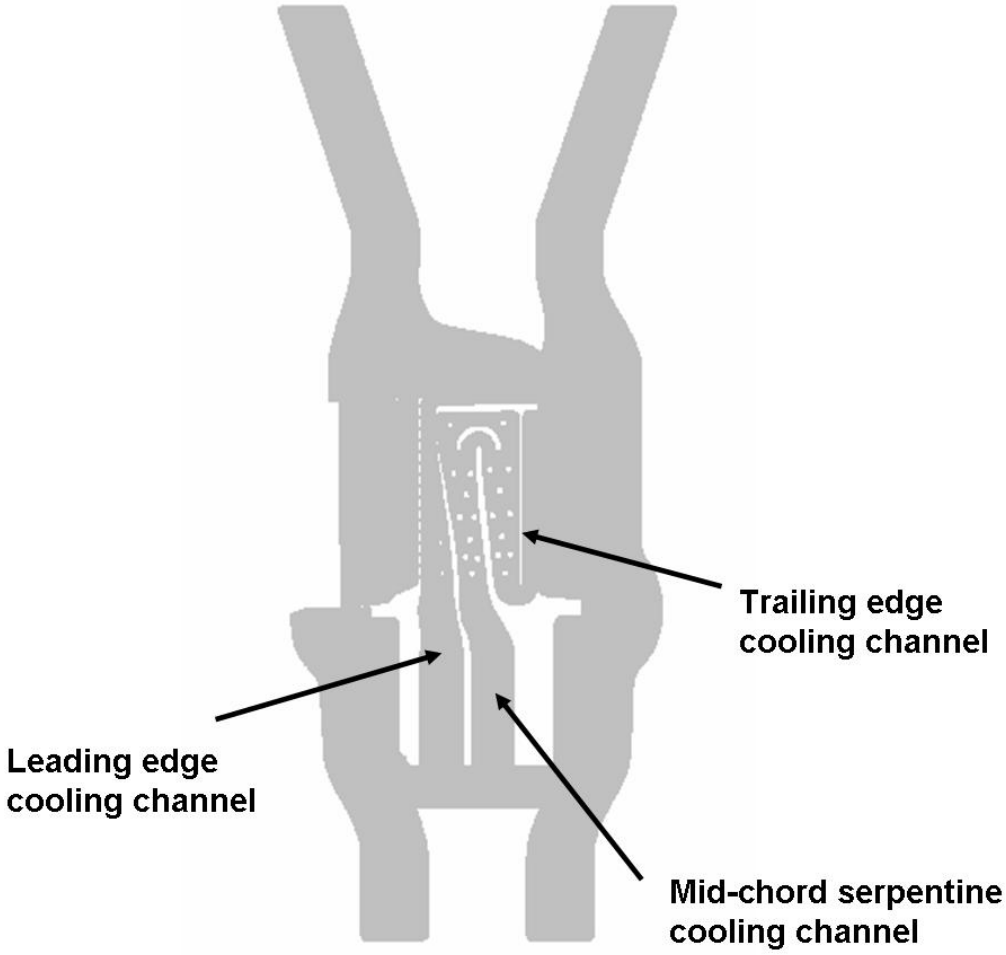

Figure 5. 6 A cross-sectional view of ICCM showing three cooling channels; Leading edge cooing channel, Mid-chord serpentine cooling channel, and Trailing edge cooling channel.

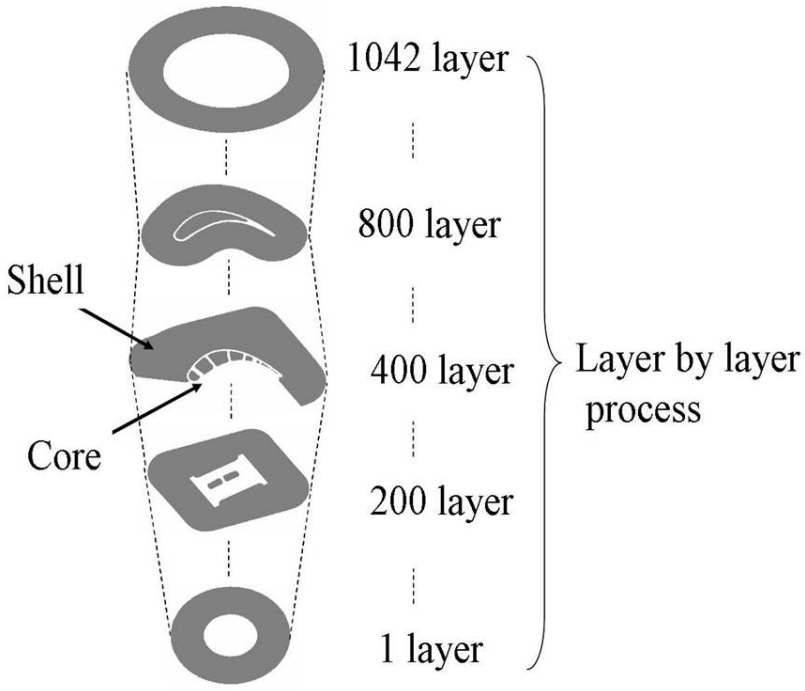

Figure 5. 7 Integrally cored ceramic mold (ICCM) has been built using layer by layer process, which has 1042 layers with the thickness of 100 μm. Core and shell parts are shown between 200 layer and 800 layer.

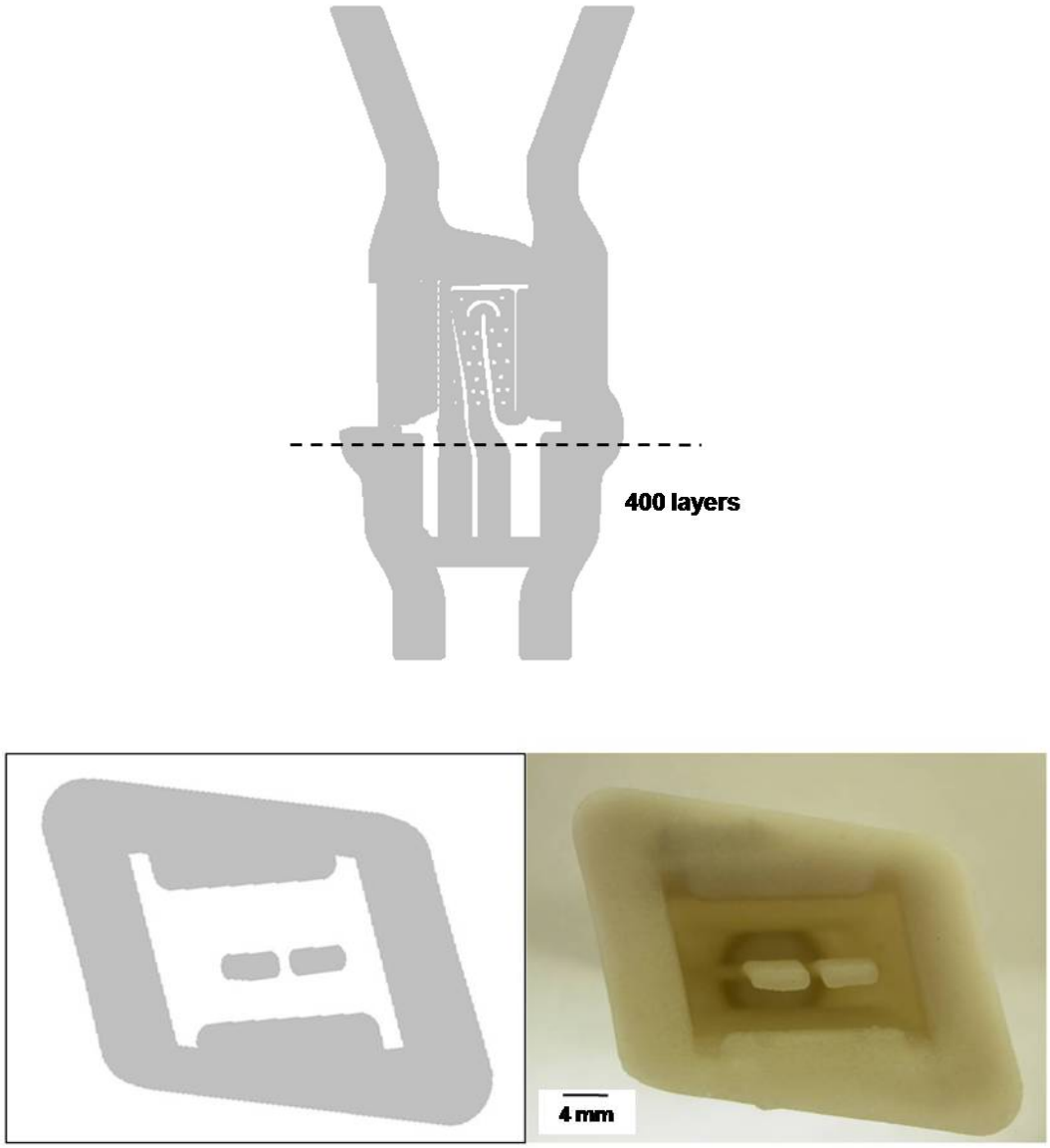

Figure 5. 8 An image showing a layer of 400 at the root part. The image represents core (red circle), casting cavity, and shell parts, which are built using layer by layer process.

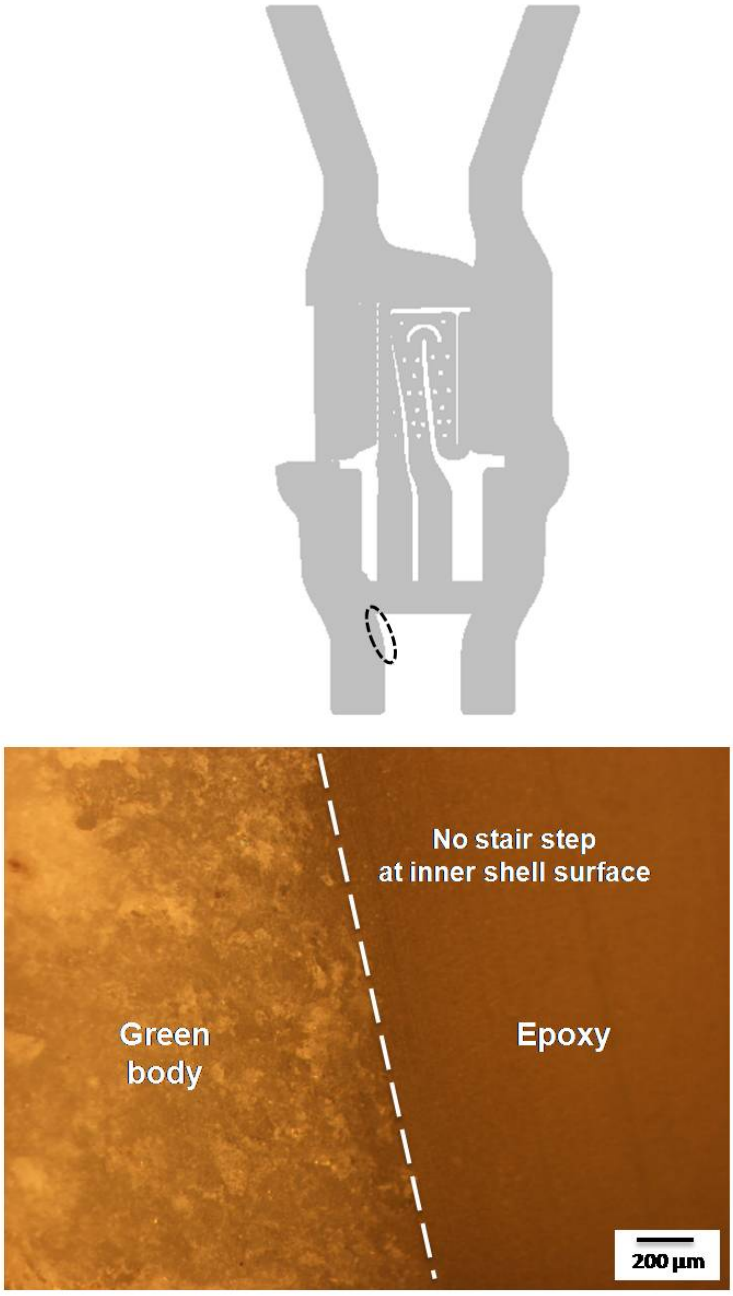

Figure 5. 9 No stair stepping at inner shell surface of ICCM, which has layers with layer thickness of 100 µm.

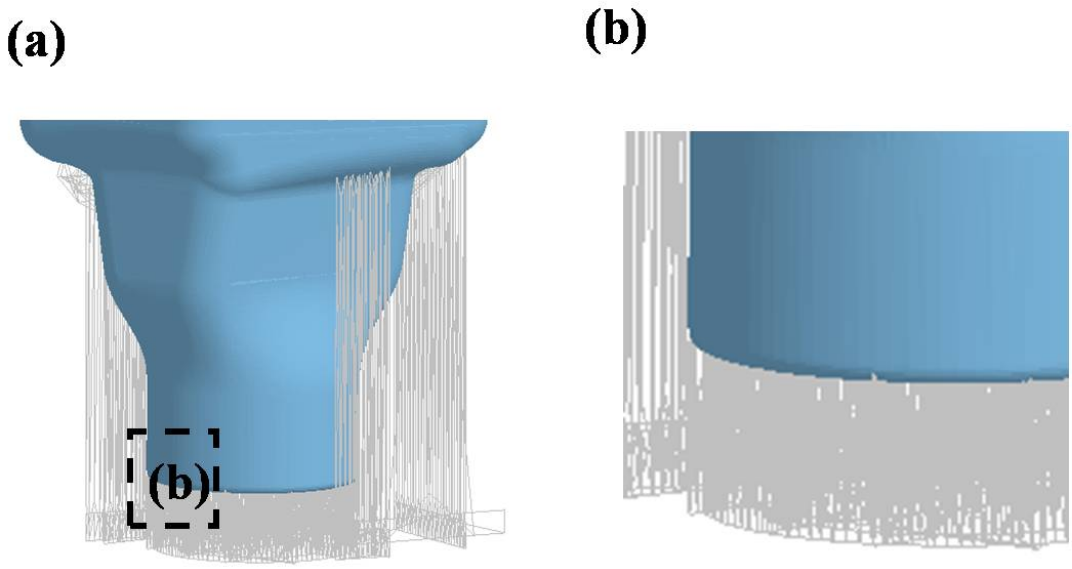

Figure 5. 10 An image showing a support structure used to hold the part while it is being generated; (a) a support structure used for simple cubic box and (b) the image magnified from the region (A).

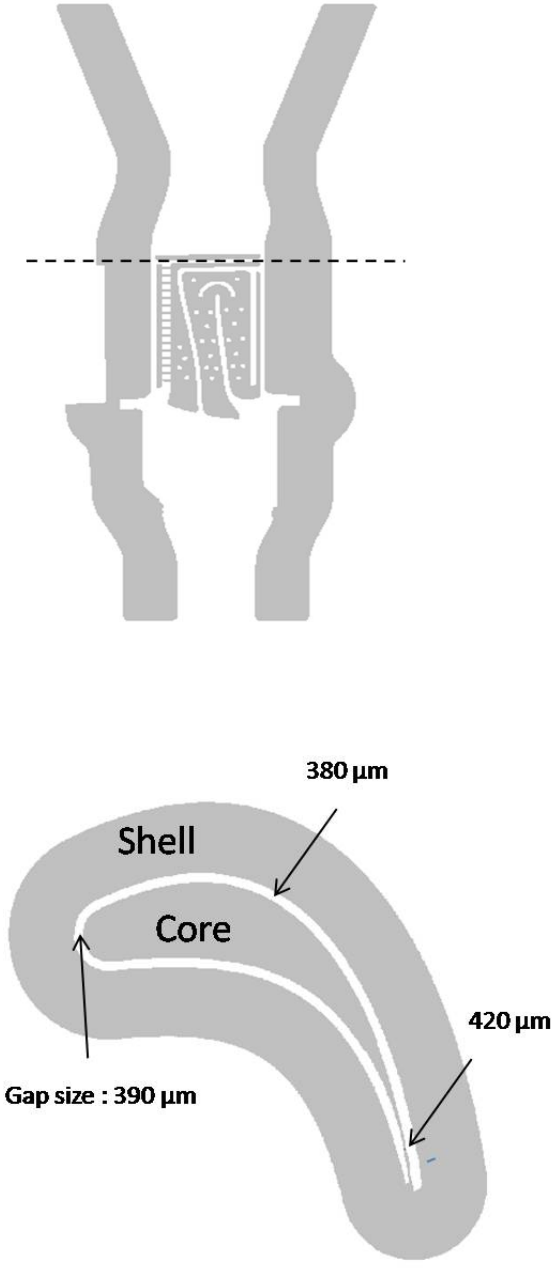

Figure 5. 11 Image of gap between core and shell. The gap is the passageway for the cast metal.

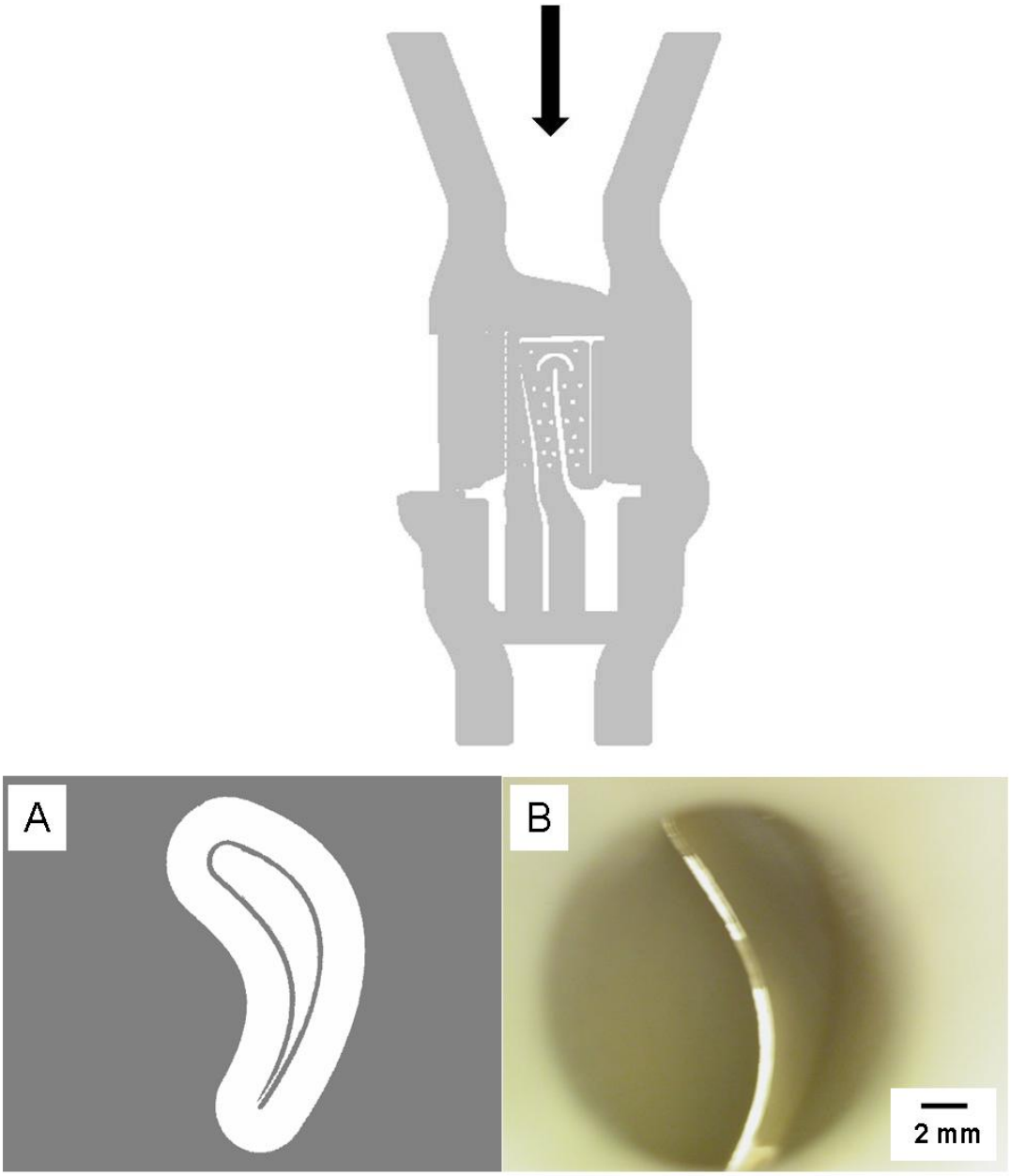

Figure 5. 12 Gap between core and shell for the passageway for the cast metal; A. STL file for the gap and B. Unresolved gap.

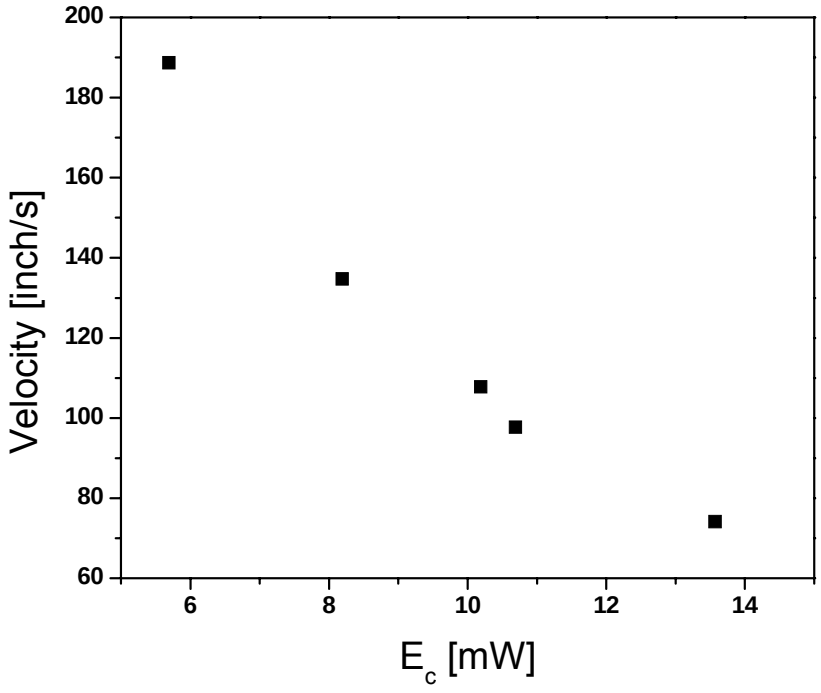

Figure 5. 13 Laser beam velocity as a function of energy dose

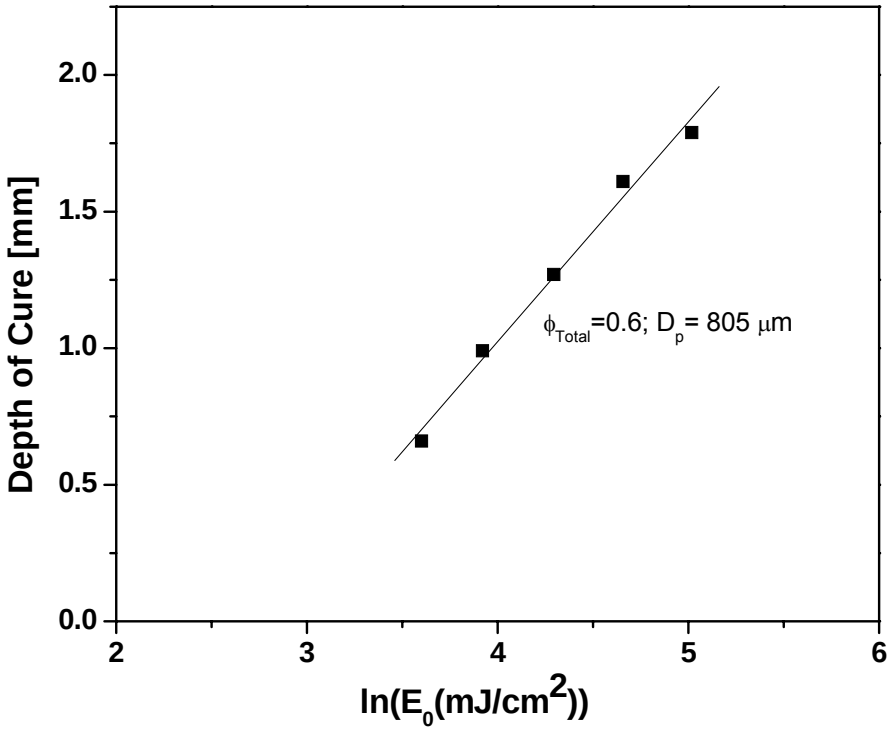

Figure 5. 14 Cure depths as a function of energy doses measured using WINDOWPANE technique on the suspension including 60 volume percentage of fused silica. The resin sensitivity (D_p) and critical energy dose (E_c) calculated using Eq. 5.1 are 805 μm and 15.33 mJ/cm^2.

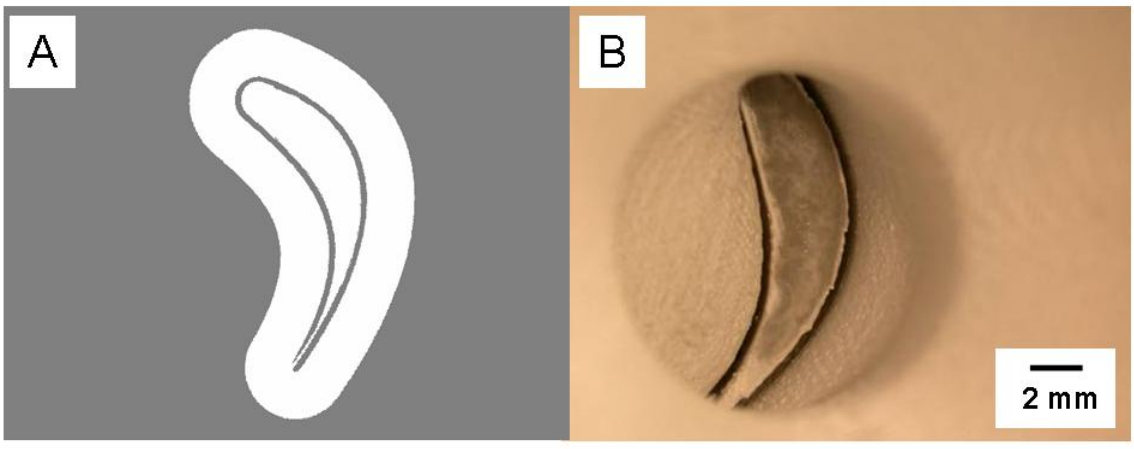

Figure 5. 15 Resolved gap between core and shell mold; A. STL file and B. Resolved gap of green body

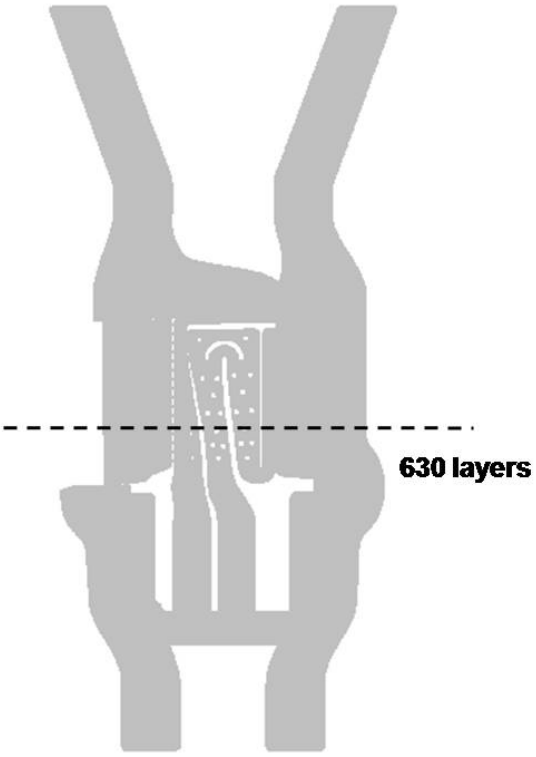

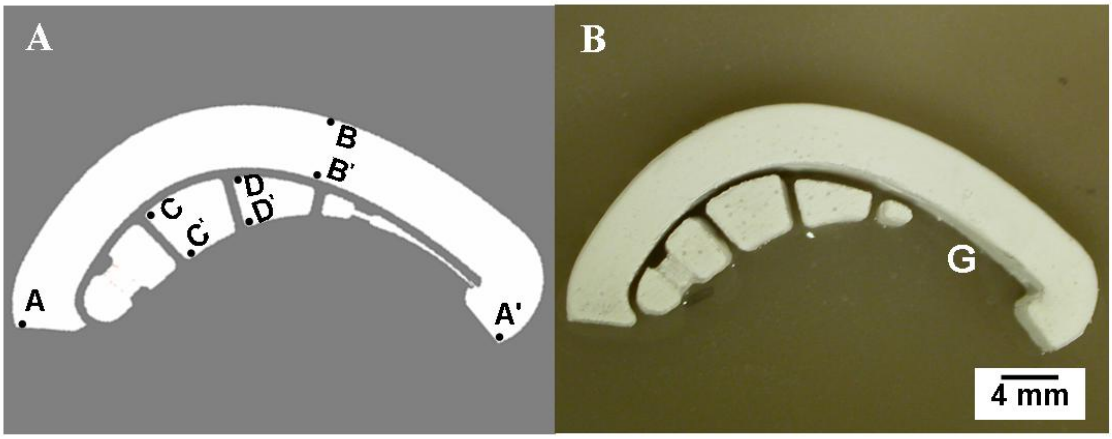

Figure 5. 16 Demonstrations in order to measure the accuracy of the integrally cored ceramic mold (ICCM) built by CerSLA. A. STL file and B. Green body of ICCM with core and shell mold at the layer number 630 (A-A' to D-D': measured length, G: missing part)

Table 5. 2 Evaluation on accuracy of CerSLA from the comparison between STL file and Green body of ICCM

		As-built before sintering state		After sintering state	
Axis	Part	STL file	Green body	Sintering shrinkage (%)	Sintered body
X-Y	A-A'	33.6	33.37±0.11	10.8	29.72±0.07
	B-B'	4.66	4.42±0.11	10.9	3.93±0.07
	C-C'	4.72	4.60±0.1	10.7	4.11±0.08
	D-D'	**3.89**	3.87±0.09	10.9	3.45±0.04
Z	E-E'	**26.67**	26.71±0.17	10.6	23.91±0.05
	F-F'	**22.72**	22.81±0.07	10.7	20.36±0.04

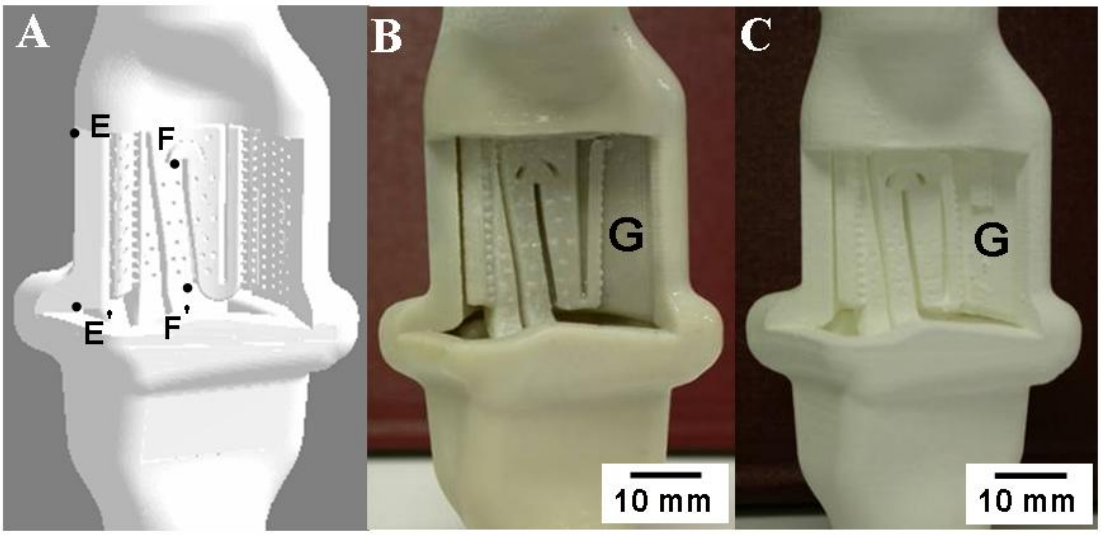

Figure 5. 17 Integrally cored ceramic mold (ICCM) for turbine airfoil with a complex internal hollow structure fabricated used ceramic stereolithography (CerSLA); A. STL file, B. Green body, and C. Sintered body without any cracks at core and shell parts. (E-E' and F-F': measured)

Reference

1. C. F. Caccavale, W. E. Sikkenga, "Investment casting using core with integral wall thickness control means", *US Patent* 5 296 308, 1994.
2. P. R. Beeley, R.F. Smart, *Investment Casting*, The university press, Cambridge, UK, 1995, 65.
3. C. M. Cheah, C. K. Chua, C. W. Lee, C. Feng, K. Totong, "Rapid prototyping and tooling techniques: a review of applications for rapid investment casting", *Int. J. Adv. Manuf. Technol.*, *25*, 308, 2005.
4. D. J. Frasier, M. Kush, M. E. Schlienger, M. Baldwin, "Method and apparatus for production of a cast component", *US Patent 6 932 145*, 2005.
5. J. W. Halloran, "Freeform fabrication of ceramics ", *Br. Ceram. Trans. J.*, *98*, 299, 1999.
6. F. Doreau, C. Chaput, T. Chartier, "Stereolithography for manufacturing ceramic parts", *Adv. Eng. Mater.*, *2*, 493, *2*000.
7. P.F. Jacobs, *Rapid Prototyping & Manufacturing– Fundamentals of Stereolithography*, SME, La Crescenta, California, 397, 1992.
8. D. Mills, "Ceramic mould material", *US Patent* 5 143 777, 1992.
9. M.L. Griffith, "Stereolithography of Ceramics", Ph.D. Thesis, University of Michigan, 1995.
10. M. L. Griffith, J. W. Halloran, "Freeform fabrication of ceramics via stereolithography", *J. Am. Ceram. Soc*., *79* [10], 2601, 1996.
11. M.L. Griffith and J.W. Halloran, "Scattering of Ultraviolet radiation in turbid

suspensions", J. Appl. Phys. 81, 2538, 1997.

12. I.C. Huseby, M.P. Borom, and C.D. Greskovich, "High temperature characterization of silica-base cores for superalloys", *Am. Ceram. Bull*., **58** [4], 448-52, 1979.

13. C. M. Lynn, D. W. Rosen, "Usage of accuracy models in stereolithography process planning", *Rapid prototyping journal*, *6* [2], 77, 2000.

14. A. Ghosh, F. J. Klug, P. H. Monaghan, P. S. Svec, and R. A. Giddings, " Reinforced ceramic shell mold and related processes", *US Patent* 6 352 101, 1999.

15. S. J. Stedman, J. R. G Evans, R. J. Brook, and M. J. Hoffmann, "Anisotropic sintering shrinkage in injection moulded composite ceramics: *J. Eur. Ceram. Soc*., *11*, 523-532, 1993.

CHAPTER 6

INFLUENCE OF RESIDUAL MONOMER ON THE CRACKS IN INTEGRALLY CORED CASTING CERAMIC MOLD (ICCM)

The goal of ceramic stereolithography (CerSLA) is to replace the traditional wax-pattern investment casting with tool-less rapid prototyping methods. CerSLA is used to build silica-based refractory molds as complex "integrally cored ceramic molds" (ICCM), which are novel investment casting shell molds with the core already in place. For details about the integrally cored ceramic mold, the reader is referred to Chapter 5. In order to fabricate the integrally cored ceramic mold (ICCM) for turbine airfoil, the green body of the ICCM fabricated by CerSLA must be fired to remove the cured polymer binder and to sinter the ceramic. After the mold is fired, no macro cracks or flaws should exist in the sintered ICCM, which should have sufficient mechanical properties to avoid ceramic mold failure resulting from the cast metal. However, early in the project, molds made by CerSLA had severe flaws. As shown in Figure 6.1, vertical and horizontal cracks exist in the sintered ICCM fabricated by a 50 volume percentage suspension of fine silica powder (average particle size ~ 7μm). This chapter describes how the causes of these flaws were identified and eliminated, and presents a process optimization for fabricating a macro horizontal-flaw-free integrally cored ceramic mold (ICCM).

6.1 BUILD STYLES

Ceramic stereolithography (CerSLA) builds ceramic green objects from CAD files from many thin liquid layers of powder in monomer, which are solidified by polymerization with a UV laser, thereby "writing" the design for each slice. A layer is written according to a "build style" which controls X and Y directions of the UV laser. If a build style is incorrect, defects such as delamination, distortion, and bending in the green body can be induced. The origin of the distortion is the inevitable volume decreases when the monomers are polymerized. The "build styles" involve strategies to suppress macroscopic distortions related to volume change. It is important to find the proper build style for ceramic suspensions. Since CerSLA originates from the stereolithography (SL) based on the photopolymerizable monomer system with no ceramic filler, the build styles widely used in the conventional unfilled resin system are explained.

6.1.1 Conventional build style in the resin system: Tri-Hatch to WEAVE

Recall that the SL builds by curing strings of resin as the laser is scanned to cure the resin. When the stereolithography process was developed (Jacobs), the layers were cured by defining the outside "Border lines" first, then curing the inside with a series of "Fill lines" in a hatch pattern.[1] The fill lines can connect between two border lines, or they can connect to just one border line and leave a small gap between the other lines (an "end contraction").

Tri-Hatch was the most widely used internal hatch style of resin system. Tri-Hatch, a method used to solidify the inside of a part or the volume between borders, uses a

scanned line parallel to the x axis combined with lines at 60^{o} and 120^{o} to the x axis. The most common spacing between these lines is 1.25 mm, thus producing an internal structure of equilateral triangles. However, within a laser-cure, too much residual resin remains in the SL part structure, which directly influences the post-cure distortion. Specifically, a large fraction of uncured liquid resin (roughly 50%) remains, which leads to excessive post-cure distortion.

To reduce the amount of residual liquid resin, WEAVE style was developed. This style considerably improves post-cure distortion when compared to parts built using the Tri-Hatch method.[2] WEAVE typically uses two sets of orthogonal vectors per layer, which draws a set of parallel Y-hatch vectors was drawn on the first pass, followed by an orthogonal set of parallel X-hatch vectors drawn on the second pass. Hatching spacing is approximately 0.011″ for both the x and y hatch.

WEAVE build style advanced from Tri-Hatch minimizes the postcure distortion by reducing the amount of uncured monomer, but this process can produce large solidified regions that are a dominant cause of part distortion. This distortion is due to internal stresses developed during part building, with the most significant distortions occurring on large, nominally flat slabs. For example, as shown in Figure 6.2 (a), the short vectors drawn using the WEAVE style sequentially writes the border line, X-hatch vectors from left to right, and Y-hatch vectors from the front of the vat toward the back. In this process, the Y-hatch vectors attach to the border line and the previous layer partially polymerized by the border vectors and the X-hatch vectors. Subsequent shrinkage is generated from the left toward the right according to a propagating “wave” of curing. Figure 6.2 (b) shows a distorted thin vertical wall exaggerated for the purpose

of visual representation. The curvature shown is attributed to the net result of subsequent shrinkage at the parts largely attached to the lower layer and the border lines.

Build styles are being developed to avoid the dominant source of error, like part distortion resulting from internal stress developed during part building, with the most significant distortions occurring when large, flat, and complex 3-D objects are built. One recently developed build type is the STaggered weave build style. The style enables internal stresses to be released using the smallest contact area between cure lines based on STaggered hatch and Retracted hatches.

6.1.2 STaggered weave build style

6.1.2. a) STaggered hatch

Figure 6.2 shows the conventional hatch of WEAVE style and STaggered hatch of Staggered WEAVE style. Most significant distortions under the conventional WEAVE style occur due to internal stresses developed during part building. Since WEAVE style was similar to building a brick wall with all the bricks located directly on top of one another, the full height of the wall in a straight line is extended. As shown in Figure 6.3 (a), a UV laser controlled by conventional WEAVE style writes the X hatch vectors on the nth layer which are positioned directly above the X vectors on the (n-1)th layer. The Y vectors are also positioned directly above one another. However, the weaker regions exist between the hatch vectors as the maximum values of solidified areas are located directly down the centerline of each vector. Those weaker regions should be diminished, because the regions are possible to be used as the area generating tiny cracks resulting from the internal stresses developed during part building.

STaggered hatch is developed in order to reduce internal stress as filling the weaker regions between layers.[3] STaggered hatch style is a similar method that the bricks are "staggered" to avoid weak spots and a tendency to develop long cracks directly down a given mortar line. As shown in Figure 6.3 (b), the fill vectors on the *n*th layer are offset by exactly half the regular hatch spacing ($h_s/2$), relative to fill vectors on the (*n*-1)th layer. The advantage of this hatch is to intentionally offset the fill vectors on successive layers to reduce stress concentrations along the relatively weaker regions between fill vectors.

6.1.2. b) Retracted hatch

In the conventional build types, the shrinkage resulting from a reaction between a given cured border vector and hatch vector would be the dominant source of error on part accuracy. In addition, Tri-Hatch and WEAVE types cause another problem as all hatch vectors are attached to the border vectors. As shown in Figure 6.4, when a solidified line is written by a UV laser, it undergoes shrinkage on the first pass due to its attachment to the borders on both ends. Hatch lines attached at both borders increase the net effect of the shrinkage forces, thus generating considerable internal forces. Those forces lead to the distortion near an end part of borders and reduce part accuracy.

Retracted hatch style is developed to avoid the internal forces escalated near border vectors, which connects one end of each hatch vector to one of the borders.[2] Hatch vectors in X or Y direction are only attached at one and only one border so that the first pass hatch vectors do not generate any reactive forces resulting from shrinkage forces to be exerted on the borders. Figure 6.4 shows the retracted hatch style in which the other end of the hatch vector is disconnected about 250 μm from the adjacent border. Note that

the retraction sequence itself is alternated such that a given X-hatch vector is attached to the border on one end, while its nearest neighbors will be disconnected at that end. This end contraction of retracted hatch type releases continuous increment of the internal stress.

Given the STaggered weave build type, the ceramic green body of ICCM from CAD files is built using Ceramic stereolithography (CerSLA). Contrary to the processing of photopolymerizable monomer system with no ceramic filler, the CerSLA process for fabricating sintered ceramic casting mold requires extra processing steps; a binder burn-out step to remove polymer from the green body and a sintering step to densify the ceramic. We find that flaws appear during the subsequent heating of the green body. This chapter presents evidence that the origin of these flaws is related to uncured monomer, which the wall, polymerized during heating to 200^{o}C, as well as effects due to burnout of the polymer (~300-600^{o}C), which are aggravated by sintering shrinkage upon subsequent high temperature firing (~1500^{o}C). These phenomenon are investigated by various experiment techniques.

6.2 EXPERIMENTAL INSTRUMENTATION

6.2.1 Thermogravimetric Analysis (TGA) and Differential Scanning Calorimeter (DSC)

Samples of 5-20 mg placed in alumina pans were used to detect optimal thermal condition. The thermal degradation characteristics were examined by TGA in an SDT2960 TA simultaneous TGA-DTA instrument. Simultaneous recording of the TGA-

DTA data allows for observation of the temperatures corresponding to the maximum rate of mass loss. The heating rate consisted of 5ºC/min to 600ºC in atmospheres of air.

The heat flow during polymerization were detected using differential scanning calorimetry (DSC) at a heating rate of 5^{o}C/min, using a TA Instruments Inc., Thermal Analyst model 2100 system equipped with a model 2910 MDSC cell. The sample compartment was subject to a constant purge of dry nitrogen at 50 ml min^{-1}.

6.2.2 Gas chromatography/Mass spectrometry (GC/MS)

Powder was prepared from crushing a SLA cured green sheet with the layer thickness of 1 mm and retracted hatch of 200 μm. The powder was submerged in the dichloromethane (CH_4Cl_2) for 4 hours to extract residual monomer at the retracted hatch. The extract was analyzed on a Finnigan Trace GC/MS, equipped with a Supelco SLB-5 column, 30 meters long x 0.25 mm I.D. Helium at 1 ml/min was used as the carrier gas. The injector temperature was 200 C., set up for a splitless injection. The oven temperature was held at 30 ^{o}C for 3 minutes, and then heated to 275^{o}C at 20 degrees per minute. The mass range was set from m/z (mass-to-charge ratio) 35 to m/z 400, with electron energy of 70 eV. Identification of the components was done by comparison of the mass spectra with ones found in the Wiley NBS library.

6.2.3 CerSLA condition

A photopolymerizable suspension is prepared from ceramic particles, a photoreactive monomer solution, and photointiator are firstly prepared. Initially, the silica powder is suspended in a solution of hexane diol diacrylate (HDDA) and ethoxylated

pentaerythritol tetraacrylate (EPETA), using a Variquat CC59 (a polypropoxy quaternary amine modified with an acetate polar group) as a dispersant. Photoinitiation is performed by using a 325 nm UV laser in an SLA 250/40 stereolithograpy apparatus in the presence of an Irgacure 184 (a hydroxyketone) as the photoinitiator.

The acrylate-based suspension is polymerized via free radical polymerization initiated by UV radiation. The free radical polymerization generally occurs based on the following steps. When photo-initiators are exposed to UV light, they generate radicals which play a role of breaking the carbon double bonds of the acrylate functional group in the monomer. Acrylate monomers with broken acrylate functional group link together to make a polymer, which fabricate the green body resulting from the acrylate based suspension.

6.3 Horizontal and Vertical Cracks during Binder Burn-Out (BBO)

6.3.1 Optimum thermal condition to remove organic binder and sinter ICCM

In order to successfully eliminate the polymer from the green body, the optimum thermal conditions are necessary during a BBO schedule consisting of a series of heating steps and multiple dwell times prior to ceramic densification. Practically, the yield of ceramic processes is not so much due to a variety of defects resulting from binder removal. For instance, carbon retention, cracking, blistering, warping, anisotropic shrinkage, and delamination of fired bodies can all result from binder removal. Thermogravimetric analysis (TGA) is an effective tool able to identify temperature regions of rapid mass loss used to obtain thermal conditions for several heating steps and

dwell times in a BBO schedule.[4] Using TGA-DTA represents the weight loss and temperature difference as a function of temperature, as shown in Figure 6.5. TGA plots provide evidence that all organic binders are removed below 600^{o}C in atmosphere of air. They show four main mass removal events, the first of which occurs from 200 to 335^{o}C removing 4 wt% of material, the second exothermic event from 335 to 415^{o}C removing 21 wt% of material, and the third exothermic event from 415 to 480^{o}C removing 3 wt% of material, and the final event from 480 to 600^{o}C removing the final 5 wt%. The exothermic events of the process demonstrate that the degradation involves oxidation reaction.

Given the TGA results, a BBO, sintering and cooling schedules shown in Figure 6.6 were designed. Since 21 wt% of the binder is quickly removed at the second event from 335 to 415^{o}C, 1^{o}C per minute as a heating rate is used to prevent any defects resulting from fast binder removal. The porous ceramic mold is obtained after removing all binders in the green body, and then it is sintered to densify ceramic powder at 1500^{o}C. Especially, the more cautious cooling schedule is required in order to decrease the abrupt contraction of sintered body. Since this contraction results from the phase transformation of cristobalite from β to α phase between 250^{o}C and 150^{o}C during cooling induced microcracks and decreased mechanical strengh of ceramic sintered body, cooling rate of 1 degree per minute was used at the temperature region.[5]

6.3.2 What is the origin of vertical and horizontal cracks detected during binder burn-out?

As can be seen in Figure 6.1, after experiencing the thermal conditions to remove the organic product and subsequent sintering of the green body, the sintered ICCM exhibits cracks. To describe the origin of the crack, a cube shaped green body is used to accurately detect the temperature at which cracks initiate during BBO. The state of cube shaped green body is monitored at regular temperature increments of 20^{o}C to 600^{o}C based on the thermal conditions in Figure 6.6. Figure 6.7 shows macro horizontal and vertical cracks in the cube shaped green body during BBO. Cracks initially are found around 240^{o}C. Comparing with TGA in Figure 6.5, very little weight loss at 240^{o}C suggests that the cracks do not directly result from BBO. More and longer cracks, horizontal and vertical cracks, are detected at 400^{o}C. Those cracks mean that cracks in the sintered ICCM shown in Figure 6.1 already exist during a BBO process.

Note that vertical cracks also exist in the green body during BBO. Green bodies are built by the layer-by-layer process of CerSLA, easily including horizontal cracks generated from weak bond of layers after BBO. However, vertical cracks are not observed as frequently. Given the vertical and horizontal cracks, the question arises as to the origin of the cracks detected during binder burn-out and ways to prevent them. The relationship between the cracks and the build style is considered as the origin of the cracks. Since CerSLA process utilized STaggered and Retracted hatch type in the STaggered method to relieve internal stress by intentionally leaving residual monomer in the green body, as shown in Figure 6.3 and 6.4., the cracks in the green bodies during BBO may be connected to the build style used in CerSLA process.

In the case of photopolymerizable monomer system with no ceramic filler, the free-radical photopolymerization reaction is exothermic. Measuring the heat flow from the sample during UV irradiation monitors the kinetic parameters, the rate of polymerization (R_p) and percentage conversions of monomer. R_p and percent conversion of monomer represent the number fraction of C=C bonds reacting in the sample per unit dose at the initiation and propagation steps and the total amount of converted monomer after termination.[6] Those kinetic parameters were not only reliant on the UV irradiation, but also raising the isothermal curing temperature has enhanced kinetic parameters; rate of polymerization (R_p) and percentage conversions of monomer. The increase of kinetic parameters results from a thermal contribution towards the photo-radical polymerization of the acrylates and increase of mobility of the unreacted monomer during initiating and propagating in the network.[7]

In the CerSLA process, Heat energy applied during a binder burn-out process to remove polymer in the green body may influence the polymerization of the unreacted monomer. DSC (Differential Scanning Calorimeter) is used to measure the exothermic heat flow from the free-radical polymerization, examining the thermal decomposition of the hydroxyketone photointiator at polymerization in the monomer system including hexane diol diacrylate (HDDA), ethoxylated pentaerythritol tetraacrylate (EPETA). Figure 6.8 shows the exothermic heat flow, representing polymerization of photopolymerizable monomer system generated by thermal degradation of photoinitiator around 190^{o}C. The exothermic reaction means that the rest of uncured monomer in the green body can be polymerized by heat energy during a BBO process. We hypothesize that cracks are generated by the internal stress resulting from volumetric change of

uncured monomers polymerized through the heat energy. The sites in which a residue of monomer can be located are roughly the middle and end part of each layer in the green body resulting from STaggered and Retracted hatch build type.

6.4 STAGGERED WEAVE BUILD TYPES VS. CRACKS

6.4.1 STaggered hatch space vs. Cracks

In the STaggered hatch build type, the amount of residual monomer is dependent on hatch space defined as the distance between the centerlines of adjacent parallel hatch type in the STaggered build method. Firstly, in the case of conventional resin system, optimum hatching space is obtained using the calculated cured linewidth as a function of beam size and resin property. Line width and hatching space are calculated with [1]

$$L_w = B\sqrt{\frac{C_d}{2D_p}} \qquad 6.1$$

where B is the beam width (125 μm), C_d is the depth of photopolymerization through the surface, and D_p is the resin sensitivity or the distance at which the laser intensity is reduced by e^{-1}. This cured linewidth function shows that for a Gaussian laser scanned in a straight line across a photopolymer obeying the Beer-Lambert equation: The cured linewidth, L_w, is directly proportional to the laser spot diameter, B. The cured linewidth is also proportional to the square root of the ratio of the cure depth to the resin penetration depth (C_d/D_p). Given the B, C_d, and D_p at the laser power 40 mW in our

system, calculated linewidth cured on the fused silica based suspension and useful hatching space are 90 μm and 52 μm, respectively.

An experiment was designed in order to compare the effect of STaggered hatch type to the cracks of sintered body. The amount of residual monomer located on the inside of green body is changed by STaggered hatch type. As shown in Figure 6.9, cracks in the sintered body fabricated with hatching space ranging from 25 to 100 μm are represented by circles. If the residual monomer located on the STaggerd hatch is the main reason for generating the cracks in the sintered body, more cracks should be detected from the residual monomer in the larger hatch space. However, although sample with hatching space 40 μm has fewer cracks, vertical and horizontal cracks are found in the all samples with different hatching spaces. Therefore, the residual monomer located on the Staggered hatch is not the origin of cracks in the sintered body. There is another residual monomer in Figure 6.9. Since residual monomer shown in Figure 6.10 was added in the end contraction of 20 μm between border and fill vector near the surface, this monomer may affect the cracks of the sintered bodies shown in Figure 6.9.

6.4.2 Retracted hatch vs. Cracks

Previous results contained not only the effect of STaggered hatch, but were also coupled with the effects of the Retracted hatch. In order to separately analyze the effect of Retracted hatch on the crack, sintered bodies are prepared with the different hatch space from 25 to 100 μm and no retracted hatch. No retracted hatch means that the fill vectors are attached to the border lines on both ends to remove residual monomer near border line at the surface. Figure 6.11 shows the effect of no retracted hatch on the cracks

in the sintered body. With no end contraction in retraction hatch, vertical and horizontal cracks in the sintered body are removed.

The reason for this improvement is related to the retracted hatch of the resin system. One end of fill vectors in a layer was only attached to one of borders to relieve the internal stress, reducing any reactive forces to be exerted on the borders. However, the residual monomer marked as red circles in Figure 6.10 exists at retracted hatch between fill and border vectors and it may be the cause of cracks. It can be concluded that the internal stress is resulted from the residual monomer thermally polymerized during heating to ~ 200^{o}C. As shown in Figure 6.1 and 6.7, the vertical and horizontal macro cracks in the green and fired bodies are initiated by releasing the internal stress from the polymerization shrinkage of the residual monomer.

In order to examine the effect of uncured monomer on the cracks of fired bodies, the length of horizontal and vertical cracks located at the 4 side surfaces of each cube sample are measured, and then sum the lengths of the cracks. Relative crack length is obtained from the total crack length divided by 4 (number of side surfaces). Figure 6.12 shows the relative length of horizontal and vertical crack as a function of end contraction of 0 to 200 μm. In order to neglect the effect of STaggered hatch, all samples with hatch spacing of 50 μm are prepared so that the effect of end contraction is considered to be a main variable on the horizontal and vertical cracks. The horizontal and vertical crack does not have any trend on the relative crack length. However, note that relative total crack length is gradually increased as end contraction is getting larger. The amount of residual monomer increases with end contraction, and the volume contraction due to thermal polymerization of the monomer should increase with end contraction. This trend

means that the strain resulting from thermal polymerization of monomer causes the horizontal and vertical cracks.

The more uncured monomer left, the longer the total crack length. This result can be explained by the following reason. Uncured and residual monomers located near border vector are polymerized by the radicals generated by the thermal decomposition of the hydroxyketone photo-initiator during binder burn-out process. They undergo the volumetric change like shrinkage resulting from the density difference between the monomer and polymer. In contrast, for the case of zero end contraction in the Retracted hatch without uncured monomer, the fill vectors already polymerized by UV light are firmly connected with border vectors so that they are able to sustain its original shape during BBO. Hence, much less or no internal stress exists between shrinkage of uncured monomer and previous cured polymer of border vector, which creates no cracks at the surface of fired bodies.

6.4.3 Detection of residual monomer located in the retracted hatch

Through comparison between crack length and end contraction, we can conclude that residual monomer in the end contraction was polymerized by thermal decomposition of hydroxyketone photoinitiator during BBO, inducing the volume change and increasing the internal stress according to the amount of the residual monomer. The generated internal stress causes the horizontal and vertical cracks, gradually increasing the total crack length as the length of end contraction including residual monomer increases, as shown in Figure 6.12. Given the results, residual monomer may exist at the retracted hatch in the green body. Therefore, the step is necessary to know what materials exist at

the retracted hatch part of green body before BBO.

Materials can be detected using Gas chromatography/Mass spectrometry (GC/MS), which uses the difference in the chemical properties between different molecules in a mixture to separate the molecules.[8] For example, since each element has different molecule weight and shape, it travels through the column at different speeds so that the molecules take different amounts of time to come out of the gas chromatograph. This allows the mass spectrometer downstream to evaluate the molecules separately, which can be separated in the GC column and produce their ideal specific spectral peaks, while mass spectrometry as the identification technique has been used.

The compounds, extracted from a green sheet with end contraction of 200 μm or no end contraction, were investigated by GC/MS analysis. Figure 6.13 shows GC chromatogram corresponding to the compounds extracted from a green sheet with end contraction of 200 μm. Two distinctive peaks, #1 and #2, are detected at the retention time of each component is ideally detected at a specific spectral peak that was recorded electronically at the different retention time elapsed between injection and elution.

Figures, 6.14 and 6.15 show the results of mass spectrometry and Wiley NBS library for identifying peaks on two distinctive peaks of #1 and #2. Individual compounds, #1 and #2 eluted from the GC column enter the mass spectrometry, breaking apart into large or small fragments of the original molecules. Those fragments are represented as the signal intensity (relative abundance) for each of fragments in the y-axis and the mass to charge ratio (M/Z) in the x-axis, as shown in Figure 6.14 (a). Fragments of individual compounds, #1 and #2, are compared with the reference data in Wiley NBS library to indentify each compound. Figure 6.14 (b) shows the reference data of HDDA in Wiley

NBS library, the matching result between the reference data and fragments, and fragments of a compound #1. Given the result of peak identification, the peak of #1 and #2 are identified as the HDDA (monomer) and Irgacure 184 (photoinitiator), respectively. Those compounds detected from GC/MS analysis are supporting our hypothesis that cracks are initiated from the thermal polymerization of residual monomer and photoinitiator in the green sheet with end contraction of 200 μm during binder burn-out.

6.5 CONCLUSION

Ceramic stereolithography (CerSLA) builds ceramic green objects from CAD files from many thin liquid layers of powder in monomer. Layers are written according to a "build style" which controls X and Y directions of the UV laser. The purpose of the "build style" is to suppress macroscopic distortions resulting from the inevitable volume decreases when the monomers were polymerized. STaggered or Retracted hatch in the WEAVE style are used to reduce internal stress as filling the weaker region between layers or as disconnecting one of the ends of the hatch vector to the adjacent border, respectively.

Uncured photo-polymerization monomer located at the STaggered or Retracted hatch is polymerized by heat energy. In the CerSLA process, heat energy is applied during a binder burn-out process to remove polymer in the green body. In order to examine thermal polymerization of uncured monomer, differential scanning calorimetric (DSC) is used to detect the exothermic heat flow from the free-radical polymerization. The exothermic heat flow represents polymerization of monomer generated by the

thermal decomposition of the hydroxyketone photo-initiator around 190^{o}C.

Retracted hatch vector shows the significant effect on the crack that more uncured monomer initiates the longer total crack length. Vertical and horizontal cracks are generated from the volumetric change like shrinkage resulting from the density difference between the monomer. On the other hand, for the case of zero end contraction in the Retracted hatch without uncured monomer, the fill vectors already polymerized by UV light are firmly connected with border vectors so that they are able to sustain its original shape during BBO. In addition, uncured monomer and photoinitiator residing in the Retraction hatch are detected by GC/MS. Those results obtained from GC/MS analysis indicates that cracks are initiated from the thermal polymerization of residual monomer and photoinitiator in the end contraction hatch.

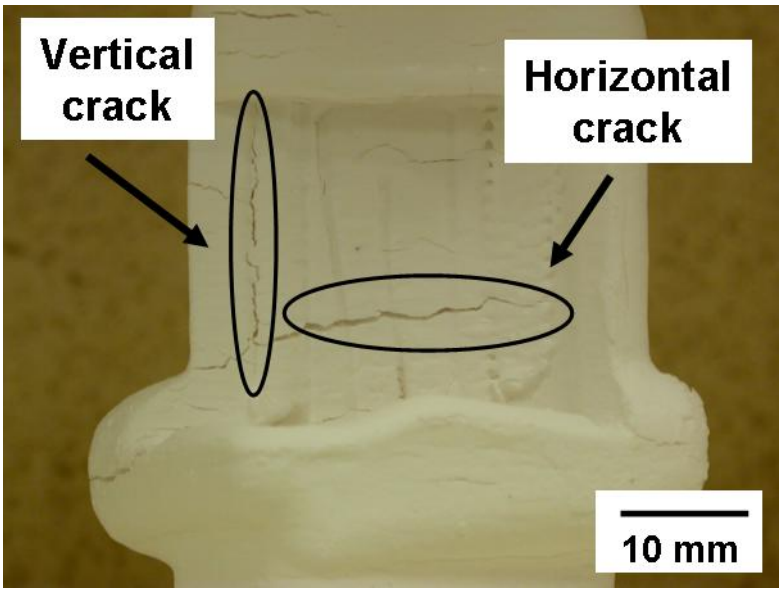

Figure 6. 1 Vertical and horizontal cracks of ICCM sintered mold

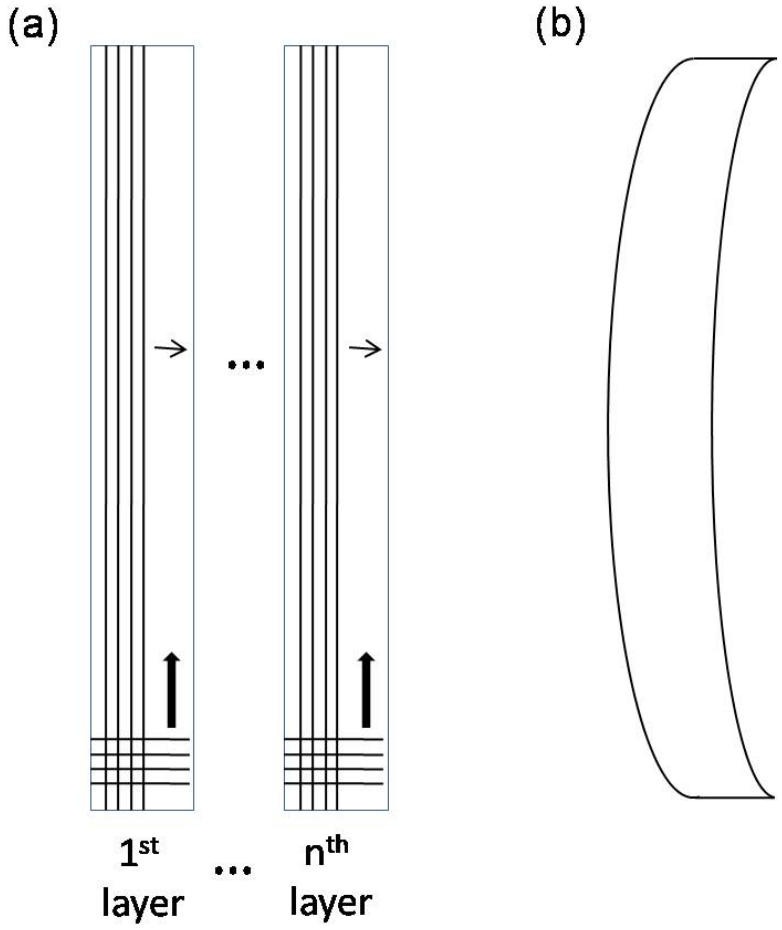

Figure 6. 2 Short vectors drawn using the WEAVE style. (a) cross-sectional view of each layer and (b) a distorted thin vertical wall attributed to the net result of subsequent shrinkage at the regions which largely attached to the lower layer and the border lines.

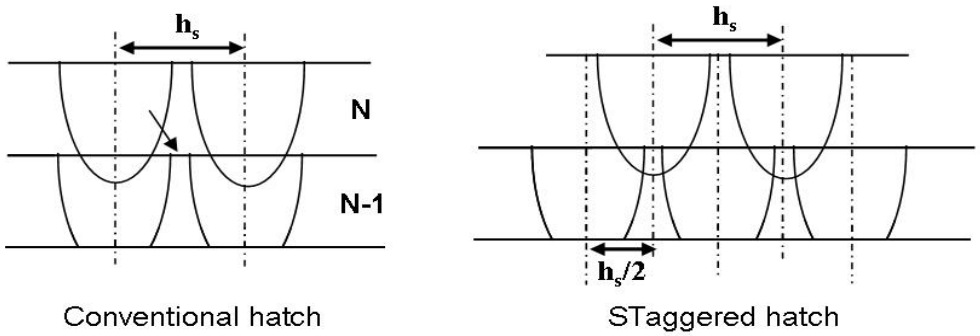

Figure 6. 3 STaggered hatch build type to reduce internal stress

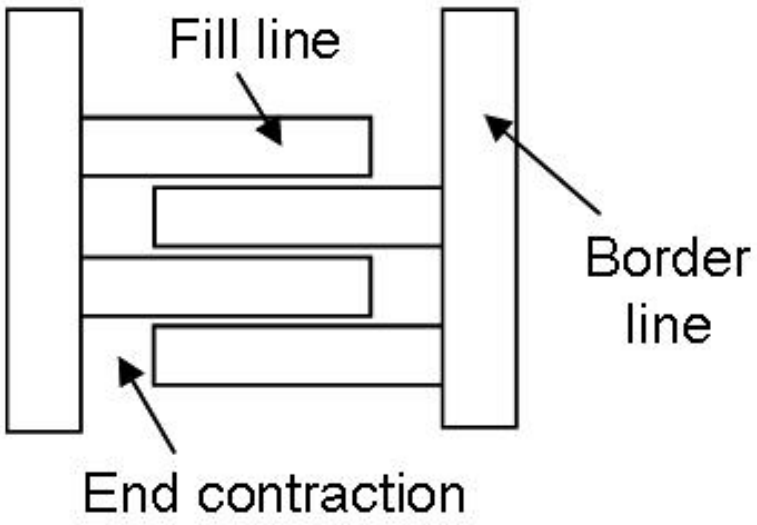

Figure 6. 4 Retracted hatch to reduce internal stress

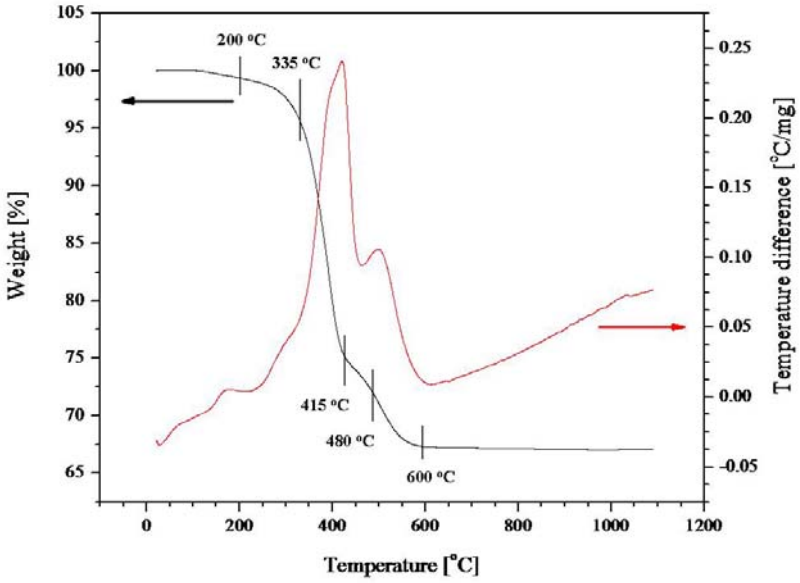

Figure 6. 5 Thermogravimetric analysis (TGA) used to identify temperature regions of rapid mass loss

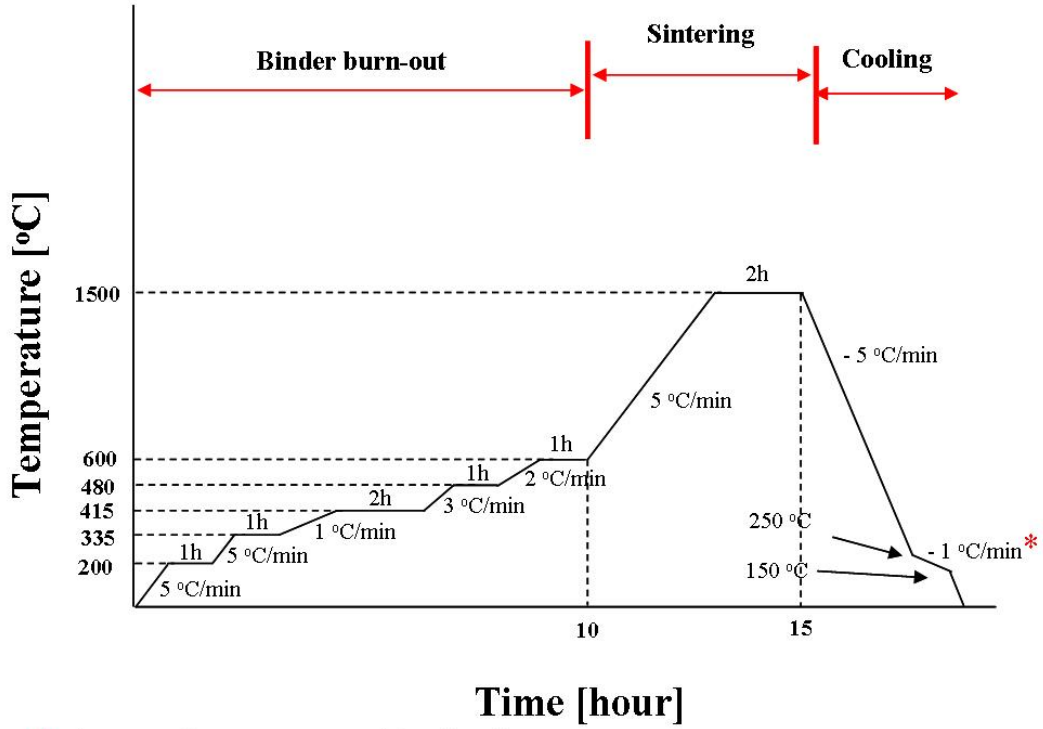

Figure 6. 6 Thermal conditions for organic product removal and sintering of green body

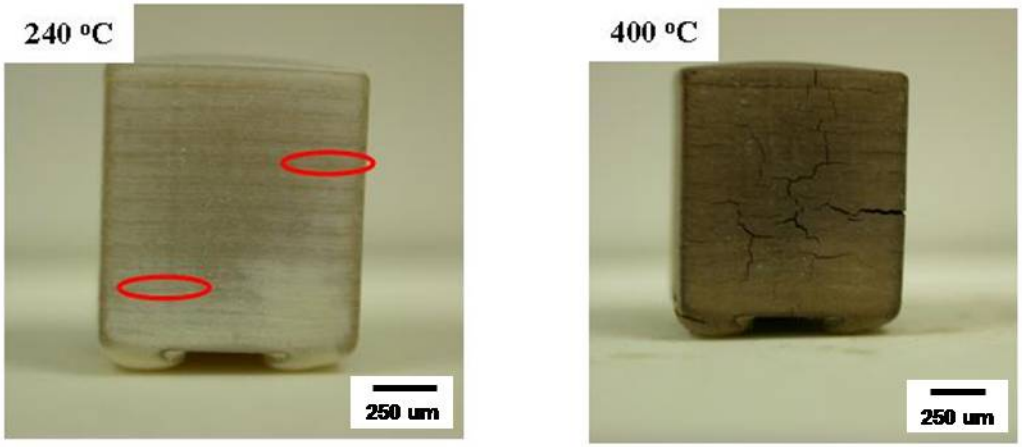

Figure 6. 7 Vertical and horizontal cracks detected in the green body during binder burn-out

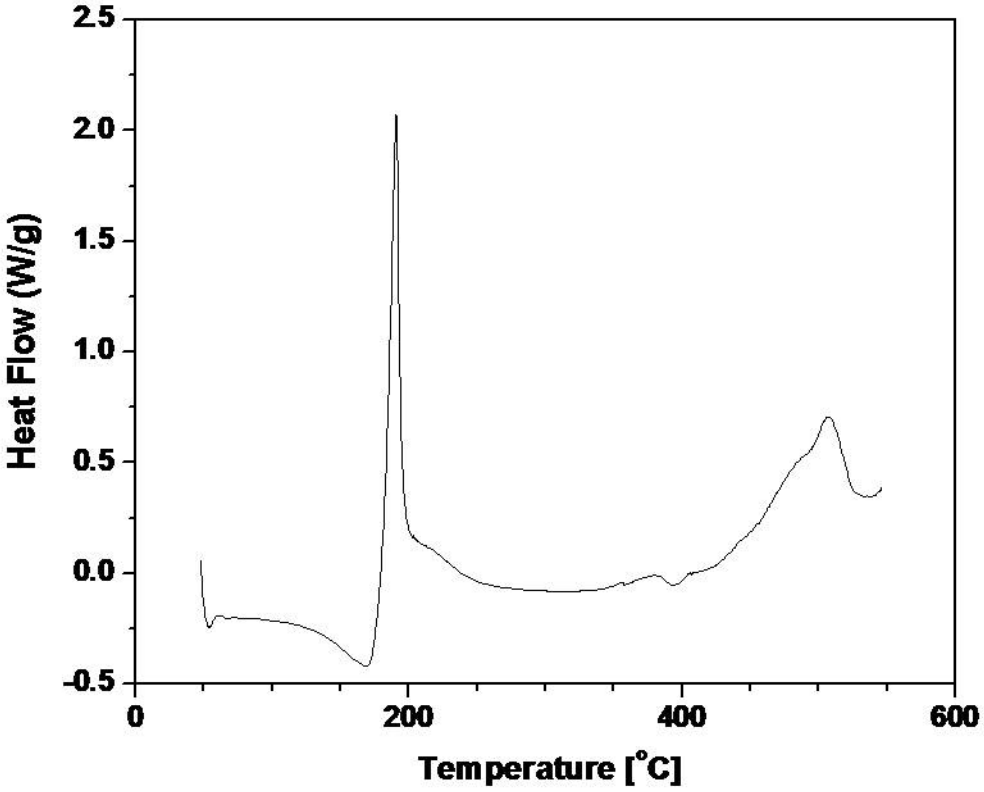

Figure 6. 8 Heat flow as a function of temperature measured by DSC. Exothermic heat flow around 200°C represents thermal polymerization induced by thermal decomposition of photoinitiator.

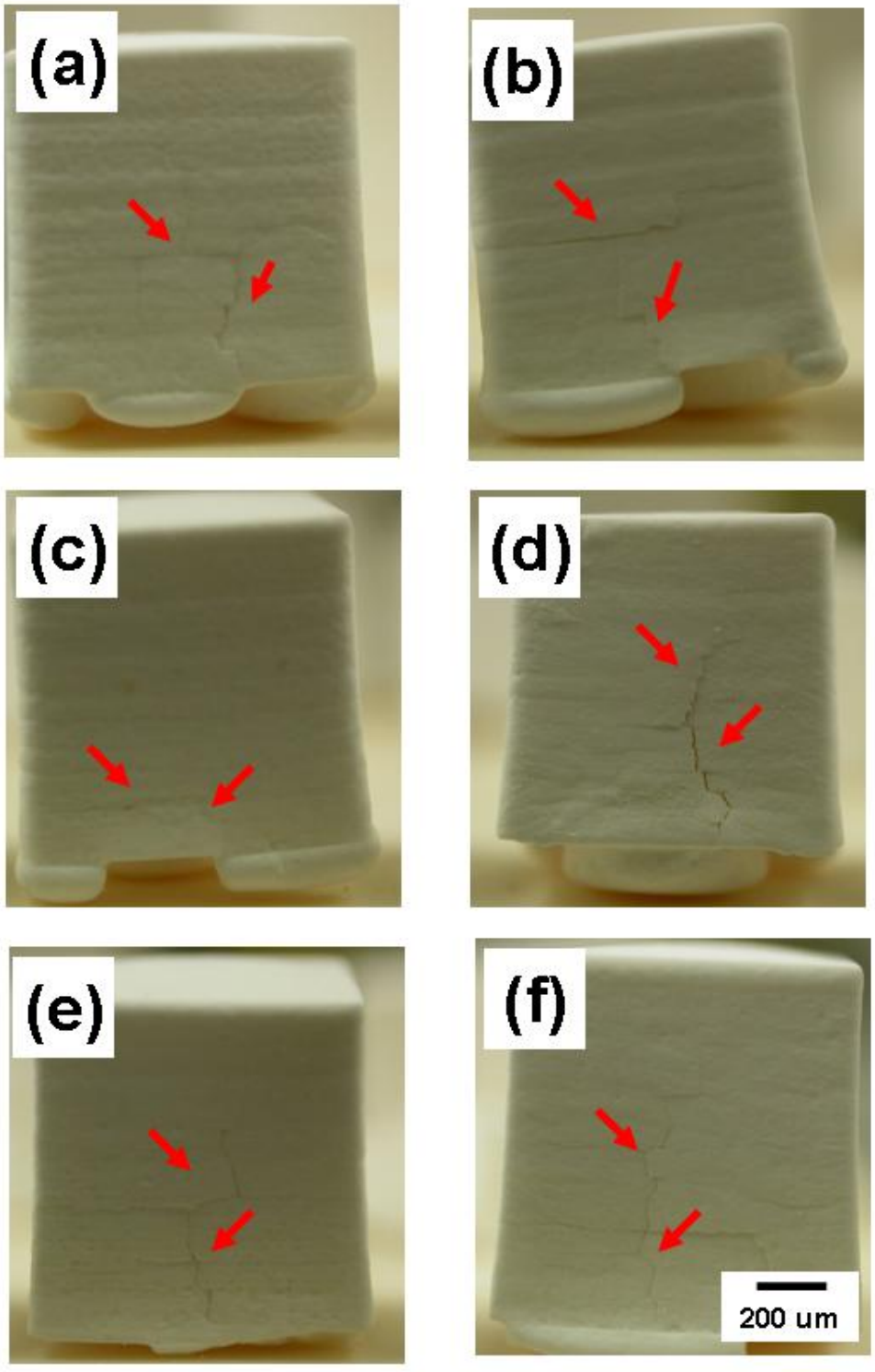

Figure 6. 9 Cracks generated in the whole regions of hatching space (h_s); (a) h_s = 25 μm, (b) h_s = 30 μm, (c) h_s = 40 μm, (d) h_s = 50 μm, (e) h_s = 80 μm, and (f) h_s = 100 μm.

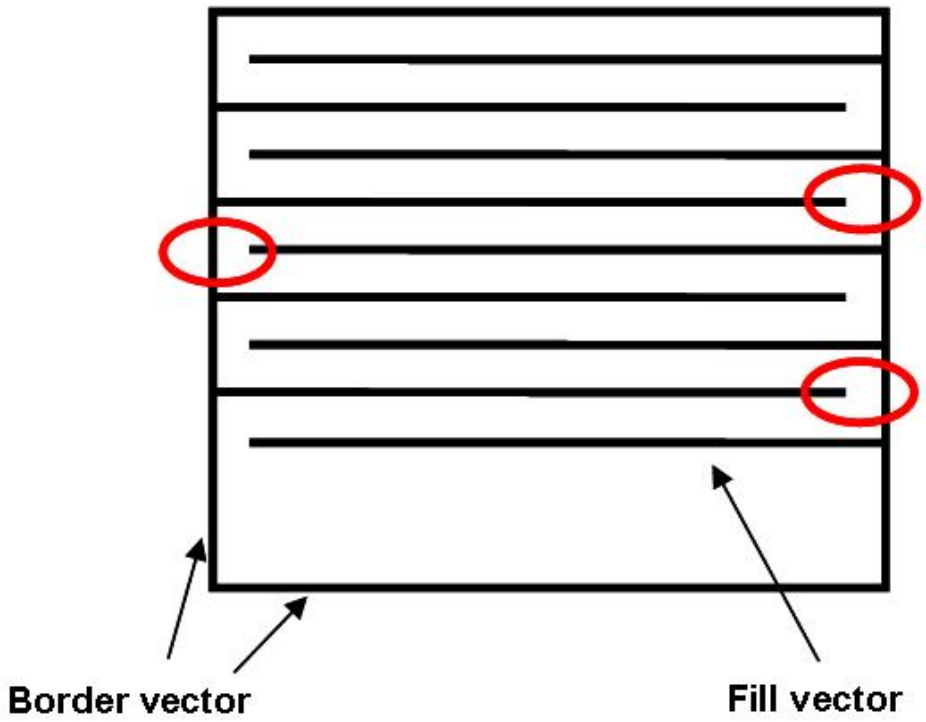

Figure 6. 10 Residual monomer resulted from Retracted hatch near border vector

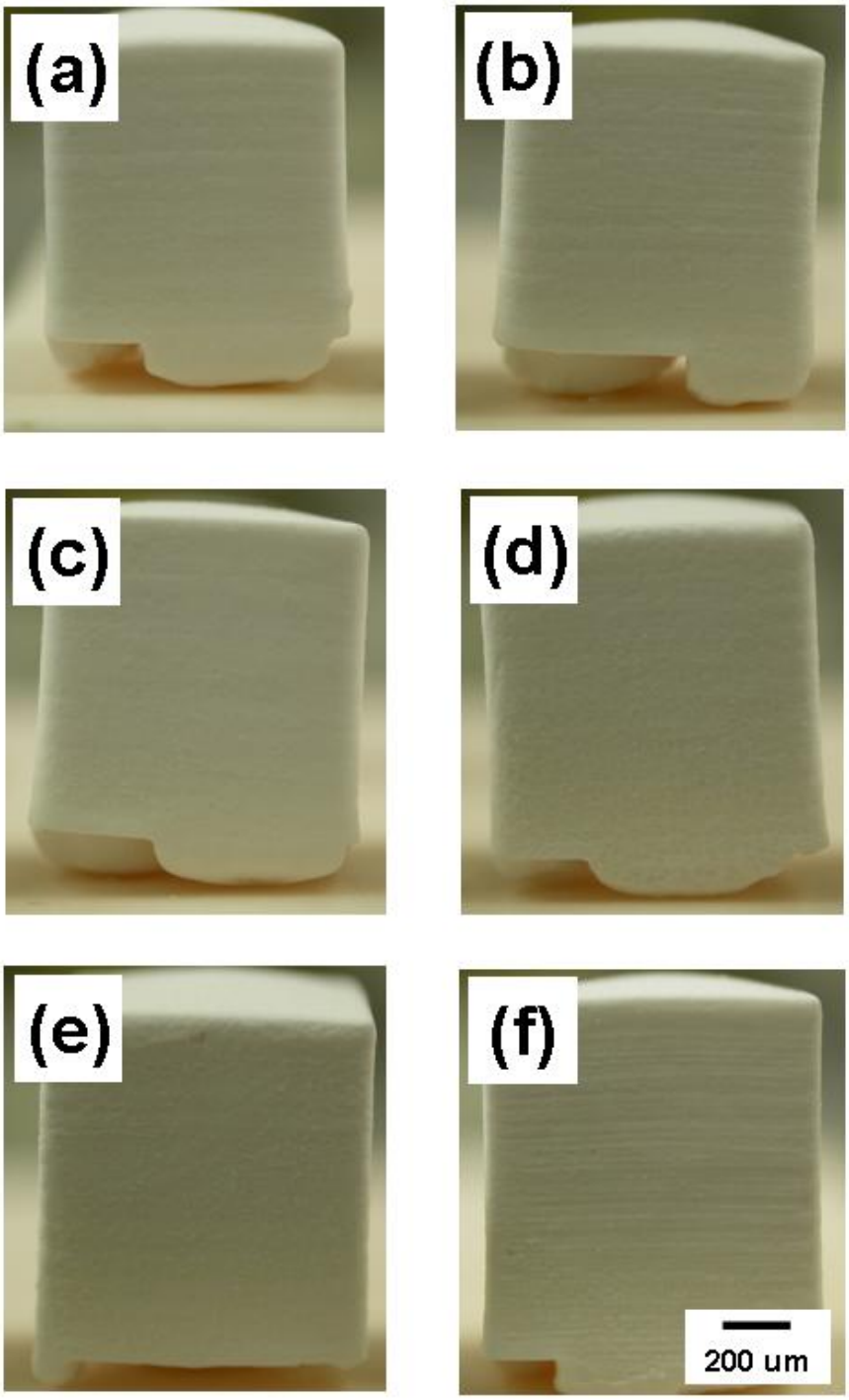

Figure 6. 11 No cracks resulting from no residual monomer near surface); (a) h_s = 25 μm, (b) h_s = 30 μm, (c) h_s = 40 μm, (d) h_s = 50 μm, (e) h_s = 80 μm, and (f) h_s = 100 μm.

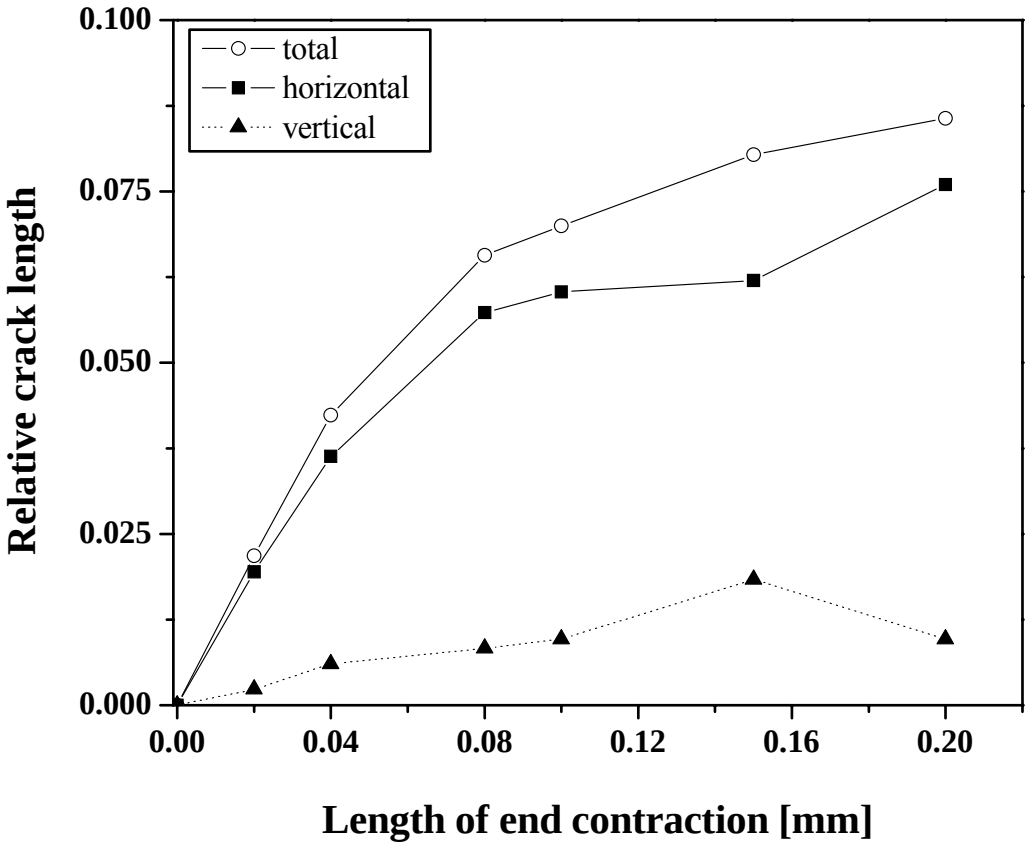

Figure 6. 12 Relative crack length as a function of retracted hatch style

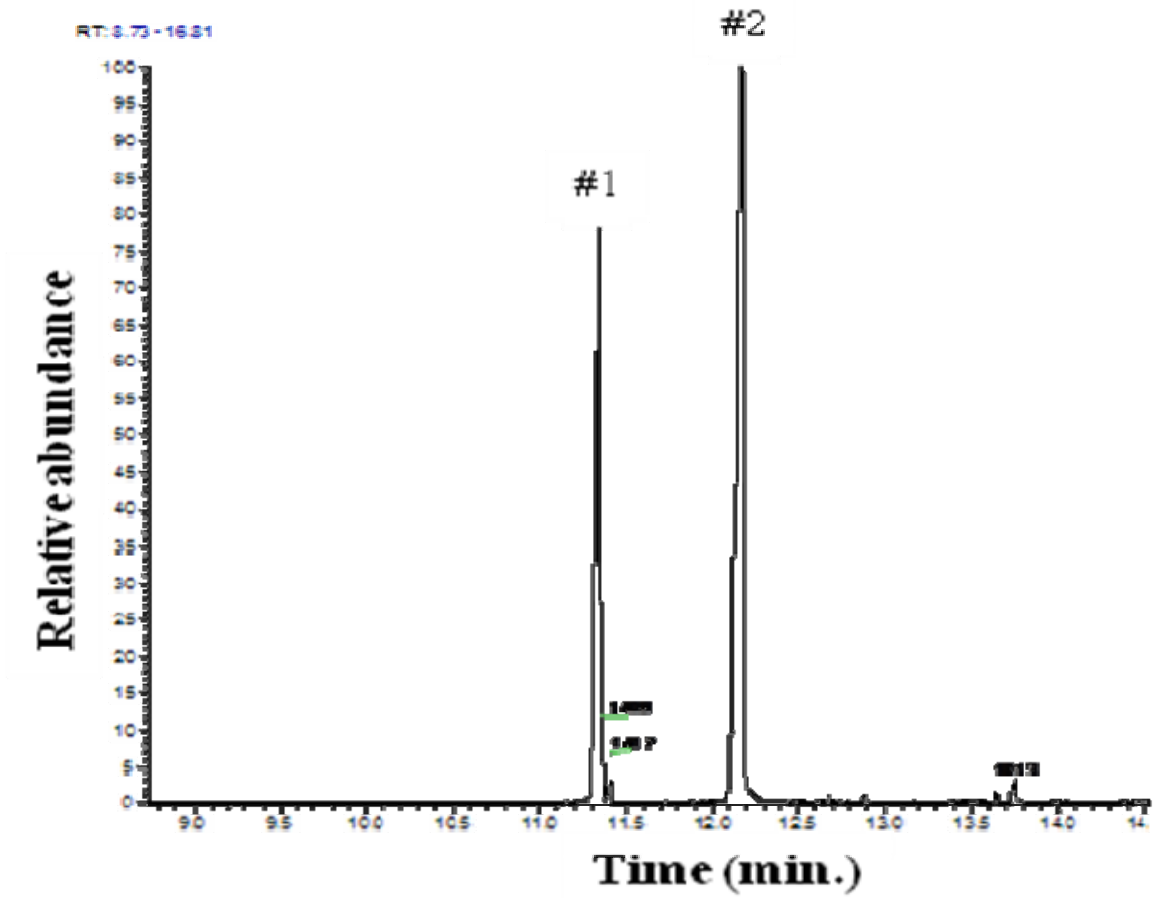

Figure 6. 13 GC/MS chromatogram of HDDA (#1) and photoinitiator (#2) extracted from a green sheet with end contraction of 200 μm.

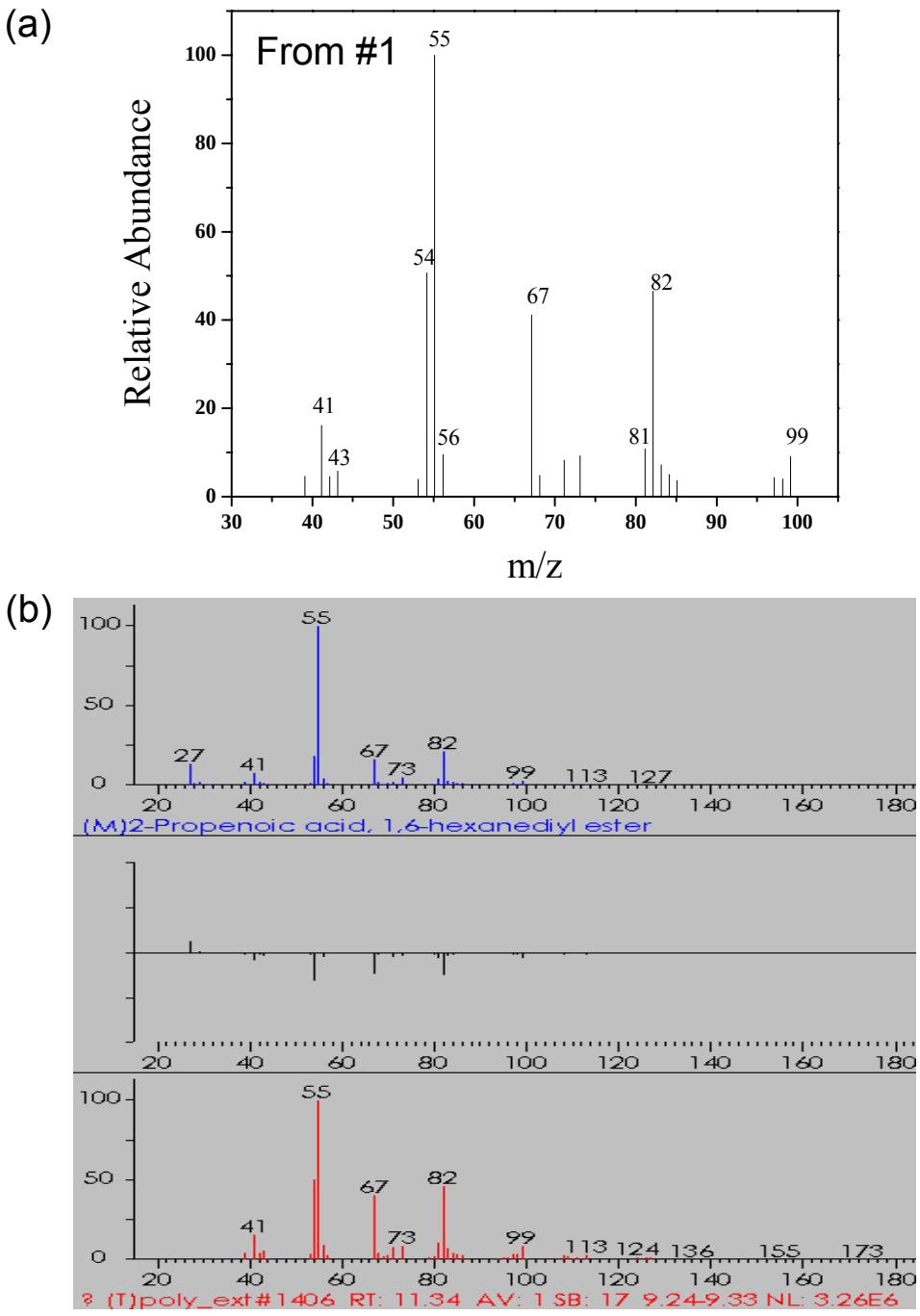

Figure 6. 14 Peak identification of a component (#1) detected using GC; (a) Mass to charge ratio analyzed using MS and (b) Matching a component (#1) with a reference data in Wiley NBS library. HDDA (residual monomer) as a component (#1) is identified using MS and Wiley NBS library.

(a)

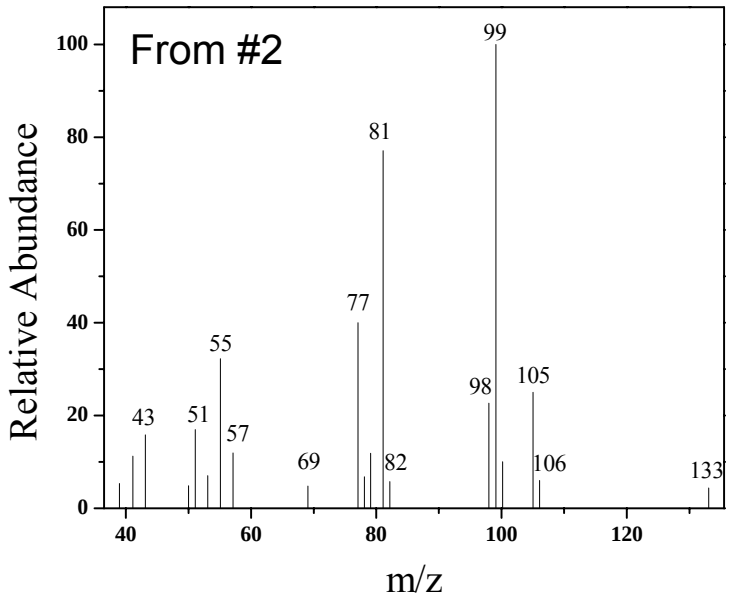

(b)

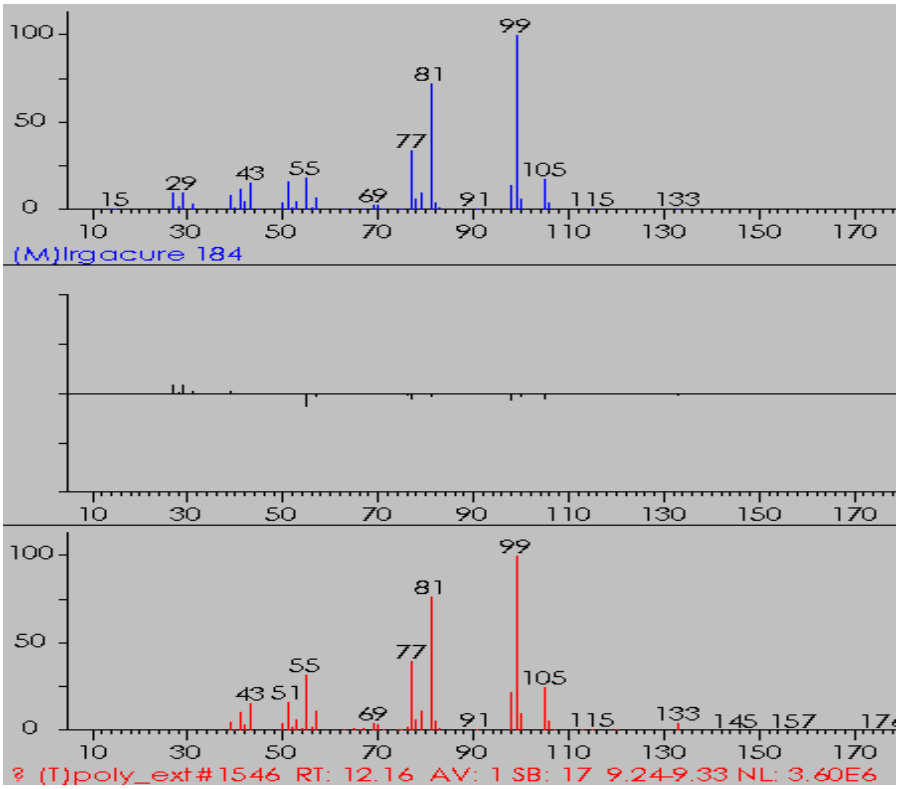

Figure 6. 15 Peak identification of a component (#2) detected using GC; (a) Mass to charge ratio analyzed using MS and (b) Matching fragments of a component (#2) with a reference data in Wiley NBS library. Irgacure 184 (photoinitiator) as a component (#1) is identified using MS and Wiley NBS library.

Reference

1. P.F. Jacobs, *Rapid Prototyping & Manufacturing– Fundamentals of Stereolithography*, SME, La Crescenta, California, 397, 1992.
2. S.O. Onuh and K.K.B. Hon, "Application of the taguchi method and new hatch styles for quality improvement in stereolithography", *Proceedings of the Institution of Mechanical Engineers*, **212**, 461-71, 1998.
3. S.O. Onuh and K.K.B. Hon, "Integration of rapid prototyping technology into FMS for agile manufacturing", *Integrated Manufacturing Systems*, **12** [3], 179-86, 2001.
4. A.M. Knapp and J.W. Halloran, "Binder removal from ceramic-filled thermoplastic blends", *J. Am. Ceram. Soc*., **89** [9], 2776-81, 2006.
5. A.J. Leadbetter and A.F. Wright, "The α-β transition in the cristobalite phases of SiO2 and AlPO4: I. X-ray studies", *Philosophical magazine*, **33** [1], 105-12, 1976.
6. G.A. Brady and J.W. Halloran, "Differential photo-calorimetry of photopolymerizable ceramic suspension", *J. Mater. Sci.*, **33**, 4551-60 (1998).
7. G. Odian, "Principles of polymerization", John wiley & Sons, Inc., New York, 1991.
8. B.A. Howell, "The utilization of TG/GC/MS in the establishment of the mechanism of poly (styrene) degradation", *J. Therm. Anal. Cal.*, **89** [2], 393-98 (2007).

CHAPTER 7

SINTERING AND CRISTOBALITE TRANSFORMATION IN FUSED SILICA COMPACTS

This chapter covers the sintering of fused silica compact and the transformation to cristobalite for refractory grade silica powders. The goal is to investigate the transformation kinetics of fused silica studied by quantitative X-ray diffraction (QXRD) and choose the optimal thermal condition for controlling the cristobalite transformation in fused silica compact during sintering. Given the transformation kinetics of fused silica, the amount of cristobalite in the integrally cored ceramic casting mold (ICCM) can be controlled, thus able to fabricate the ceramic molds with sufficient mechanical properties to avoid ceramic mold failure resulting from the cast metal.

7.1 INTRODUCTION

A fused silica based integrally cored ceramic mold (ICCM), the ceramic core with a ceramic mold shell in a single patternless construction shown in Chapter 5, is fabricated by ceramic stereolithography (CerSLA). The ICCM is designed to directly cast a turbine airfoil with complex hollow interior passages that are used to conduct cooling air through one or more passageways. To produce ceramic cores for the hollow cooling passages in a turbine airfoil, the selection of refractory ceramics is crucial since the quality and accuracy of the cast part is dependent on the ceramic core material.

Refractory ceramics, the material capable of making internal hollow cavity of turbine airfoil, should satisfy the following restrictions: similar strength to that of cast metal during solidification, thermal stability for dimensional accuracy, and easy removal of core after casting. If the ceramic is much stronger than the cast metal, hot cracking of the metal occurs due to the larger thermal contraction of the metal during cooling. On the other hand, if the ceramic is too weak, the mold will fail from the weight of the hot cast metal. The refractory ceramic must have excellent thermal stability to prevent creep and dimensional change resulting from the secondary sintering due to high casting temperature as high as 1600^{o}C.

Among the refractory ceramics, fused silica is the material extensively used for ceramic cores to produce complex, internal cooling passage in investment-cast, superalloy turbine airfoils.[1] Fused silica is the best candidate for non-reactive alloys fulfilling the restrictions on refractory ceramics used for investment casting such that it has thermal stability at high temperature resulting from a low thermal expansion

coefficient (about $0.6x10^{-6}/^{o}C$) and excellent thermal shock resistance. In addition, a fused silica core is easily removed due to the complete chemical leachability in aqueous solutions such as NaOH and KOH, where the solutions are non-deleterious to the nickel-base superalloys.[2]

Given the various advantages of fused silica, the sintering of a fused silica compact and the transformation to cristobalite should be considered. During the sintering of fused silica molds, cristobalite transformed from the fused silica provides stiffness for the fused silica molds.[3] The silica mold, being composed of a glassy material, starts to soften and will be susceptible to bow or twist if the differential expansion forces are imposed on the system. This problem is improved by using a modified composition such as 90% silica glass and 10% crystalline cristobalite. However, if an excessive amount of cristobalite exists in fused silica molds, abrupt contraction induced from beta- to alpha-cristobalite at $\approx 200^{o}C$ on cooling leads to extensive cracking, thus decreasing the strength.[4] Therefore, it is necessary to investigate the reaction kinetics and phase transformation mechanism of cristobalite.

The purpose of this study is to investigate the transformation kinetics of fused silica studied by quantitative X-ray diffraction (QXRD) and choose the optimal thermal condition for controlling the cristobalite transformation in fused silica compact during sintering. The relation between transformation and microstructure after sintering is reported, and related to the physical properties of silica investment casting molds and cores. Given the transformation kinetics of fused silica, the amount of cristobalite in the ICCM can be controlled, thus able to fabricate the ceramic molds with sufficient mechanical properties to avoid ceramic mold failure resulting from the cast metal.

7.2 BACKGOURND ON VISCOUS FLOW SINTEIRNG AND CRYSTALLIZATION OF FUSED SILICA

7.2.1 Viscous flow sintering of fused silica powder

Sintering is the term used to describe the consolidation of the product during firing, which reduces the surface area of the powder particles. The driving force of sintering arises from the excess free energy of the surface of the powder over that of the solid material.[5] The fundamental research of sintering is to explain the main mechanism inducing the reduction of energy. Mechanisms for mass transport during sintering are divided by four types: surface diffusion, evaporation-condensation, volume diffusion, and viscous flow. [5,6]

Surface diffusion is a general transport mechanism that can produce surface smoothing, particle joining, and pore rounding. In the case of evaporation-condensation mechanism, there is a positive radius of curvature where the vapor pressure is relatively high. Sublimation and vapor transport to surfaces of lower vapor pressure also produce these effects. Volume diffusion along the grain boundaries and through the lattice of the grains produces both neck growth and volume shrinkage. The mechanisms of bulk viscous flow may be effective when a wetting liquid is present and when a mechanical pressure is applied, respectively. Among the mechanisms, surface diffusion and evaporation/condensation do not produce densification, but diffusions along the grain boundaries and through the lattice of grains and viscous flow in amorphous materials produce densification in the course of reducing surface area. [7]

In this thesis, since fused silica powders (amorphous or glass powders) are only

used to fabricate an ICCM, viscous flow sintering in amorphous materials are mainly presented. In the sintering of glass powders, it can be shown that densification by viscosity flow is faster than densification by diffusion. Given the sintering stages, two models, Frenkel model and the Mackenzie-Shuttleworth (M-S) analysis, have been developed to account for the sintering of glasses. Frenkel's model of viscous sintering, which describes the early stages of sintering of spherical, monodispersed particles, allows one to calculate the shrinkage rate of two equal particles whose centers approximate each other. Mackenzie and Shuttleworth developed a model to explain the final sintering steps of a matrix with spherical monodispersed pores.

In the initial stage, viscous flow produced by the driving force of surface tension causes neck growth. For two glass spheres of uniform diameter, the initial shrinkage $\Delta L/L_0$ is given by the classic Frenkel equation[8]

$$\frac{\Delta L}{L_0} = \frac{3\gamma_s t}{2\eta r} \qquad 7.1$$

where t is the isothermal sintering time, γ_s surface tension, η viscosity, and r the radius of the uniform spherical particles. Equation 7.1 demonstrates that the initial rate of shrinkage is directly proportional to the surface tension, inversely proportional to the viscosity, and inversely proportional to the particle size. This description assumes that the void space between particles forms a continuous pore structure during the initial stages of sintering.

In the final stage or near the end of the sintering process, isolated pores should be represented as small spherical pores. A negative pressure equal to 2γ/r exists at the interior of each pore. This is equivalent to an equal positive pressure on the exterior of the compact tending to consolidate it. Mackenzie - Shuttleworth have derived a relation from the behavior for sintering of a viscous body containing dispersed isolated pores. The Mackenzie-Shuttleworth equation can be written as[9]

$$\frac{dD}{dt} = \frac{K\gamma_s n^{1/3}(1-D)^{2/3}(D)^{1/3}}{\eta} \qquad 7.2$$

where K is a constant that depends on geometry, γ_s surface tension, n the number of pores per unit volume of bulk material, D the relative density (bulk density/ glass density), and η viscosity. Equation 7.2 represents the densification rate dD/dt of uniform spherical pores dispersed in an isotropic, incompressible viscous medium. In the final stage, gas solubility and its diffusion in the glass and pore coalescence decrease the number of pores n, thus affecting the final pore shrinkage. Although finer pores have a larger driving force for shrinkage, the driving force is reduced by an increase in the gas pressure due to an increase in temperature or from gas evolved from within the glass, or pore coalescence.

7.2.2 Devitrification of fused silica

In the sintering of silica powder compact, less surface energy at the surface areas reduced by viscous flow plays a role of the driving force to enhance the densification. In

some cases of vitreous systems, however, surface crystallization occurs as a concurrent process of the sintering. The crystalline phases do not undergo as much shrinkage due to the viscous flow of vitreous silica, thus preventing the sintering induced by viscous flow.[1]

Crystallization or "devitrification" of glass can lead to different glass properties such as viscosity and coefficient of thermal expansion, and serious problems such that high stresses resulting from nonuniform contraction on cooling can cause fracture of the piece.[10] In the application of an optical fiber, additionally, crystals in a glass affect the transmission capability. The optical properties of a glass are changed due to the light scattered by the crystals such that this scattering degrade transparency in an optical fiber for long distance transmission.

Experimental and theoretical studies on the crystallization of glass have been focused on predicting crystallization rates in new compositions, and also defining the limiting times and temperatures to which a glass piece can be subjected.

7.2.3 Nucleation & growth of cristobalite in the fused silica

In order to predict and control the crystallization of fused silica compact, the mechanism of nucleation and growth of cristobalite in the fused silica compact powder are reviewed. Crystals usually form in glass by a nucleation and growth mechanism: a small region of the equilibrium crystal composition forms by nucleation and then grows. Nucleation involves the formation of numerous small particles, or nuclei of the new phase (often having size of only a few hundred atoms), which are capable of growing.

The formation of a stable nucleus is expressed by a thermodynamic parameter

called Gibbs free energy, G. Gibbs free energy is a function of the internal energy of the system (i.e., the enthalpy, H) and a measurement of the randomness or disorder of the atoms or molecules (i.e. entropy, S). When ΔG has a negative value, a transformation will occur spontaneously. According to the site where nucleating events occur, there are two types of nucleation: homogeneous and heterogeneous.

In the homogenous nucleation, nuclei of the new phase form uniformly throughout the parent phase. In the heterogeneous nucleation, on the other hand, nuclei form preferentially at structural inhomogeneities, such as container surfaces, insoluble impurities, grain boundaries, dislocations, and so on. In glasses, since it is difficult to remove structural inhomogeneities, crystallization is initiated from heterogeneous nucleation not homogeneous nucleation.[11] A general equation for the rate of steady-state nucleation (I) in condensed systems has the following form:

$$I = \frac{A}{\eta}\exp\left(\frac{-\Delta G^*}{kT}\right) \qquad 7.3$$

where A represents a jump frequency and is relatively weakly temperature dependent, k is the Boltzmann constant, T is temperature (K), η is dynamic viscosity, and ΔG^* is the thermodynamic energy barrier to form a nucleus of the critical size in the heterogeneous kinetics, such that

$$\Delta G^* = \frac{16\pi V_m^2}{3\Delta G_c^2}\sigma_\infty^3 (2 - 3\cos\theta + \cos^3\theta)/4 \qquad 7.4$$

where V_m is molar volume of the melt, ΔG_c is the bulk free energy change for crystallization, σ_∞ is the surface free energy between the crystal and liquid in the absence of a heterogeneity (surface), and θ is the contact angle between crystal and heterogeneity. In the equations 7.3 and 7.4, given the extreme dependence of the nucleation rate on the surface free energy, small changes of surface free energy (σ) result in large changes in the nucleation rate (I). Zanotto showed that a 30% decrease in σ results in a 100 increase in the nucleation rate using parameter values for lithium disilicate.[12]

Once a stable nucleus has been formed, crystal growth propagates from certain centers by the addition of atoms or molecules to the nucleus at a rate which is determined by the reaction of crystal-liquid interfaces. The rate of growth of a crystalline phase from a glass has been studied by many investigators. According to Turnbull, the rate of propagation of the interface between the crystalline and amorphous (i.e, liquid or glass) state of a pure substance is obtained[13]

$$u = \frac{fD_u}{a}[1 - \exp(\Delta g / kT)] \qquad 7.5$$

where f is fraction of sites in the interface to which molecules can be attached, D_u is the kinetic constant (in units of distance^2/time) for the process, a is the molecular displacement, and Δg is the molecular free energy change.

7.3 EXPERIMENTAL PROCEDURE

Fused silica (SiO_2, Alfa Aesar Chemicals, Ward Hill, MA) shown in Figure 7.1 (a) was fired at 1550^{o}C for 10 hours to produce cristobalite powder. Devitrification generally occurred on the surface of the silica grains and grinding is done to expose the unconverted fused silica, prior to refiring. Ground powders were heated at 1550^{o}C for another 10 h, and then a second grinding was done to produce cristobalite with relatively high purity. Figure 7.1 (b) shows the SEM micrographs of transformed cristobalite. Thermal facets representing crystal not amorphous are detected in the transformed cristobalite.

The reference data was gathered by taking XRDs (X-ray Diffraction Pattern) of pure 0.2 grams of cristobalite with the addition of 0.05g grams of calcium fluorite. The fluorite (CaF2) as a standard sample is used to plot a calibration curve. Then, the intensity ratio between cristobalite and calcium fluorite (CaF2) was plotted as a function of weight percentages of cristobalite to make a calibration curve. Figure 7.2 shows two strong peaks, 80% of cristobalite ($2\theta = 21.95^{o}$) and fluorite ($2\theta = 28.26^{o}$), determined by X-ray diffraction and it is found that α-cristobalite and fluorite. Each sample was crushed and was put on the glass holder. Each sample was placed on the sample stage face up in the goinimeter part of the Rigaku MiniFlex. The diffractions were done a scan speed of $2\theta = 1^{o}$/min over a wide 2θ range of 20-29 degrees.

Ceramic test bars with dimension (8 mm height x 8 mm width x 83 mm length) for a three-point bending test were built by CerSLA. The ceramic suspension in the CerSLA was prepared from the mixture of fused silica powder; 25 weight percent of

coarse (d_{50}: 27 μm) and 75 weight percent of fine (d_{50}: 7μm). A quaternary amine dispersant (CC-59, Goldschmidt,) in an amount equal to 3% of the weight of the SiO_2 powder was added to lower the viscosity and aid in ceramic dispersion. The photopolymerizable monomer and monomer mixture were prepared using 1,6-hexanediol diacrylate (HDDA, SR238) as received from Sartomer company (Exton, PA). 1-Hydroxy cyclohexyl phenyl ketone (Irgacure 184, Ciba Specialty Chemicals, Tarrytown, NY) used as a photoinitiator decomposed on UV- radiation, releasing free radicals, which initiated the polymerization reaction of monomer mixtures. SiO2 powder and CC-59 as a dispersant for stable colloidal dispersion were added to UV-curable monomer mixtures without photoinitiator to prepare the ceramic suspensions. Green bodies of test bars were produced in a commercial stereolithography apparatus (SLA-250, 3D Systems, Inc. Valencia CA), by dipping a substrate into a reservoir of well-stirred suspension to make 100 micron thick liquid layers. After a delay time of either 40 seconds, the layer was solidified within 4 seconds by scanning the surface in a raster pattern at 1369 mm/sec with a UV laser beam focused in a 120 diameter spot size. The UV radiation was provided by using diode-pumped solid state lasers in quasi-CW 355 nm air-cooled format (Xcyte, JDS Uniphase, Milpitas, CA).

Given the thermal schedule listed in Table 7.1, green bodies of test bars were processed by binder burn-out to remove cured polymer, and then test bars were heated at 10^{o}C/min to temperature between 1200^{o}C and 1500^{o}C, held for 2 hours, and then cooled at 10^{o}C/min to room temperature before being subjected to a three-point bending test. The three-point bending tests of the sintered test bars were conducted using a universal materials testing machine (Instron 4502, Instron Corp., Norwood, MA) with a crosshead

speed of 1.27 mm/min and a 10 kN load cell. The flexural strength of the samples was monitored with software (Testworks 4, MTS system Corp., Eden Prairie, MN). Three specimens of each material were tested to obtain an average flexural strength along with its standard deviation.

The various images were taken to analyze how the temperature and time affect the amount of cristobalite formation in fine powder. Optical images of the green and sintered bodies were taken by an OVM1000NM (Olympus) microscope. SEM images were obtained by a FEI Philips XL 30 Scanning Electron Microscope (FEI Co., OR, USA) with samples sputtered with gold for 3 min (SPI Sputter Coater, SPI Supplies, PA, USA) prior to imaging.

7.4 CRISTOBALITE VS. FLEXULAR STRENGTH

7.4.1 Quantitative X-ray analysis for weight fraction of cristobalite

In internal standard method, a diffraction line from the phase being determined is compared with a line from a standard substance mixed with the sample in known proportions. The relationship between the intensity of the phase and the standard and weight fraction of the phase is[14]

$$\frac{I_A}{I_S} = Kw_A \qquad 7.6$$

where K is a constant, I_A the intensity of the phase A, I_S the intensity of the

standard S, and w_A the weight fraction of A. Therefore, the intensity ratio of a line from phase A and a line from the standard S is a linear function of w_A, the weight fraction of A in the original samples. A calibration curve can be prepared from measurements on a set of synthetic samples, containing known concentrations of A and a constant concentration of a suitable standard. Once the calibration curve is established, the concentration of A in an unknown sample is obtained simply by measuring the ratio I_A/I_S for a composite sample containing the unknown and the same proportion of standard as was used in the calibration.

A calibration curve using internal standard method was prepared in order to measure the amount of transformed cristobalite in the fused silica powder. Mixtures of cristobalite and fused silica, of known composition, were mixed with enough fluorite to make the weight fraction of fluorite in each composite sample enough to 0.20. Figure 7.3 shows a calibration curve plotted from the intensity ratio of a line from cristobalite and a line from the fluorite (CaF2) vs. weight percent of cristobalite. The curve is linear and through the origin, as predicted by Equation 7.6.

Given the calibration curve of cristobalite, the amount of transformed cristobalite in the bars for flexural strength test is measured from the crushed powder. Figure 7.4 shows a result of quantitative X-ray diffraction data for weight percent of cristobalite in isothermally sintered test bar. It indicates that the amount of transformed cristobalite in the test bar sintered for 2 hours increased with increasing sintering temperature. The formation of cristobalite should be controlled, since the cristobalite in fused silica plays important roles such as increase of stiffness and decrease of mechanical property. Generally, casting industries are using ceramic molds with the amount of cristobalite of

less than 10%. Among the parameters relating to the generation of cristobalite, the holding time significantly affects the amount of transformed cristobalite. When holding time of test bars sintered at the same temperature of 1300^{o}C were changed from 2 hours to 30 minutes, there was much less formation of cristobalite during sintering from 27.6 to 8.3 %.

7.4.2 Flexural strength of fused silica test bar vs. Phase transformation of cristobalite

The flexural strength of test bars sintered at different temperatures from 1200^{o}C to 1500^{o}C is measured, as shown in Figure 7.5. Red lines indicate the optimum ranges in the flexural strength between 10 and 15 MPa required for the ceramic mold. Test bar samples sintered at 1250^{o}C and 1300^{o}C for 2 hours have the proper flexural strength of 10.6 and 11.8 MPa. In addition, a different sample heated at 1300^{o}C with a holding time of 30 minutes has the proper flexural strength of 10.2 MPa. The flexural strength of test bars increased with increasing sintering temperature. However, the flexural strength decreased to 4.6 MPa with the higher sintering temperature of 1500^{o}C. Figure 7.6 shows the flexural strength of test bars and the corresponding amount of cristobalite plotted as a function of sintering temperature. The flexural strength increased with increasing contents of transformed cristobalite up to 27.6%, yet it declined with more than the cristobalite formation of 30%.

The flexural strength was directly dependent on the amount of cristobalite, which is correlated with the transformation of cristobalite. When cristobalite was heated to temperature between 200^{o}C and 275^{o}C, the tetragonal alpha- or low-cristobalite transforms to the cubic beta- or high-cristobalite. Figure 7.7 shows the unit cell

dimensions of cristobalite calculated by Wright et al. [15] The actual transition temperature is dependent upon the degree of crystallinity of the specimen: well-crystallized material transforms at the highest temperatures; material which is poorly crystallized has lower transition temperatures. The transition shows marked hysteresis; the beta → alpha transformation occurs on cooling at a temperature about 35°C lower than the alpha → beta warming transition. With the lattice parameter measurements, the amount of contraction observed during cooling through the beta- to alpha- cristobalite transformation was considerably less than the 1.34% contraction and induced a specific volume change of ~5 vol% for cristobalite, thus generating microcracks. The microcracks, resulting from the beta- to alpha-cristobalite transformation, are the main reason for the degradation of the flexural strength.

Figures 7.8 and 7.9 show the microstructure of a sample sintered at 1400°C for 8 hours to examine the effect of transformed cristobalite on the crack. Thermals facet, crystal not amorphous, detected near the microcracks represent the cristobalite. The presence of thermal facets near the microcracks indicates that the microcracks were generated from the abrupt contraction induced when beta cristobalite transforms to alpha-cristobalite at ≈200°C on cooling, which affects the flexural strength with the contents of transformed cristobalite in the test bars shown in Figure 7.6. Therefore, to prevent the degradation of flexural strength from microcracks, cristobalite in the sintered ceramic molds used in the casting industry should be less than 10%.

7.5 KINETICS: CRISTOBALITE TRANSFORMATION IN FUSED SILICA COMPACTS

Figure 7.10 shows the QXRD data for weight fraction of cristobalite transformed in isothermally sintered fused silica powder for various annealing times and temperature. The weight percent increases sigmoidally with annealing time t, indicating that the formation of cristobalite can be fitted to a nucleation and growth kinetic model. The incubation time, τ_0, was represented arbitrarily by extrapolating the curve of the experimental results to the 2 wt% transformation level. An incubation time decreases with increasing sintering temperature, from 20 min at 1370 ^{o}C to 194 min at 1295 ^{o}C.

An incubation energy, Q, for the formation of a stable nucleus is a function of temperature in the Arrhenius equation;

$$k = A \exp\left(-\frac{Q}{RT}\right) \qquad 7.7$$

where k is the rate constant and Q is an incubation energy. In the nucleation step, k represents the number of stable nuclei (n*) and A is related to the total number of nuclei of the solid phase. For the exponential term of this expression, changes in temperature have a greater effect on the magnitude of the Q term in the numerator than the T term in the denominator. This Q corresponds to the free energy required for the formation of a stable nucleus at the critical radius. Figure 7.11 shows the incubation energy resulting

from the Arrhenius plot of incubation time against transformation temperature. The incubation time, τ_0, was obtained arbitrarily by extrapolating the curve of the experimental results to the 2 wt% transformation level.[16] The incubation phenomenon includes both diffusion and reaction. The data suggest that the cristobalite incubation involves an activated process with an apparent activation energy Q of 161 ± 13 Kcal/(g·mol) (674 ± 53 kJ/(g·mol)), determining the temperature dependence of the diffusion and reaction processes which form cristobalite nuclei. The activation energy represented in this research is in the range of those reported (122 to 170 kcal) by Heterington et al. for apparent intrinsic crystallization of various vitreous silicas.[17]

If we assume that the nucleation and growth processes occur after the incubation process, the transformation data can be described by a quantitative Avrami kinetic equation of the form [18,19]

$$wt\ \% = 1 - \exp[\ -K(D)\, f(\dot{N}, \dot{G})\, t_m^n\ ] \qquad 7.8$$

where $t_m = t - \tau_0$, where τ_0 is the temperature-dependent incubation time and n is the time exponent (or Avrami exponent). The term *K(D)* is a constant that correlates the volume fraction to weight fraction. If the density of the parent phase is equal to the product phase, then K (D) = 1. The function $f(\dot{N}, \dot{G})$ depends upon nucleation rate and growth rate. Time exponent (n) is independent of temperature when the nucleation and growth mechanism is not changed during crystallization. The time exponent (n) listed in

Table 7.2 is dependent on the mechanism of transformation reaction, which vary from 0.5 to 1.5 for diffusion-controlled, and from 1 to 3 for interface controlled kinetics. [20]

A regression method was used to extract the time exponent and the function K (D) $f(\dot{N}, \dot{G})$ for each temperature. The curve, which corresponds to the rising parts of the transformed cristobalite shown in Figure 7.10, can be described by straight lines by rearranging Equation 7.8:

$$\ln \ln\left(\frac{1}{1 - wt\,\%}\right) = \ln[-K(D) f(\dot{N}, \dot{G})] + n \ln t_m^n \qquad 7.9$$

Given the equation 7.9, the function K (D) $f(\dot{N}, \dot{G})$ and time exponent (n) of the cristobalite transformation can be calculated from the intercept and the slope of plot. Figure 7.12 shows that function K (D) $f(\dot{N}, \dot{G})$ and time exponent (n) are 4.55×10^{-2} and 1.53 ± 0.09, respectively. The results listed in Table 7.3 show the function K (D) $f(\dot{N}, \dot{G})$ and time exponent on the four different annealing temperatures, which have values of the time exponents between 1.5 and 2.0. The average time exponent of the transformed cristobalite is 1.85. In the case of crystallization of fused silica, there is no change of composition when fused silica transformed to cristobalite. Given the relation between the mechanism and avrami time exponent shown in Table 7.2, transformation kinetics are controlled by 2-dimensional interfacial growth. This transformation kinetics are close to the crystallization of cristobalite reported by Jean et al. that occurs either by 3-

dimensional diffusional (n=1.5) or 2-dimension interfacial (n=2) growth mechanism.[20]

7.6 CONCLUSION

The flexural strength of test bars increased with increasing sintering temperature, while the flexural strength decreased to 4.6 MPa with the higher sintering temperature of 1500^{o}C due to an increase in the amount of cristobalite. The flexural strength increased with increasing contents of transformed cristobalite up to 27.6%, yet it declined with cristobalite formation of more than 30%. Thermals facets, crystal not amorphous, detected near the microcracks represent the cristobalite. The presence of thermal facets near the microcracks indicates that the microcracks were generated from the abrupt contraction induced when beta cristobalite transforms to alpha-cristobalite at ≈200^{o}C upon cooling, which affects the flexural strength with the contents of transformed cristobalite in the test bars.

Transformation kinetics of fused silica powder have been studied by the QXRD data for weight fraction of cristobalite transformed in isothermally sintered fused silica powder for various annealing times and temperature. In the transformation-time-temperature (TTT) plot, the weight percent increases sigmoidally with annealing time t, indicating that the formation of cristobalite can be fitted to a nucleation and growth kinetic model. The transformation is preceded by a temperature dependent incubation time. The incubation is an activated process with an apparent activation energy of 161 ± 13 Kcal/(g·mol) (≈674 ± 53 kJ/(g·mol)). Transformation kinetics by QXRD can be fitted to an Avrami equation with an average time exponent of 1.85. Since fused silica

transformed to cristobalite, there is no change of composition such that the transformation kinetic is controlled by short range diffusion across the interface rather than long range diffusion control.

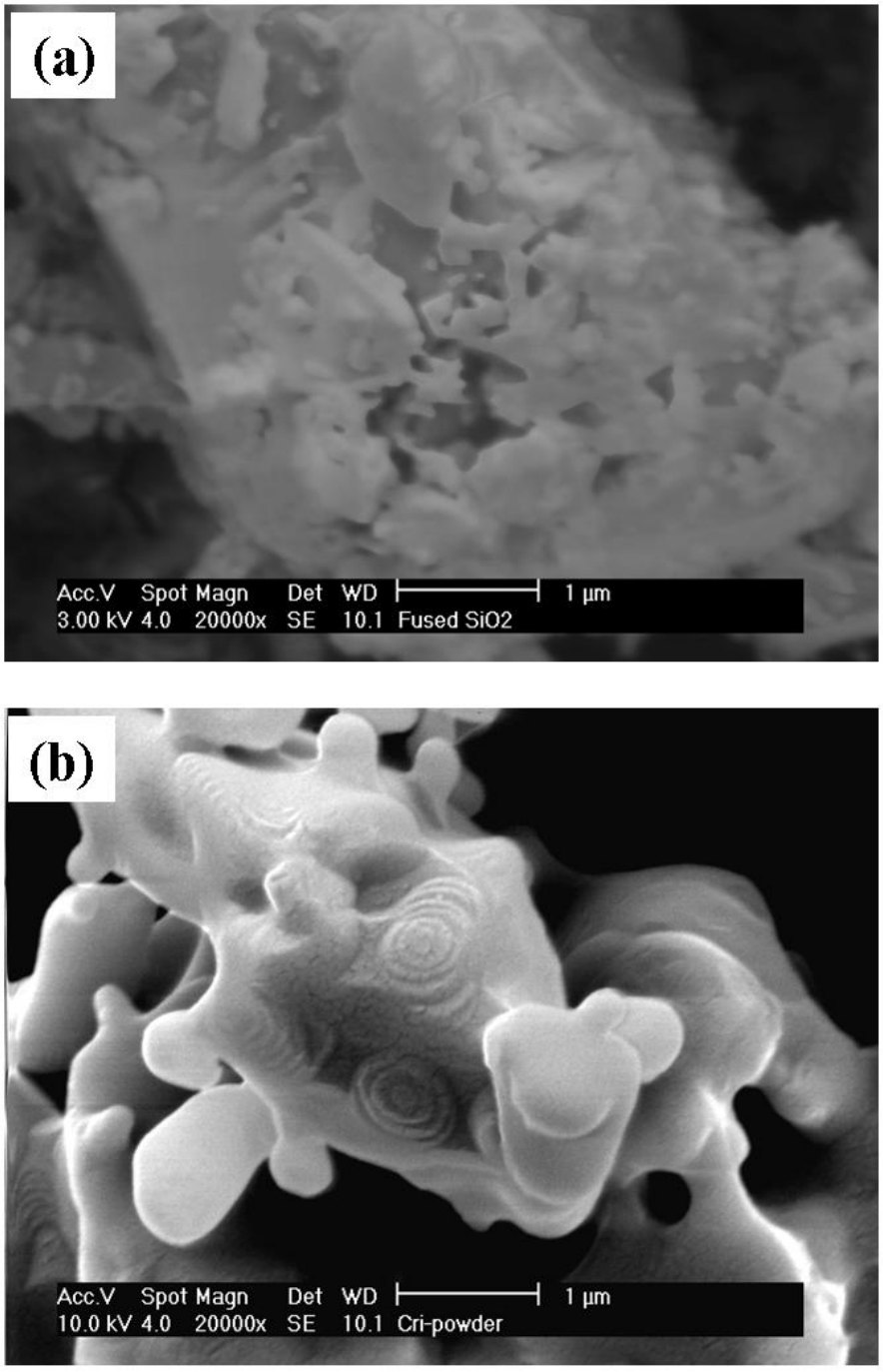

Figure 7. 1 SEM images of (a) as received fused silica powder and (b) cristobalite.

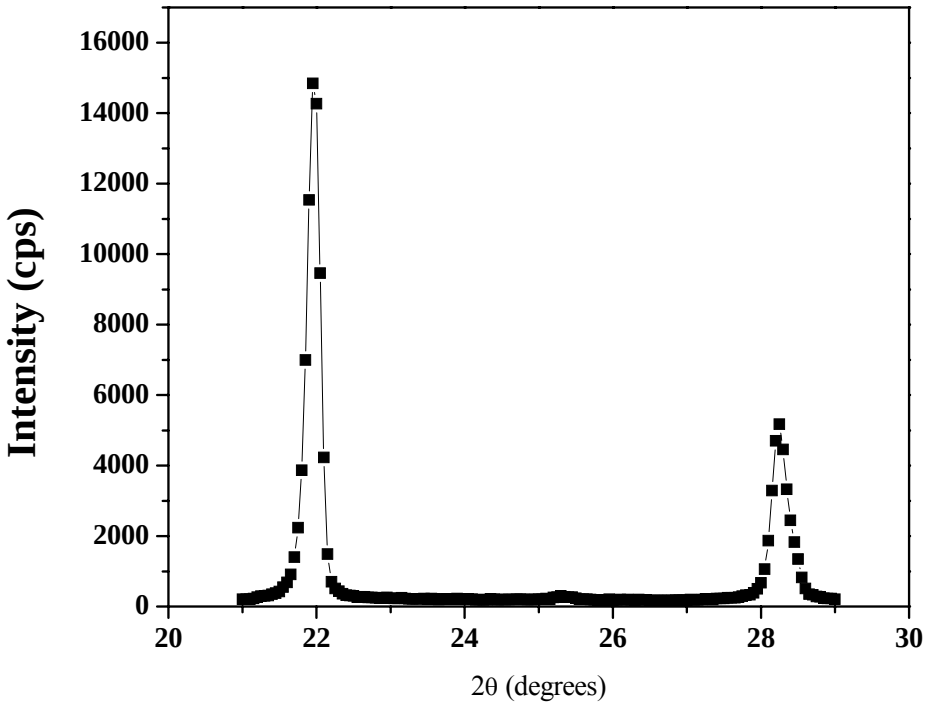

Figure 7. 2 X-ray diffraction of 80 % α-cristobalite (2θ = 21.95^{o}) and fluorite (2θ = 28.26^{o}), used to prepare a calibration curve in order to measure the amount of α-cristobalite in the sintered ceramic mold.

Table 7. 1 Thermal condition for binder burn-out and sintering

	Temperature (^{o}C)	Rate (^{o}C/min.)	Holding time (hour)
Binder burn-out	**25 (room temp.) - 100**	**5**	**1**
	100 - 200	**5**	**2**
	200 – 335	**3**	**2**
	335 – 415	**1**	**2**
	415 – 480	**3**	**2**
	480 – 600	**2**	**2**

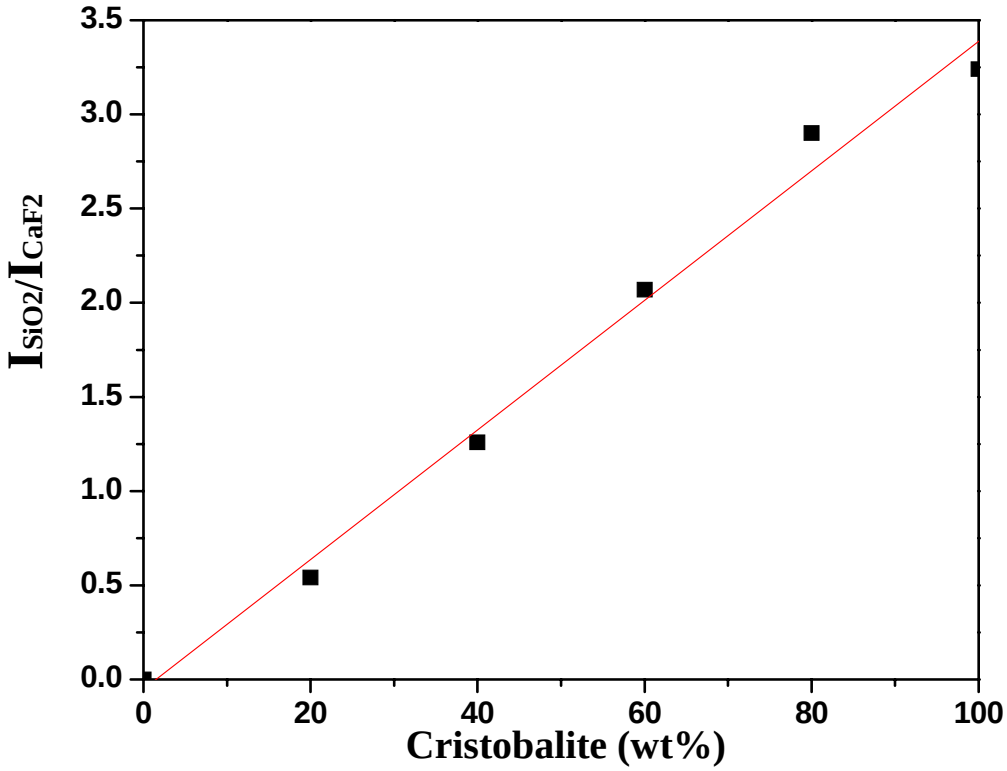

Figure 7. 3 Calibration curve for cristobalite analysis, with fluorite as internal standard. I_{SiO2} is the intensity of the d = 4.05Å line of cristobalite, and I_{CaF2} is the intensity of the d = 3.16Å line of fluorite.

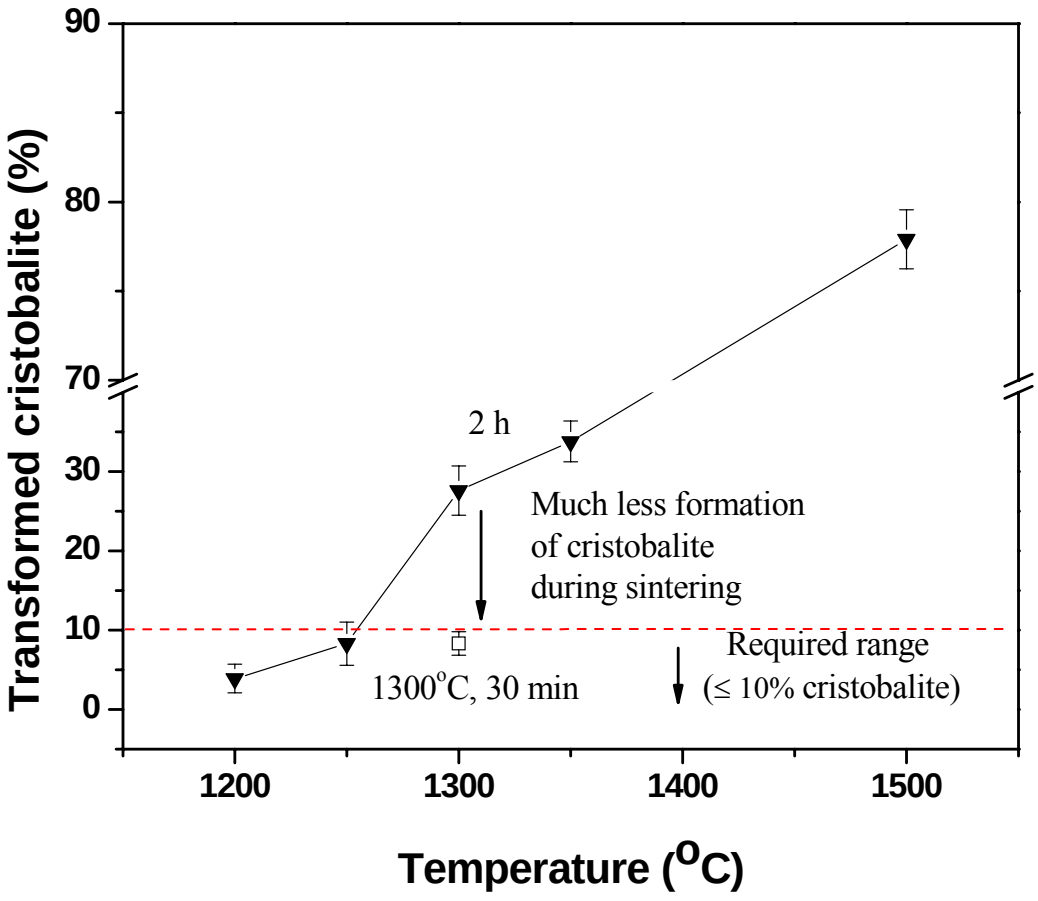

Figure 7. 4 Amount of transformed cristobalite as a function of annealing temperatures.

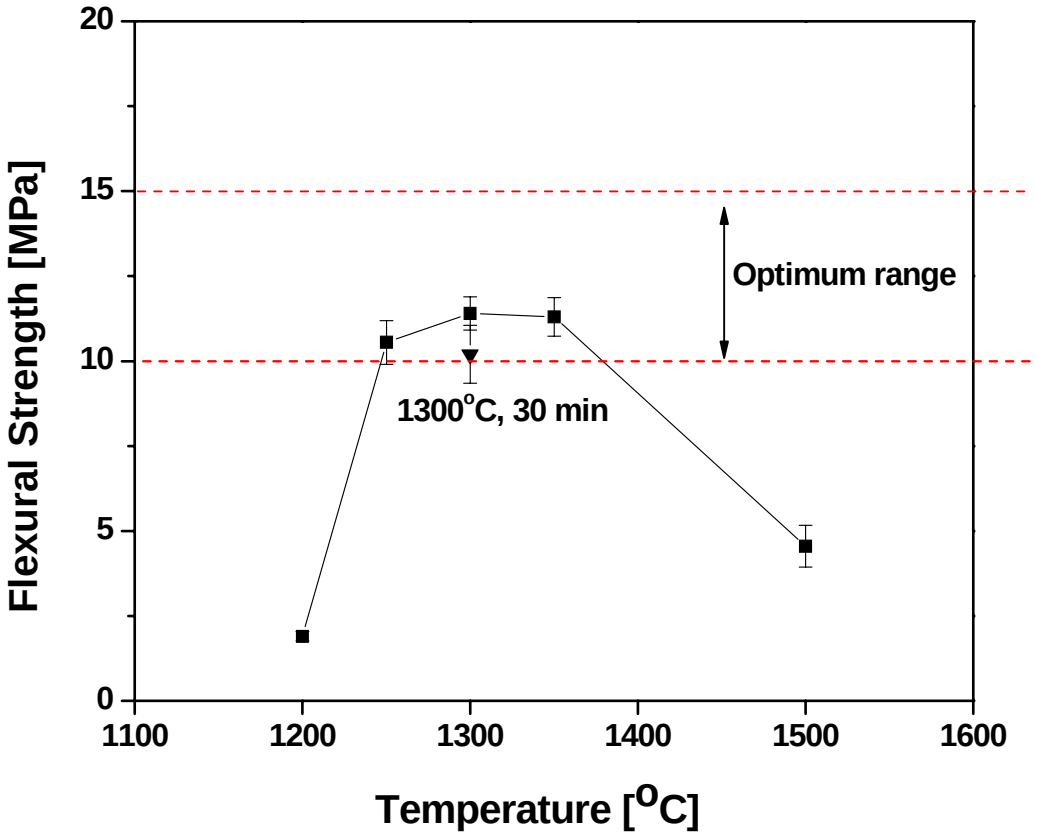

Figure 7. 5 The flexural strength of test bar sintered as a function of different sintering temperatures.

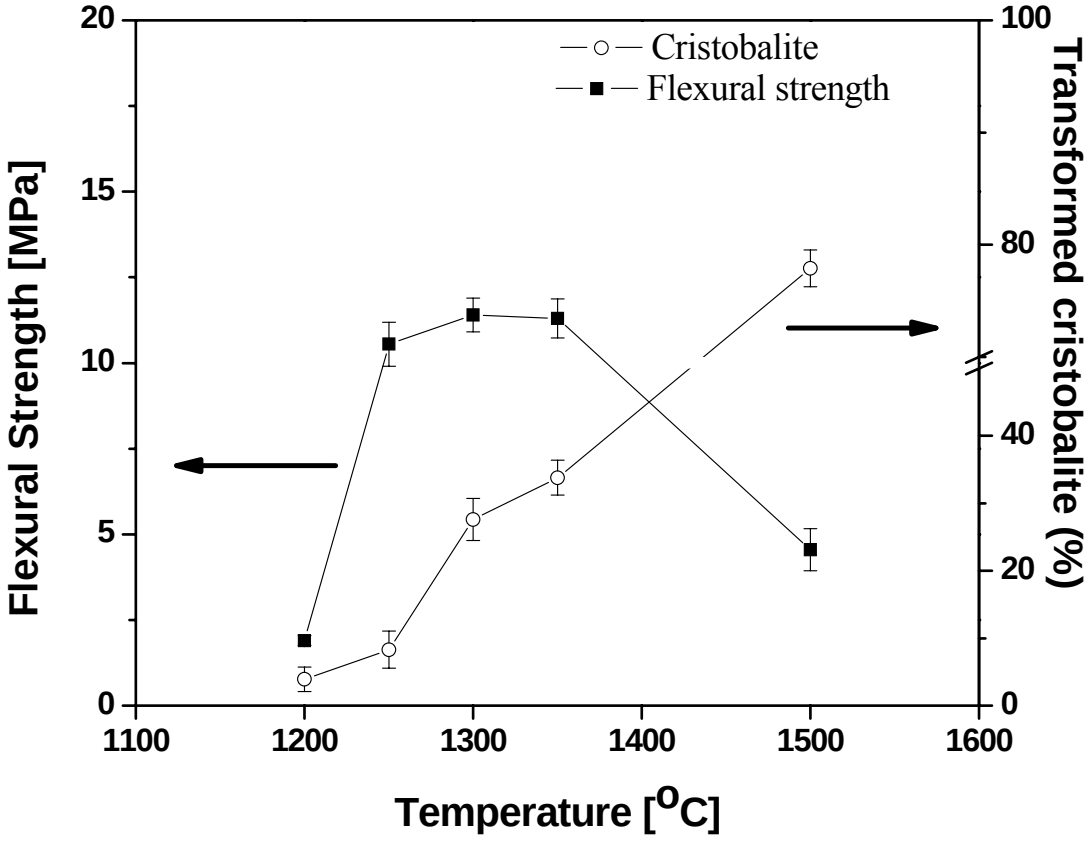

Figure 7. 6 Dependence of the flexural strength on the contents of transformed cristobalite in the test bars.

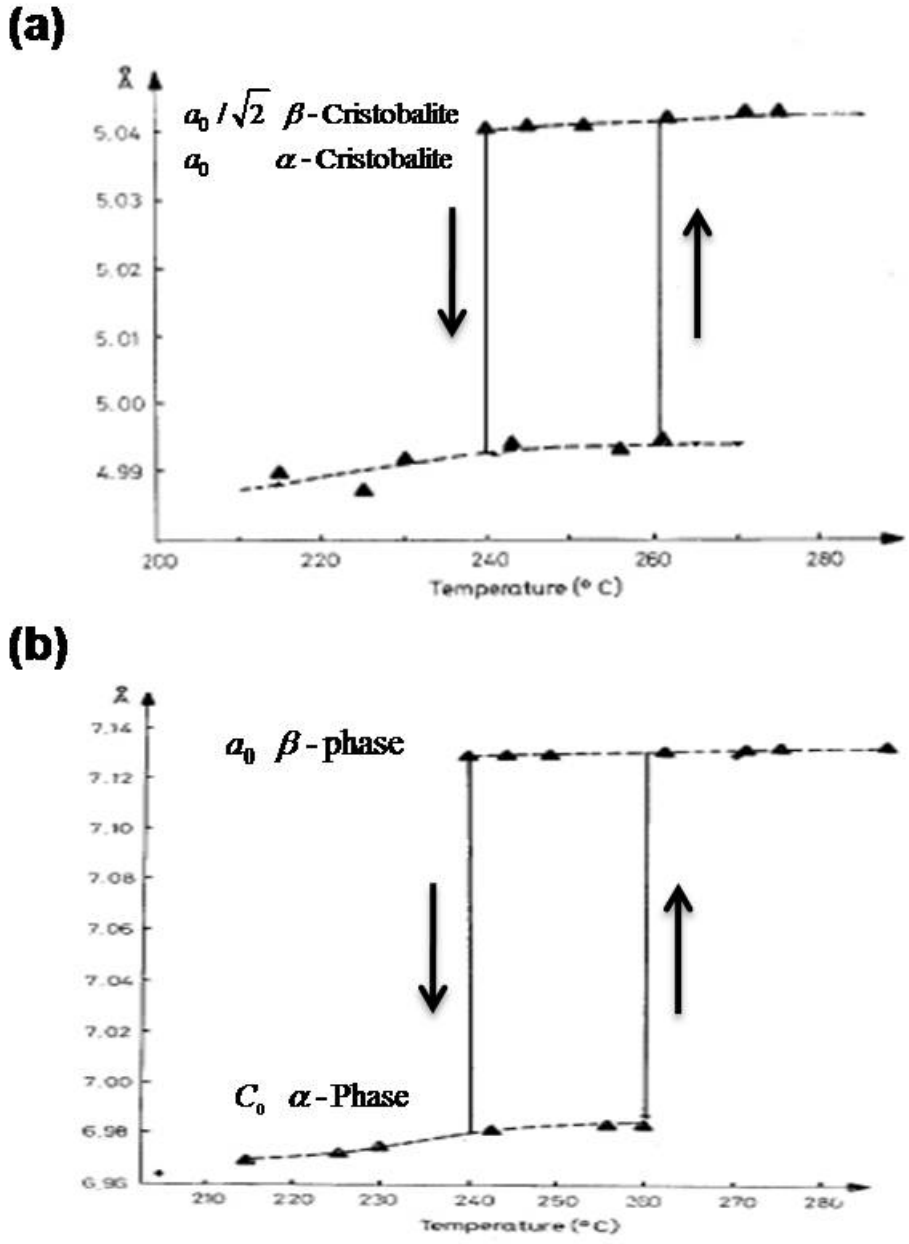

Figure 7. 7 A discontinuous change in the lattice dimensions of transformed cristobalite; (a) Lattice parameter a_0 of cristobalite (b) Lattice parameter c_0 of cristobalite.[15]

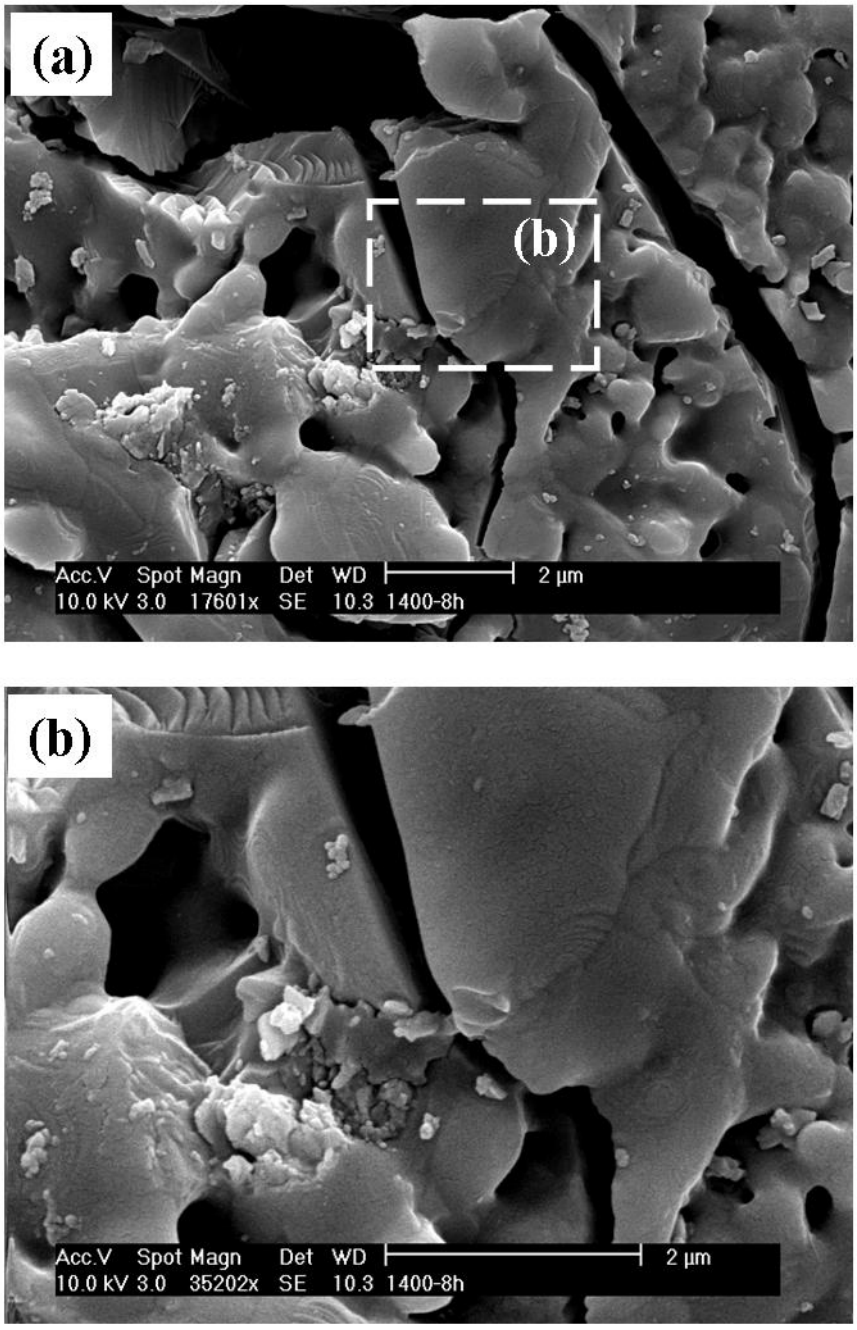

Figure 7. 8 SEM micrographs for a sample sintered at 1400 ^{o}C for 8 h; Thermals facets representing cristobalite are detected near the microcracks.

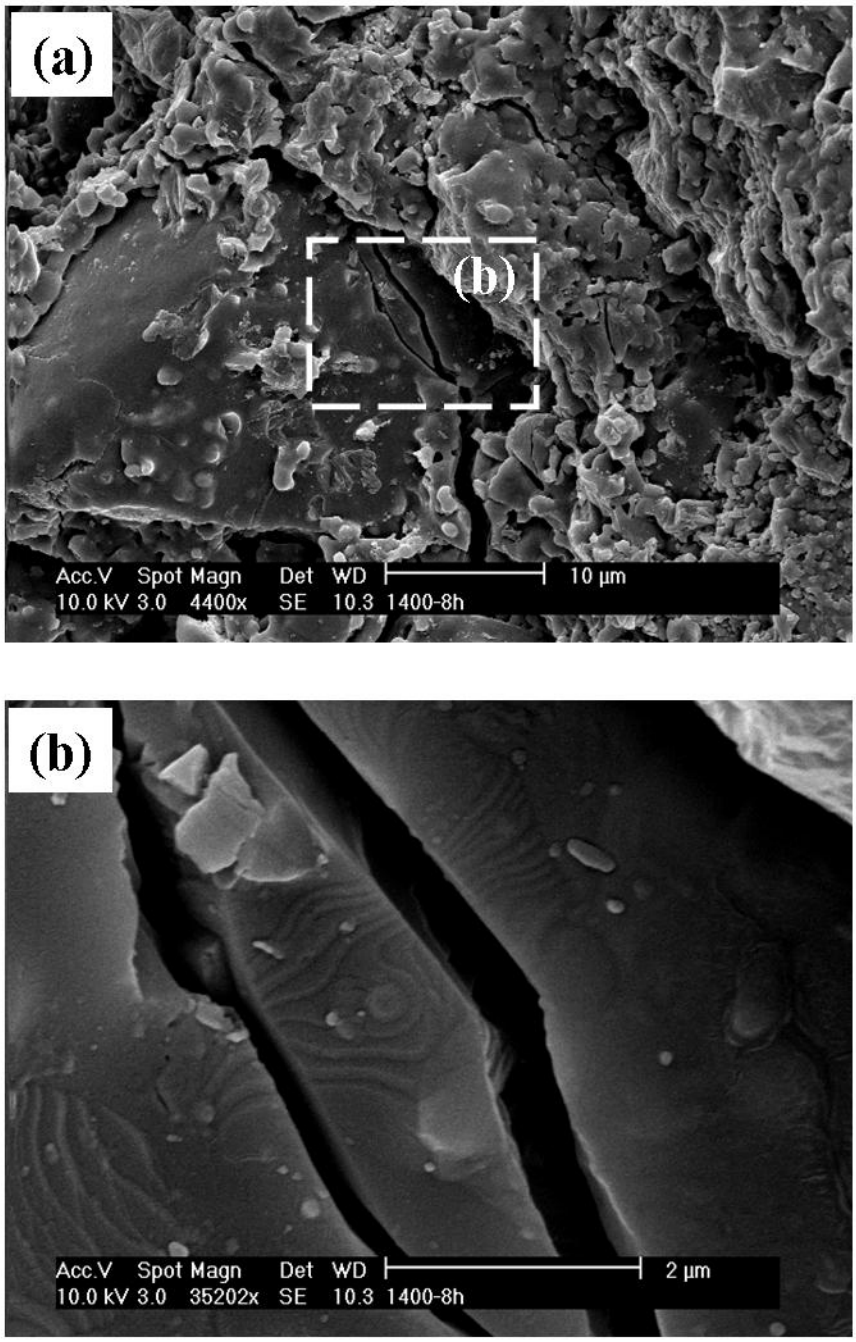

Figure 7. 9 SEM micrographs at different position of a sample sintered at 1400 ^{o}C for 8 h; Thermals facets representing cristobalite are detected near the microcracks.

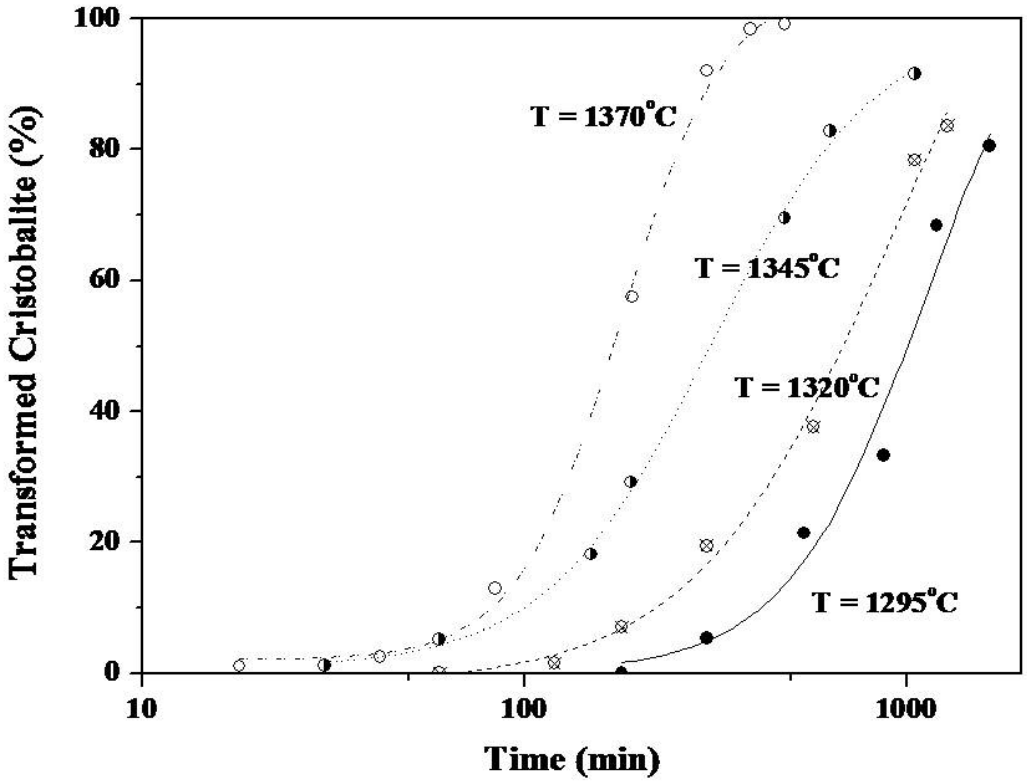

Figure 7. 10 Weight percent of transformed cristobalite versus annealing time plotted according to nucleation and growth kinetics.

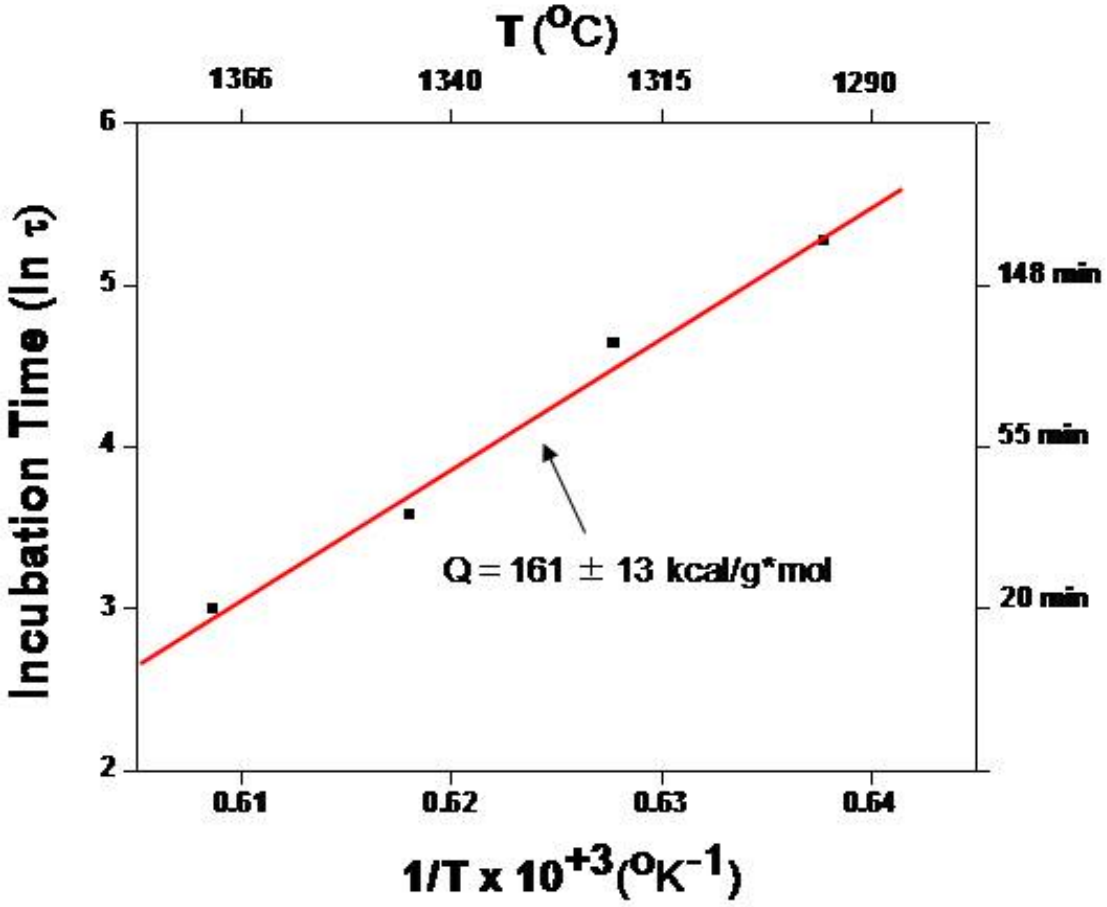

Figure 7. 11 Arrhenius plot of incubation time versus the annealing temperature gives the incubation energy Q of 161 ± 13 kcal/(g·mol).

Table 7. 2 Avrami time exponent (n) representing the mechanism of transformation.

	Diffusion-controlled	Interface-controlled
3-dimension	1.5	3.0
2-dimension	1.0	2.0
1-dimension	0.5	1.0

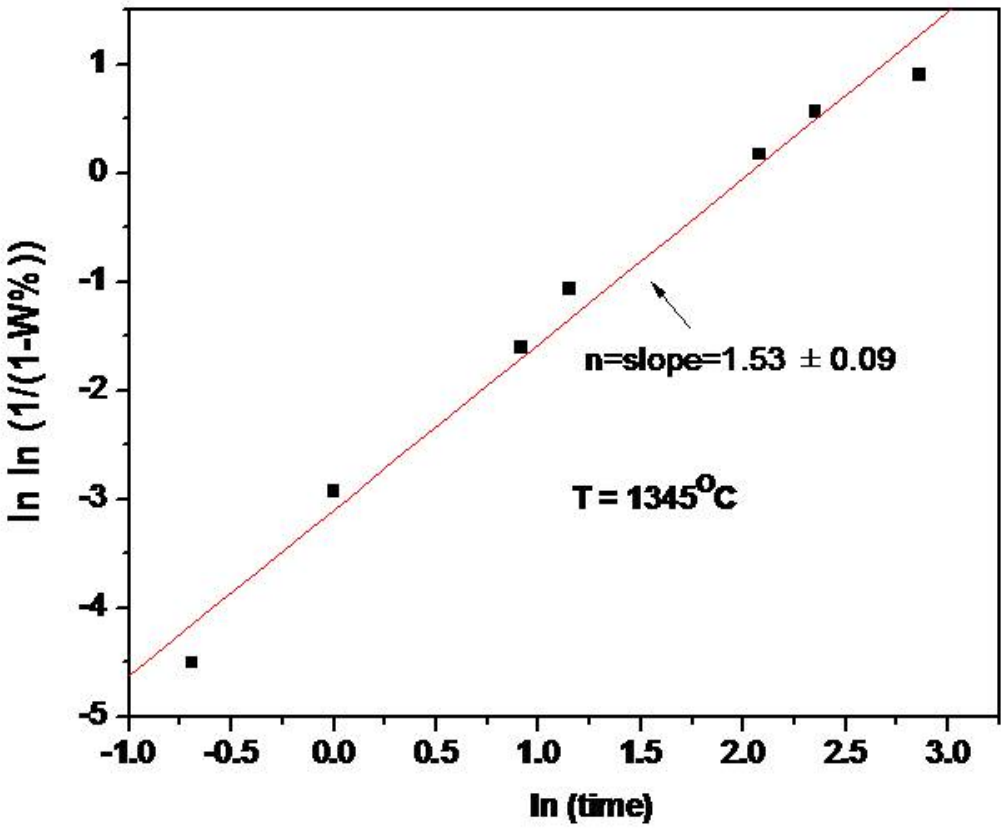

Figure 7. 12 Time exponent (n) of the cristobalite transformation plotted under normalized time and transformation weight scale. The slope, n, is 1.53 ± 0.09 at 1345 ^{o}C.

Table 7. 3 Time exponents (n) and K (D) f (Ṅ, Ġ) of the cristobalite transformation of fused silica compacts

Annealing temp (°C)	n	$K(D)f(\dot{N},\dot{G})$
1295	1.99 ± 0.16	2.5×10^{-3}
1320	1.90 ± 0.17	6.73×10^{-3}
1345	1.53 ± 0.09	4.55×10^{-2}
1370	2.01 ± 0.10	8.21×10^{-2}

Reference

1. I.C. Huseby, M.P. Borom, and C.D. Greskovich, "High temperature characterization of silica-base cores for superalloys", *Am. Ceram. Bull*., **58** [4], 448-52, 1979.
2. A.A. Wereszczak, K. Breder, M.K. ferber, T.P. Kirkland, E.A. Payzant, C.J. Rawn, E. Krug, C.L. Larocco, R.A. Pietras, and M. Karakus, "Dimensional changes and creep of silica core ceramic used in investment casting of superalloys", J. Mater. Sci., 37, 4235-45, 2002.
3. P. R. Beeley, R.F. Smart, *Investment Casting*, The university press, Cambridge, UK, 1995, 65.
4. C.H Chao and H.Y. Lu, "Optimal composition of zircon-fused silica ceramic cores for casting superallys", *J. Am. Ceram. Soc*., **85** [4], 773-79, 2002.
5. W.D. Kingery, H.K. Bowen, and D.R Uhlmann, "Introduction to ceramics", John wiley & sons, New York, 469-513, 1976.
6. J.S. Reed, "Principles of ceramics processing", John wiley & sons, New York, 594-608, 1995.
7. W.D. Kingery and M. Berg, "Study of the initial stages of sintering solids by viscous flow, evaporation-condensation, and self-diffusion", *J. Appl. Phys.,* **26** [10], 1205-12, 1955.
8. T.J. Clark and J.S. Reed, "Kinetic processes involved in the sintering and crystallization of glass powders", *J. Am. Ceram. Soc*., **69** [11], 837-46, 1986.
9. J.K. Mackenzie and R. Shuttleworth, "A phenomenological theory of sintering",

Proc. Phys. Soc., London, Sect. B, **62**, 833-52, 1949.

10. R.H. Doremus, "Glass science", John wiley & Sons Inc., New York, 73-88, 1994.
11. M.J. Davis and P.D. Ihinger, "Heterogeneous crystal nucleation on bubbles in silicate melt", *American Mineralogist*, **83**, 1008-15, 1998.
12. E.D. Zanotto and P.F. James, "Experimental tests of the classical nucleation theory for glasses", *J. Non-Cryst. Solids*, **74**, 374-94, 1985.
13. D. Turnbull, "On the relation between crystallization rate and liquid structure", *J. Phys. Chem.*, **66** [4], 609-13, 1962.
14. B.D. Cullity, "Elements of x-ray diffraction", Addison-Wesley publishing company Inc., 407-20, 1978.
15. A.J. Leadbetter and A.F. Wright, "The α-β transition in the cristobalite phases of SiO_2 and $AlPO_4$: I. X-ray studies", *Philosophical magazine*, **33** [1], 105-12, 1976.
16. W.C. Wei and J.W. Halloran, "Transformation kinetics of diphasic aluminosilicate gels", *J. Am. Ceram. Soc*., ***71*** [7], 581-87, 1988.
17. F.E. Wagstaff and K.J. Richards, "Kinetics of crystallization of stoichiometric SiO_2 glass in H_2O atmospheres", *J. Am. Ceram. Soc*., ***49*** [3], 118-21, 1966.
18. M. Avrami, "Kinetics of phase change. I: General theory", J. Chem. Phys., 7, 1103-12, 1939.
19. M. Avrami, "Kinetics of phase change. II: Transformation-time relations for random distribution of nuclei", J. Chem. Phys., 8, 212-241940.
20. J.H. Jean and T.K. Gupta, "Crystallization kinetics of binary borosilicate glass composite", *J. Mater. Res.*, **7** [11], 1992.

CHAPTER 8

CONCLUSIONS

8.1 OVERVIEW

Investment casting (IC) is a widely used technique for modern metal casting providing an economical means of mass producing shaped metal parts containing complex features. However, investment casting needs refractory ceramic cores and shell molds. The shell molds are built by multiple dip coating on injection-molded wax patterns, which themselves are formed over injection-molded ceramic cores. The tooling required for these two injection molding operations lead to excessive costs and very slow prototype cycles. These limitations often present problems in justifying costs of producing parts requiring a small number of castings.

As an alternative for small production runs or designs too complex for conventional cores and patterns, we used ceramic stereolithography (CerSLA). CerSLA is an extension of the standard RP process of stereolithography, using a photopolymerizable suspension of ceramic powders. Using the layer-by-layer growth enabled by CerSLA, we eliminate the pattern production delay and cost issue, which produce a one-piece mold integrated with the core, or an Integrally Cored Ceramic Investment Casting Mold (ICCICM). We can deeply understand on the nature and properties of the photopolymerizable suspension for refractory silica powders, the build

parameters (layer thickness, laser write style, etc), and the processing steps after CerSLA fabrication (draining, binder removal, sintering). Given the suspension including 60 volume percentage of fused silica, two processing parameters: D_p of 805 ± 48 microns and E_c of 15 ± 1.29 mJ/cm^2 are obtained from the slope and the x-intercept value in the cure depth as a function of energy dose. The accuracy of CerSLA is evaluated by the size difference resulting from the comparison between a green and a sintered body with the STL file, for both core and shell parts of the cross section of layer 630. At the positions of cross section measured in the X-Y plane, the linear tolerance of the green body are fairly controlled under ± 0.2 mm.

In the suspension of CerSLA, the use of non-reactive and unsinterable coarse ceramic powder is required to maintain its physical dimensions in the mold when the hot metal hits it. However, the differential sedimentation of coarse or denser particles induces segregation in a layer, where the population of larger or denser particles accumulate near the bottom. Severe segregation associated with mono-modal PSD is suppressed by using bimodal PSD. In the case of a coarse powder inducing bad segregation, the settling velocity of 0.84 microns/sec was calculated from a coarse powder with diameter of 27 microns. On the other hand, in the other case of a bimodal powder showing much less segregation, the settling velocity for a bimodal powder with diameter of 12 microns was 0.06 microns/sec. Using bimodal powder increases the solid concentration and decrease the particle size, thus modifying the sedimentation velocity of fused silica powder and preventing segregation in a layer due to slow settling velocity. No segregation or much less segregation exists in layers when bimodal powders are used to suppress segregation.

In order to prevent segregation in a layer, a criterion should be satisfied such that the time required for the suspended particle to settle a layer thickness is longer than the time required to write a layer. Given the criterion, the degree of segregation (β) was derived based on the two competing factors; settling time of powder and writing time of a layer.

$$\beta = \frac{\tau_{write}}{\tau_{settle}} = \frac{A}{\lambda}\frac{1}{P_L} v_{stokes}(1-\phi)^n E_c \exp(\frac{\lambda\phi}{\gamma d})$$

where A surface area (cm^2), λ layer thickness (μm), P_L power of laser (mW), v_{stokes} the stoke's settling rate, ϕ the concentration of solid, γ the term for the resin sensitivity related to the refractive index difference between ceramic powder and resin, and *d* is light scattering diameter. β is dependent on the Design factor (surface area (A_s) and layer thickness (λ)) and Apparatus factor (laser power P_L). In the case of design factor, layer thickness of 200 microns and silica powder with particle size of 60 microns, ceramic stereolithography can build layers with the surface area less than 18.4 cm^2 without segregation. In the case of apparatus factor, a layer thickness of 100 micron and a suspension including fused silica powder with uniform particle size of 40 microns, laser power larger than 26.5 mW is required to prevent segregation.

In order to apply ICCICM to investment casting, the sintering of a fused silica compact and the transformation to cristobalite should be considered. During the sintering of fused silica molds, cristobalite transformed from the fused silica provides stiffness for

the fused silica molds. The silica molds, being composed of a glassy material, starts to soften and will be susceptible to bow or twist if the differential expansion forces are imposed on the system. This problem is alleviated by using a modified composition such as 90% silica glass and 10% crystalline cristobalite. However, if an excessive amount of cristobalite exists in fused silica molds, abrupt contraction induced from beta- to alpha-cristobalite at ≈200^{o}C on cooling leads to extensive cracking, thus decreasing the strength. Therefore, it is necessary to investigate the reaction kinetics and phase transformation mechanism of cristobalite.

Transformation kinetics of fused silica powder has been studied by the QXRD data for weight fraction of cristobalite transformed in isothermally sintered fused silica powder for various annealing times and temperature. In the transformation-time-temperature (TTT) plot, the weight percent increases sigmoidally with annealing time t, indicating that the formation of cristobalite can be fitted to a nucleation and growth kinetic model. The transformation is preceded by a temperature dependent incubation time. The incubation is an activated process with an apparent activation energy of 161 ± 13 Kcal/(g·mol) (≈674 ± 53 kJ/(g·mol)). Transformation kinetics by QXRD can be fitted to an Avrami equation with an average time exponent of 1.85. Since fused silica transformed to cristobalite, there is no change of composition such that the transformation kinetics are controlled by short range diffusion across the interface rather than long range diffusion control.

8.2 FUTURE DIRECTIONS

1. Oxygen inhibition. The formulation of suspension based on the acrylate monomer as photo-curable polymer due to the high reactivity and fast cure time has been used. However, acrylate monomers easily absorb oxygen so that molecular oxygen quenches the active initiators, decreasing the rate of initiation and monomer conversion. As shown in Chapter 6, since residual monomer initiates cracks during binder burn-out (BBO), the monomer conversion should be increased. New and more efficient monomer system (Acrylate/Epoxide) could be used to prepare the suspension formulation with less absorbed oxygen. Using the system can give following advantages; low viscosity, low shrinkage, and no inhabitation of oxygen.

2. Improved rheology. It is necessary to have a stereolithography ceramic suspension fluid enough for the recoat step in the build process. Therefore it is important to know the viscosity and to achieve the most fluid suspension possible. Suspensions require a fairly high solid fraction of ceramic powder to be dispersed (usually > 50 vol %) in a monomer of liquid state. However, the addition of more powder results in a more viscous suspension. New electrosteric dispersants consisting of polymeric chains with a polar end group will be used. As the polar group readily adsorbs onto hygroscopic ceramic surfaces with the polymer chain extending into the hydrophobic medium to provide steric repulsion, high solid loaded suspension will be prepared.

3. Ceramic stereolithography (CerSLA) as a novel process is investigated to

replace the lost wax process which is a technique widely used to fabricate refractory molds for investment casting. When CerSLA build ceramic casting shell mold with an integral core designed by Honeywell, the most important aspect is how to precisely evaluate the consistency and accuracy of ceramic mold. Micro-computer tomography (Micro CT) would be used to compare a STL file to a green body of ICCICM, which obtains 360^{o} radioscopic image data while irradiating object with X-rays. Given the data, cross-sectional images of a green body are generated so that more consistent and accurate comparison can be possible.

4. After preparing integral cored shell molds directly fabricated using CerSLA, molds will be delivered to Precision Castparts Corporation (PCC) for making a casting metal component for a turbine airfoil. This CerSLA will in fact provide a significant benefit very quickly, as the core tooling is often the bottleneck in investment casting research. The molds with the different mold thicknesses: 1.8, 3.3, 6.4 millimeters will be fabricated to investigate the effect of mold thickness on the investment casting. With directly fabricated integral cored shell mold, experts at PCC will pour the molten metal into ceramic mold to cast turbine airfoil. Additionally, we will compare cast result of separately fabricated core and shell mold by conventional investment casting with that of directly fabricated integral cored shell mold.

This thesis investigates is the development of a novel process to replace the lost wax process, producing an integrally cored ceramic investment casting mold (ICCICM). Through the results of the thesis, the process for fabricating the ceramic core with a

ceramic mold shell in a single patternless construction for turbine airfoils with complex internal passageways is outlined. Given the sintered ICCICM, we hope that CerSLA replaces lost wax process and brings new opportunities and research direction for the investment casting.